Test of the Standard Model of Electroweak Interactions by Measuring the Anomalous $ZZ\gamma$ and $Z\gamma\gamma$ Couplings

A Dissertation Presented

by

Gregory Leonid Landsberg

to

The Graduate School

in Partial Fulfillment of the Requirements

for the Degree of

Doctor of Philosophy

in

Physics

State University of New York
at
Stony Brook

December 1994

State University of New York
at Stony Brook

The Graduate School

Gregory Leonid Landsberg

We, the dissertation committee for the above candidate for the Doctor of Philosophy degree, hereby recommend acceptance of the dissertation.

dissertation director
Professor Paul Grannis
Department of Physics

chairman of defense
Professor Michael Marx
Department of Physics

committee member
Professor Peter Koch
Department of Physics

outside member
Professor Ulrich Baur
Department of Physics
SUNY at Buffalo

This dissertation is accepted by the Graduate School.

Graduate School

Abstract of the Dissertation

Test of the Standard Model of Electroweak Interactions by Measuring the Anomalous $ZZ\gamma$ and $Z\gamma\gamma$ Couplings

by

Gregory Leonid Landsberg

Doctor of Philosophy

in

Physics

State University of New York at Stony Brook

1994

A novel test of the gauge sector of the Standard Model (SM) of electroweak interactions — the first measurement of the tri-linear $ZZ\gamma$ and $Z\gamma\gamma$ couplings — was carried out with the DØ detector at the Fermilab Tevatron in $p\bar{p}$ interactions at $\sqrt{s} = 1.8$ TeV. We observed 4 (2) $p\bar{p} \to Z\gamma + X$ events in the dielectron (dimuon) decay channel of the Z, with a total expected background of 0.5 ± 0.1 events, which is in good agreement with SM predictions. The following limits on the anomalous CP-conserving and CP-violating

h_{i0}^V couplings were obtained from fitting the p_T^γ spectrum for a form factor scale of $\Lambda = 500$ GeV (for the case when only one coupling is varied at a time): $|h_{10,30}^Z| < 2.0$, $|h_{20,40}^Z| < 0.5$, $|h_{10,30}^\gamma| < 2.1$, $|h_{20,40}^\gamma| < 0.5$. The results are compared with recent data from the CDF and L3 experiments, as well as with the indirect limits from low energy measurements.

To my Father

Contents

List of Figures

List of Tables

Acknowledgements

Take heart, I said to myself: don't think of Wisdom now; ask the help of Science.

Umberto Eco, "Foucault's Pendulum"

High Energy Physics is an amazing branch of science... Unpredictable, like the fabulous Chicago weather (and like that weather sometimes just pushing you into the lab by simply leaving you no other choice). Being developed around the world by brilliant and devoted people, despite numerous efforts of different governments to terminate their hopes and their future. It is probably the second branch of physics after the space science with a high political impact. Many hate it. Some love it. Which is just the other side of the same coin, since real love is not "for" — it is "despite of." And I must start my acknowledgements with a few nice words about the branch of Science I have chosen.

It is exciting and difficult to work in the field which changes so rapidly. Only 40 years ago the antiproton was discovered at Berkeley. Now, at the Tevatron, we have 50 billion of them in each bunch. About ten years ago the first few W and Z bosons were observed at CERN. It took both the physics and organizing genii of Carlo Rubbia, and many years of hard work of hundreds

of people to build the machine and the detectors capable of fulfilling that goal. Nowadays the W and Z are text-book particles, and I have to use a lint remover to pick up several of them which stuck to my clothes after each visit to the lab.

This Dissertation contains a description of a novel test of the Standard Model of electroweak interactions. In some sense, it is at the leading edge of High Energy Physics today. But it is clear, that in a decade or so the new experiments will improve the results obtained in this first measurement so much, that the two hundred pages of this Thesis will only be of historical interest, and its few remaining copies will comfortably age on dusty shelves of the libraries, with their rusty staples dimly glittering in the dull light turned on by an occasional visitor. And it will be only this preface which still might be up-to-date at that time. Since the things change, but Science itself does not. Because there are, and there always will be people who share their experience and knowledge with the new generations of future scientists, people whom we owe a great debt. And this is why I want this preface to be a bit longer and a bit more broad than a standard acknowledgement section.

First of all I am grateful to my parents who raised me in a scientific spirit. I am the third generation of physicists in my family, and this fact simply left me no other choice than to go into physics. And I do not regret that I did it. I very well remember a phone call which rang in our apartment exactly twenty years ago, one chilly November day of 1974. That morning the discovery of Ψ particle, now known as the J/Ψ, was announced to the world, and somebody called my father, who worked on free quark searches at that time, to tell him

that the fourth quark had just been discovered. There are not too many things which would make my dad to interrupt his morning shower. But this one was apparently among those few. And even though I was only 7 years old at that time, I sort of mentioned to myself, that it must be a really exciting job, which makes you to jump out of the shower and run to the phone! Not that this reminiscence of childhood governed my choice later on, but it must have contributed.

Back to Russia, during my college days and first years of experimental work in the fixed target GAMS experiment, I was lucky to meet many good physicists, and I would like to thank here my first advisor, Yuri Prokoshkin, who taught me a lot about the real work in a modern experiment — both the physics and human aspects.

I would like to thank Mike Marx who introduced me to DØ, a part of which I am proud to be, and who encouraged me to apply to the graduate school of SUNY at Stony Brook.

I owe a great debt to my advisor, Paul Grannis, who first of all acquainted me with the DØ experiment, and helped me a lot during my first days as a graduate student. He always had time for me despite the tremendous workload as the DØ spokesperson. Paul participated in many aspects of this analysis, and several ideas developed here were generated by him. And, most important, during my three years in DØ he always set an example with his broad and deep knowledge of physics and detectors; an example of a complete scientific honesty.

It is a pleasure to express my deep gratitude to Ulrich Baur, who in all

senses initiated the analysis described in this Dissertation with a thorough article (written together with E.L. Berger) where many theoretical questions were answered for the first time. He kindly sent me the preprint as soon as it appeared, and this blue book was literally on my table all the time since I started to work on this topic. Ulrich was patient enough to answer in detail tons of my electronic letters with numerous questions about the anomalous couplings which I raised during different stages of the analysis. He also provided us with a fast Monte Carlo program for theoretical calculations, and most of all was a valued friend and advisor for these last two years.

And of course, I am grateful to all members of the DØ family, who built this superior detector, put it into operation, and made this analysis possible at all. I would like to name several people here, who deserve a special "thank you." I owe Sandor Feher, with whom I collaborated on the scintillating fiber detector for tracking chamber calibrations. He introduced me to many DØ folks and helped me in several other aspects. I want to thank my fellow Stony Brook students for being my neighbors in the tight but never dull "cubicles" of the DØ Trailer City. Many people contributed a lot to the analysis described in this Dissertation and kindly did parts of the work for me: Hiro Aihara, Brajesh Choudhary, Mike Kelly, Stefano Lami, and Tony Spadafora. Many more people provided stimulating discussions: Jim Cochran, Marcel Demarteau, Guido Finocciaro, Steve Glenn, Qizhong Li-Demarteau, Meenakshi Narain, Ed Oltman, and Michael Rijssenbeek. I am grateful to Paul Russo and Kim Kwee Ng, computer system managers at Fermilab and Stony Brook, who put a lot of effort into keeping computers working and who helped me to

solve numerous software problems. Many thanks also to Jim Cochran, Alain Pluquet, and Scott Snyder who provided me with several detector plots.

I want to thank all the people who read and reread the drafts of this Dissertation and improved it in many aspects by their comments: Ulrich Baur, Jim Cochran, Paul Grannis, Srini Rajagopalan, and Tony Spadafora. Many thanks to Steve Errede of CDF and Fawzi Boudjema from LAPP for a lot of fruitful discussions. I would also like to thank Steve for providing us with the CDF and L3 data.

And last, but not least, I am grateful to many of my friends — beautiful ladies and real gentlemen — who have nothing to do with High Energy Physics, and who simply made my life much more interesting and diverse. I owe to them my numerous trips and a lot of fun in North Carolina and Florida, Atlanta and New York, Boston and Norfolk, Urbana and Binghamton, and of course The Windy City of Chicago. Quoting *"Conquest of Happiness"* by Bertrand Russell,

> *One of the symptoms of approaching nervous breakdown is the belief that one's work is terribly important, and that to take a holiday would bring all kinds of disaster. If I were a medical man, I should prescribe a holiday to any patient who considered his work important...*

And I wish to thank my friends for keep reminding me that there are many important things in life other than my work.

Chapter 1

Introduction

Only for you, children of doctrine and learning, have we written this work. Examine this book, ponder the meaning we have dispersed in various places and gathered again; what we have concealed in one place we have disclosed in another, that it may be understood by your wisdom.

Heinrich Cornelius Agrippa von Nettesheim,

"De occulta philosophia"

The Standard Model of Electroweak Interactions (SM) is one of the most aesthetic theories of modern physics. Developed in the 60's by S.L. Glashow, A. Salam, and S. Weinberg [1], it received its first experimental confirmation in 1973 with the observation of neutral currents in the Gargamelle bubble chamber at the CERN neutrino beam [2]. (Six years later, in 1979, Glashow, Salam and Weinberg won the Nobel Prize for this theory unifying the electromagnetic and the weak interactions.)

A more direct experimental confirmation of the SM was obtained a few years later, in 1983, with the discovery of the intermediate heavy vector bosons

(W and Z) by the UA1 and UA2 Collaborations [3, 4] at the CERN $p\bar{p}$-collider. The significance of this discovery was that the existence of these bosons is a unique and explicit prediction of this theory. Therefore, the search for these particles was a crucial test of the SM.

Numerous experimental tests which have been performed since the discovery of the W and Z bosons have not revealed any deviations from the SM. Currently, the SM based on the special theory of relativity, quantum mechanics, and quantum electrodynamics (QED) has become a cornerstone of our knowledge of Nature.

In the work discussed in the present Dissertation, a novel direct test of the SM has been carried out. We performed a search for anomalous couplings between the Z bosons and photons. This is the first direct experimental test of the SM predictions on the self-interactions between neutral gauge bosons. It has been carried out simultaneously and independently by the DØ and CDF Collaborations at Fermilab and the L3 Collaboration at CERN.

This Dissertation consists of six additional chapters. Chapter 2 (*Theory of the Anomalous Couplings*) gives a brief theoretical overview of the main features of the SM, and a detailed formalism for the description of the $q\bar{q} \rightarrow Z\gamma$ process which is sensitive to anomalous couplings between Z's and photons. Various corrections to the tree-level formalism, as well as the sensitivity to the anomalous couplings of indirect low energy experiments, are also discussed in this Chapter. Some models of the anomalous couplings are reviewed. Chapter 3 (*Detector and Monte Carlo*) briefly describes the accelerator and the detector used for the present work, as well as the Monte Carlo program used for detector simulation and precise comparison of the experimental results with the theory. Chapter 4 (*Event Selection*) describes details of the selection of the $p\bar{p} \rightarrow Z\gamma$ events in the e^+e^- and $\mu^+\mu^-$ decay channels of the Z, and backgrounds to this process. Possibilities to study this reaction in the $\nu\bar{\nu}\gamma$ channel are also discussed. Chapter 5 (*Limits on the Anomalous Couplings*) contains the main experimental results, which are the limits on the non-SM couplings between Z bosons and photons. Finally, Chapter 6 (*Conclusions*) summarizes the results obtained in the current work and gives some perspectives of future studies of the anomalous couplings with DØ, and with other detectors at existing and projected high-energy colliders. A comparison of the DØ limits with those previously set by direct and indirect low-energy experiments, as well as with the recent direct results from the CDF [5] and preliminary results from L3 [6] Collaborations, is also provided.

Chapter 2

Theory of the Anomalous Couplings

Into every tidy scheme for arranging the pattern of human life, it is necessary to inject a certain dose of anarchism.

Bertrand Russell, "Sceptical Essays"

2.1 Standard Model Formalism

The Standard Model is based on a fundamental $SU(2)_L \times U(1)_Y$ symmetry. There are 4 independent gauge fields which correspond to this symmetry. We will denote a non-Abelian $SU(2)$ field by W^i_μ, $i = 1,\ 2,\ 3$, and an Abelian $U(1)$ field by B_μ. Here and in what follows Greek letters denote Dirac 4-indices.

We further introduce fermions in such a way that they interact both with vector and axial vector currents (in order to explain parity violation in weak decays), and at the same time respect current conservation. This can be achieved by separating left-handed and right-handed fermion fields. The left-handed fields must transform as isospin doublets under $SU(2)$ symmetry, while right-handed fields are isospin singlets. The leptons are entered in the SM as

$$\begin{pmatrix} \nu_\ell \\ \ell^- \end{pmatrix}_L \text{ and } \ell_R.$$

There are no right-handed neutrino fields in the SM. Similarly, the quarks are introduced as

$$\begin{pmatrix} u_i \\ d'_i \end{pmatrix}_L, \quad u_{iR}, \text{ and } d_{iR}.$$

Here $\ell = \{e, \ \mu, \ \tau\}$, the index i denotes the three quark families, and d'_i are rotated quark fields: $d'_i = \sum_j V_{ij} d_j$, where V_{ij} is the Cabibbo-Kobayashi-Maskawa mixing matrix [7].

Finally, in order to give masses to the gauge bosons via spontaneous local symmetry breaking (LSB) (Higgs mechanism [8]) we need to introduce an isospin doublet of scalar Higgs fields which preserves only a neutral component after LSB occurs:

$$\varphi = \begin{pmatrix} \varphi^+ \\ \varphi^0 \end{pmatrix} \xrightarrow{LSB} \frac{1}{\sqrt{2}} \begin{pmatrix} 0 \\ v + H \end{pmatrix},$$

where v is the vacuum expectation value (vev) of the Higgs field in the spontaneously broken $SU(2)_L \times U(1)_Y$ symmetry, and H is a new Higgs field with zero vev.

The fermion part of the Lagrangian of the SM after spontaneous symmetry breaking has the following form (see, e.g. [9]):

$$\begin{aligned} \mathcal{L}_{\mathcal{F}} &= \sum_i \bar{\psi}_i \left(i\partial\!\!\!/ - m_i - \frac{g}{2} \frac{m_i}{m_W} H \right) \psi_i \\ &- \frac{g}{2\sqrt{2}} \sum_i \bar{\psi}_i \gamma^\mu (1 - \gamma^5)(T^+ W_\mu^+ + T^- W_\mu^-) \psi_i \\ &- e \sum_i q_i \bar{\psi}_i \gamma^\mu \psi_i A_\mu - \frac{g}{2\cos\theta_W} \sum_i \bar{\psi}_i \gamma^\mu (V^i - A^i \gamma^5) \psi_i Z_\mu. \end{aligned} \tag{2.1}$$

Here $\partial\!\!\!/$ is $\gamma^\mu\partial_\mu$, g and g' are coupling constants for the gauge fields W^i_μ and B_μ; $\theta_W \equiv \tan^{-1}(g'/g)$ is the Weinberg angle; $e = g\sin\theta_W$ is the positron electric charge. The new (rotated) gauge fields are $A \equiv B\cos\theta_W + W^3\sin\theta_W$ (massless photon field), $W^\pm \equiv (W^1 \mp iW^2)/\sqrt{2}$, and $Z \equiv -B\sin\theta_W + W^3\cos\theta_W$ (charged and neutral heavy weak boson fields). The weak isospin operators are defined as follows: $T_i = \tau_i/2$, where τ_i are Pauli matrices; $T^\pm = T_1 \mp iT_2$; m_W is the mass of the W boson, and m_i are the masses of fermions. Finally, the vector and axial couplings are $V^i \equiv t^i_{3L} - 2q_i\sin^2\theta_W$, $A^i \equiv t^i_{3L}$, where t^i_{3L} is the weak isospin of the i-th fermion ($+1/2$ for ν_ℓ and u_i; $-1/2$ for ℓ and d'_i), and q_i is the charge of ψ_i in units of e.

In short hand notation the last three terms are often put in the first (kinetic) term by replacing $\partial\!\!\!/$ by $\gamma^\mu D_\mu$, where D_μ is a covariant derivative: $D_\mu = \partial_\mu + igW^j_\mu T_j + ig'\frac{1}{2}B_\mu Y$.

The Lagrangian (2.1) contains only the fermion part and does not include cubic and quartic self interactions of W, Z, and γ gauge bosons, as well as cubic and quartic Higgs boson self couplings, and couplings of the Higgs field to the gauge bosons.

The Higgs part of the Lagrangian has the following form:

$$\begin{aligned}
\mathcal{L}_\varphi &= \frac{1}{2}(\partial H)^2 - \frac{1}{2}m_H^2 H^2 \\
&- \frac{1}{8}m_H^2 v^2\left(-1 + \frac{4H^3}{v^3} + \frac{H^4}{v^4}\right) \\
&+ \frac{1}{4}g^2 W^+_\mu W^{-\mu}(v+H)^2 + \frac{1}{8}\,\frac{g'^2}{\sin^2\theta_W} Z_\mu Z^\mu (v+H)^2,
\end{aligned}$$

where m_H is the mass of the Higgs particle. It contains kinetic and mass terms for the Higgs scalar (the first two terms), as well as W and Z boson mass terms:

$$m_W^2 W_\mu^+ W^{-\mu} + \frac{1}{2} m_Z^2 Z_\mu Z^\mu,$$

with $m_W = gv/2$, $m_Z = g'v/2\sin\theta_W = m_W/\cos\theta_W$. The second line describes cubic and quartic self interactions of the Higgs field, and the remaining pieces of the last two terms:

$$\left(\frac{1}{4} g^2 W_\mu^+ W^{-\mu} + \frac{1}{8}\frac{g'^2}{\sin^2\theta_W} Z_\mu Z^\mu\right)(H^2 + 2vH)$$

are responsible for WWH, ZZH, $WWHH$, and $ZZHH$ interactions.

Finally, the gauge boson part of the Lagrangian has the following form:

$$\mathcal{L_W} = -\frac{1}{4} W_{i\mu\nu} W_i^{\mu\nu} - \frac{1}{4} B_{\mu\nu} B^{\mu\nu}, \tag{2.2}$$

with

$$\begin{aligned} W_{i\mu\nu} &\equiv \partial_\mu W_{i\nu} - \partial_\nu W_{i\mu} - g f_{ijk} W_{j\mu} W_{k\nu}; \\ B_{\mu\nu} &\equiv \partial_\mu B_\nu - \partial_\nu B_\mu, \end{aligned}$$

where f_{ijk} are the structure constants of the weak isospin group: $[T_i, T_j] = i f_{ijk} T_k$. In the standard representation of the $SU(2)$ group $T_i = \frac{1}{2}\tau_i$, and $f_{ijk} = \epsilon_{ijk}$ (totally antisymmetric tensor). This part of the Lagrangian is responsible for cubic (WWZ, $WW\gamma$) and quartic ($WWWW$, $WWZZ$, $WWZ\gamma$, and $WW\gamma\gamma$) self-interactions of the gauge fields.

There are three free independent parameters which determine the gauge sector of the standard model: g, g', and $v = 2m_W/g = (\sqrt{2}G_F)^{-\frac{1}{2}}$. For low energy electroweak interactions an equivalent set of parameters is normally used: the fine structure constant $\alpha = e^2/(4\pi) = 1/(137.035\,989\,5 \pm 0.000\,006\,1)$ [9], the Fermi coupling constant $G_F = (1.166\,39 \pm 0.000\,02) \cdot 10^{-5}$ GeV^{-2} [9], and the Weinberg angle θ_W. The first two parameters have been measured very precisely using the quantum Hall effect [10] and muon lifetime experiments [11], leaving θ_W as the single parameter to be pinned down. (After the discovery of the W and Z bosons, this last parameter has been precisely measured at LEP and SLC to be $\sin^2\theta_W = 0.2319 \pm 0.0005$ [9].)

In the mass sector of the Lagrangian all masses except that of the Higgs boson and the mass of top quark m_t have been measured[1], so the SM has a very strong predictive power.

Another essential feature of the SM is renormalizability, which was first "guessed" by Weinberg and later proved by t'Hooft [13]. The fact that the SM is renormalizable makes it possible to calculate radiative corrections to the SM in a well defined way. The accuracy of the most precise current experiments (such as measurement of the line shape of the Z resonance at LEP [14]) is high enough to make them sensitive to $\mathcal{O}(\alpha)$ radiative corrections.

2.2 Self-Interactions of Gauge Bosons

An interesting theoretical question which arises in the SM is the self-interaction of gauge fields via trilinear couplings between the carriers, i.e. the vector bosons. (Quartic self-interactions of the gauge fields are beyond

[1]Some evidence for top quark production in $p\bar{p}$ collisions at the Tevatron was recently reported by the CDF Collaboration [12]; the claimed value of the top mass is $m_t = 174 \pm 10^{+13}_{-12}$ GeV$/c^2$.

consideration of this work.)

The W bosons in the SM carry electric charge ($q = \pm e$) and weak isospin charge ($I^W = \pm 1$). The photon and the Z boson are neutral ($q = 0,\ I^W = 0$) and Majorana particles, i.e. they are their own antiparticles.

From the form of the gauge part of the SM Lagrangian (2.2) it is clear that in the SM at tree level the only allowed self-interactions between gauge fields are the interactions between charged and neutral bosons. (These types of interactions for the case of photons are well known and described in QED.) Thus, among all $V_1V_2V_3$ vertices, where V_i is a gauge boson ($V = \{\gamma,\ W^+,\ W^-,\ Z\}$), only the $W^+W^-\gamma$ and W^+W^-Z vertices are non-zero in SM.

The $W^+W^-\gamma$ vertex was first measured directly by the UA2 Collaboration at CERN [15]. The result is consistent with the SM prediction. However the experimental errors are rather large. Both $W^+W^-\gamma$ and W^+W^-Z vertices are currently studied with much higher precision by the CDF and DØ Collaborations at the Fermilab Tevatron, and the results [16, 17] are consistent with the SM. Even more stringent limits on non-SM couplings are expected from future Tevatron experiments and LEP II by the end of this century, and from LHC at the beginning of the next one.

This Thesis is devoted to the study of the trilinear couplings between the neutral gauge bosons, which were never directly tested before. Among the four possible trilinear vertices, ZZZ, $ZZ\gamma$, $Z\gamma\gamma$, and $\gamma\gamma\gamma$, only the first three are allowed by electromagnetic gauge invariance. All of them vanish in SM at tree level. The triple Z vertex, which corresponds to a Z-pair in the final state, is not accessible at present Tevatron energies and luminosities, and can be studied with a reasonable sensitivity only at LEP II operating at center mass energy above $2m_Z$, or at the next generation of hadron colliders. Thus, the current study is restricted to the test of the $ZZ\gamma$ and $Z\gamma\gamma$ vertices, which were first discussed in Ref. [18].

2.3 Probing $ZZ\gamma$ and $Z\gamma\gamma$ Vertices in $q\bar{q}$ Interactions

In this section we discuss in detail the general features of the $ZZ\gamma$ and $Z\gamma\gamma$ vertices in $q\bar{q}$ interactions. In what follows we consider the SM to be valid apart from possible anomalies in these vertices. In particular, we assume that the couplings between quarks or leptons and Z bosons or photons are as predicted by the SM, as has been shown experimentally, e.g. by precise measurement of the leptonic and hadronic widths of the Z at LEP [14].

We will also discuss limits on the anomalous couplings originating from S-matrix unitarity, interference of the trilinear diagram with other types of the diagrams, as well as radiative and QCD corrections to the tree-level diagrams.

2.3.1 $ZZ\gamma$ and $Z\gamma\gamma$ Vertices

Let us consider the general $ZV\gamma$ vertex (see Fig. 2.1), where $V = Z$ or γ. As it was first shown in [19], such a vertex can most generally be described by just four free parameters, h_1^V, ..., h_4^V, assuming only electromagnetic gauge invariance and Lorentz invariance. This can most easily be seen from the following helicity argument. The massless photon of the final state can have only two helicities, -1 or $+1$. The massive Z boson can have in addition helicity 0, which restricts the possible number of different helicity amplitudes for the right side of the diagram in Fig. 2.1 to $2 \times 3 = 6$. However, for the assumption of essentially massless quarks there is no scalar component in the $q\bar{q}V$ vertex, so the virtual boson V is produced purely in the s-channel. Thus, the two combinations which correspond to the opposite helicities of the photon and Z in the final state are excluded, because they require a total helicity of ± 2 for the virtual V, which cannot be accessed via an s-channel exchange of a vector particle. Thus, only four out of six possible helicity amplitudes are allowed, and they generally correspond to four different matrix elements for the trilinear vertex, or four different couplings.

The vertex function for the $ZZ\gamma$ vertex, as derived in [19], has the following form (see Fig. 2.1 for 4-momentum notations):

$$\begin{aligned}
\Gamma^{Z\gamma Z}_{\alpha\beta\mu} &= \frac{P^2 - q_1^2}{m_Z^2} \left\{ h_1^Z (q_2^\mu g^{\alpha\beta} - q_2^\alpha g^{\mu\beta}) \right. \\
&+ \frac{h_2^Z}{m_Z^2} P^\alpha ((P \cdot q_2) g^{\mu\beta} - q_2^\mu P^\beta) \\
&+ h_3^Z \epsilon^{\mu\alpha\beta\rho} q_{2_\rho} \\
&+ \left. \frac{h_4^Z}{m_Z^2} P^\alpha \epsilon^{\mu\beta\rho\sigma} P_\rho q_{2_\sigma} \right\},
\end{aligned} \tag{2.3}$$

where $\epsilon^{\alpha\beta\gamma\rho}$ is a totally antisymmetric tensor, and m_Z is the Z boson mass. Similarly, the $Z\gamma\gamma$ vertex is given by [20]:

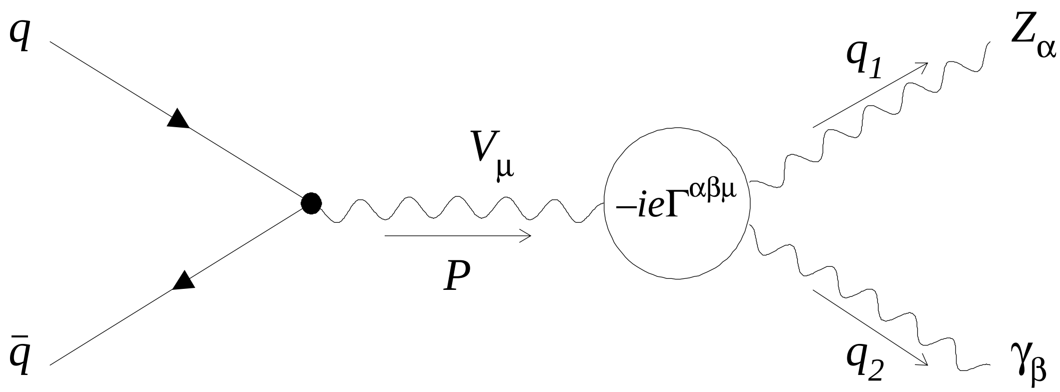

Figure 2.1: Trilinear $ZV\gamma$ vertex in $q\bar{q}$ collisions.

$$
\begin{aligned}
,^{Z\gamma\gamma}_{\alpha\beta\mu} &= \frac{P^2}{m_Z^2}\Bigg\{ h_1^\gamma(q_2^\mu g^{\alpha\beta} - q_2^\alpha g^{\mu\beta}) \\
&+ \frac{h_2^\gamma}{m_Z^2} P^\alpha((P\cdot q_2)g^{\mu\beta} - q_2^\mu P^\beta) \\
&+ h_3^\gamma \epsilon^{\mu\alpha\beta\rho} q_{2_\rho} \\
&+ \frac{h_4^\gamma}{m_Z^2} P^\alpha \epsilon^{\mu\beta\rho\sigma} P_\rho q_{2_\sigma} \Bigg\}.
\end{aligned} \tag{2.4}
$$

Terms proportional to P^μ and q_1^α are omitted from (2.3) and (2.4) since they do not contribute to the cross section. The vertex factor is $ie,^{\alpha\beta\mu}$, which corresponds to the overall coupling constants $g_{ZZ\gamma} = g_{Z\gamma\gamma} = e$. Such a choice does not affect the generality of the expressions (2.3), (2.4); it is simply a definition of the coupling constants h_i^V. In the same fashion the energy scale in the denominator of the overall factor, and in terms proportional to h_2^V, h_4^V is chosen to be the Z mass, because it is a typical mass scale of the trilinear effects. For different mass scales the results can be obtained by a simple scaling [20].

It is important that there is a factor of P^2 in the expression for the $Z\gamma\gamma$ vertex (2.4). As a result, this vertex vanishes when both photons are onshell, which is in agreement with Yang's theorem [21]. This makes it impossible to study the $Z\gamma\gamma$ vertex in two-photon decays of real Z's: one of the photons must be off-shell.

2.3.2 Features of the Coupling Constants

As previously stated (see sec. 2.2), in the SM at tree level, $ZV\gamma$ vertices are zero. Thus, any non-zero couplings h_i^V would mean a violation of the SM, and so the h_i^V are usually referred to as *anomalous couplings.* Some extensions of the SM which predict anomalous couplings will be discussed in sec. 2.5. In this section we are going to discuss general features of the anomalous couplings. Major results discussed here were derived in Refs. [19, 20].

The couplings h_i^V are C-odd dimensionless functions of q_1^2, q_2^2, and P^2. In addition, h_1^V, h_2^V are P-even, and thus violate CP. The other pair: h_3^V, h_4^V, is CP-conserving. As is clear from equations (2.3) and (2.4), h_1^V, h_3^V receive contributions only from operators of dimension ≥ 6, while h_2^V, h_4^V are due to dimension ≥ 8 operators.

To make the anomalous coupling formalism self-consistent, we have to respect the S-matrix unitarity. It was shown in [22] that in order not to violate the unitarity limit, the couplings at high energy should asymptotically approach their SM values, i.e. zero. Therefore, the $ZV\gamma$ couplings have to be energy-dependent, and are thus described by the form factors $h_i^V(q_1^2, q_2^2, P^2)$

which vanish at high q_1^2, q_2^2, or P^2. From the diagram in Fig. 2.1, however, $q_1^2 \approx m_Z^2$, $q_2^2 = 0$, and $P^2 = \hat{s}$. So, only the high $\hat{s}$ behavior should be included in the form factor for the $q\bar{q} \to Z\gamma$ diagrams.

We will use the generalized dipole type of form factors for h_i^V, following Ref. [20]:

$$h_i^V(m_Z^2, 0, \hat{s}) = \frac{h_{i0}^V}{(1+\hat{s}/\Lambda^2)^n}. \tag{2.5}$$

The constraints on the h_{i0}^V can be derived from the partial wave unitarity of the general $f\bar{f} \to Z\gamma$ process [23, 24]. Assuming that only one coupling is non-zero at a time, the following limits can be derived for $\Lambda \gg m_Z$ [20, 25]:

$$\begin{aligned} |h_{10}^{Z/\gamma}|,\ |h_{30}^{Z/\gamma}| &< \frac{(\frac{2}{3}n)^n}{(\frac{2}{3}n-1)^{n-3/2}} \cdot \frac{0.126/0.151\ \mathrm{TeV}^3}{\Lambda^3}, \\ |h_{20}^{Z/\gamma}|,\ |h_{40}^{Z/\gamma}| &< \frac{(\frac{2}{5}n)^n}{(\frac{2}{5}n-1)^{n-5/2}} \cdot \frac{2.1/2.5 \cdot 10^{-3}\ \mathrm{TeV}^5}{\Lambda^5}. \end{aligned} \tag{2.6}$$

From equations (2.6) it is obvious that unitarity is satisfied only for $n > 3/2$ for $h_{1,3}^V$, and $n > 5/2$ for $h_{2,4}^V$. In what follows we will use $n = 3$ for $h_{1,3}^V$ and $n = 4$ for $h_{2,4}^V$. Such a choice ensures the same asymptotic energy behavior of the $h_{1,3}^V$ and $h_{2,4}^V$ couplings. The dependence of the results on the choice of n is discussed in [20].

Both the unitarity limits and the strength of the couplings depend strongly on the scale parameter Λ. Together with the denominator power n, Λ is a parameter of the model. As long as the choice of n is fixed, the scale Λ is the only free parameter. The actual value of Λ is not predicted by the theory. The physical meaning of this parameter is a "compositeness scale", or scale for new physical phenomena. It is reasonable to expect Λ to be at least of the order of a few hundred GeV. If Λ is too small (say, of the order of m_Z), one would expect the real Z boson to have properties different from what the SM predicts, but there is no evidence for such a difference [14]. Very large values of Λ, on the other hand, will effectively suppress any effects of anomalous couplings due to unitarity limits up to very high energies, which is also unnatural. We will discuss the dependence of the results on the value of Λ scale in Chapter 5.

The anomalous couplings h_i^V are related to the dipole and quadrupole transition moments of the Z boson. Unlike the $WW\gamma$ case, where the anomalous couplings contribute to the above moments of the real particle (i.e. W [26]), $Z\gamma$ couplings do not affect the magnetic or electric moments of the Z boson itself, since the Z is a Majorana particle and thus all its moments are equal to 0 due to the CPT-theorem [27]. The CP-even combinations of h_3^V, h_4^V correspond to the electric dipole and magnetic quadrupole transition moments of the $ZV\gamma$ vertex; the CP-odd combinations of h_2^V, h_4^V correspond to magnetic dipole and electric quadrupole moments. The actual relation between the couplings and moments is rather complicated and depends both on the center of mass (CM) energy ($\sqrt{\hat{s}}$) and on the momentum of the final state photon [28] (unlike the $WW\gamma$ case).

2.3.3 Probing the $ZZ\gamma/Z\gamma\gamma$ Vertices at the Tevatron

Final State Signature and Feynman Diagrams

The formalism of the previous section allows one to calculate the matrix elements for the vertex in Fig. 2.1. This vertex corresponds to a Z boson and a photon on the right-hand side of the reaction. However, experimentally the presence of a Z boson is inferred only by detecting its decay products.

The hadronic modes of Z decay are contaminated with a large QCD multijet background, so at present it is possible to select Z-events only in the leptonic decay modes. Furthermore, it is a rather challenging experimental task to detect the $Z \to \tau^+\tau^-$ decay channel in hadronic collisions, so we will consider only $Z \to e^+e^-$, $Z \to \mu^+\mu^-$, and $Z \to \nu\bar{\nu}$ decay modes. Thus, the final state signature for probing the $ZV\gamma$ vertices is $\ell\bar{\ell}\gamma$, where $\ell = e,\ \mu,$ or ν.

However, the trilinear vertex is not the only one contributing to this final state. The whole set of tree level Feynman diagrams for the processes which produce a lepton pair and a photon in the final state are shown in Fig. 2.2. There are three types of reactions which contribute to the $\ell\bar{\ell}\gamma$ final state. Diagrams a) and b) represent the so-called initial state radiation, when the hard photon is emitted via *bremsstrahlung* of an incoming antiparton (a) or parton (b). Diagram c) corresponds to the already discussed trilinear coupling (or self-interaction) between gauge bosons, and it vanishes in the SM (see sec. 2.2). The only possible combinations of gauge bosons for the anomalous diagram (c) are $ZZ\gamma$ and $Z\gamma\gamma$, since the $\gamma\gamma\gamma$ vertex is prohibited (see sec. 2.2). Finally, the diagrams d) and e) describe radiative decay (or final state radiation), when the photon is emitted by one of the final state leptons, produced mainly in the decays of on-shell Z's. In what follows, we will refer to the diagrams of these three types as to *production* (a-b), *trilinear* (c), or *decay* (d-e) diagrams. It is important that for the neutrino decay channel of

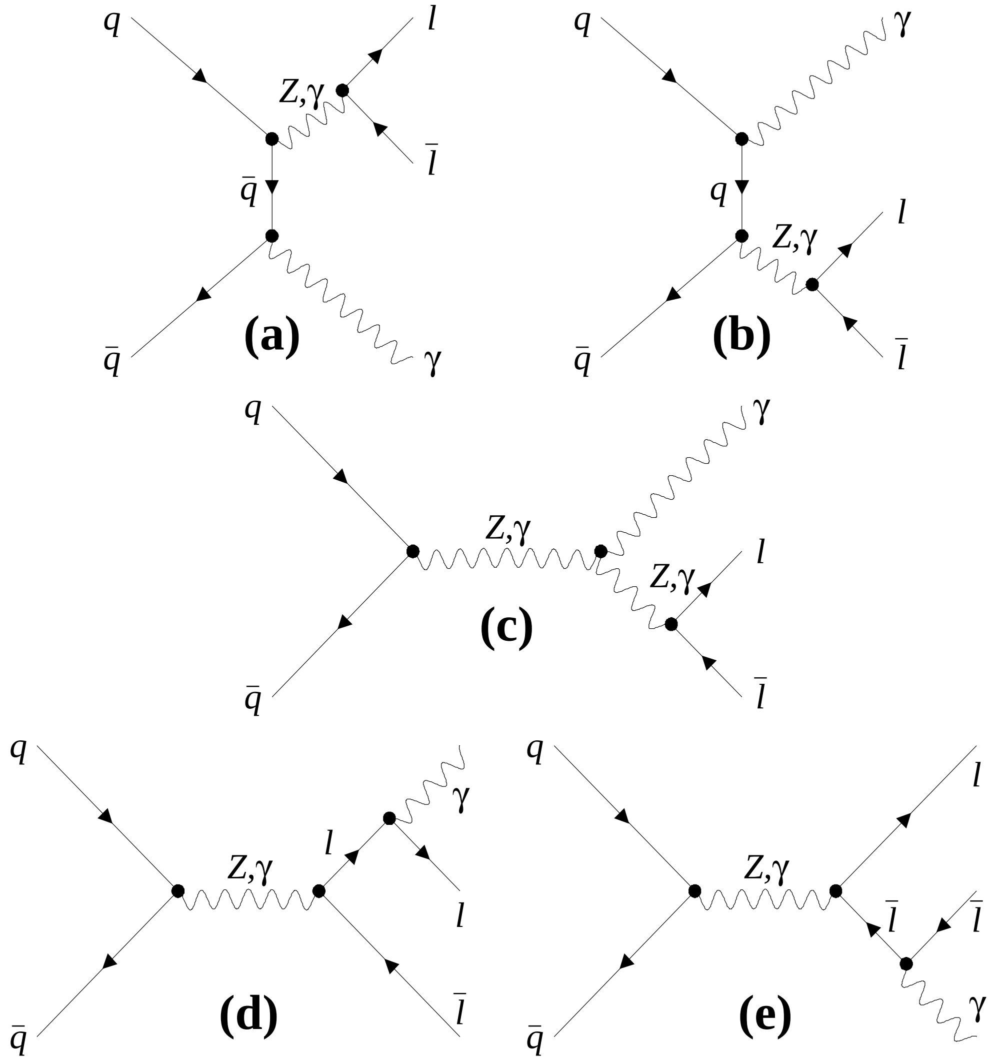

Figure 2.2: Tree level Feynman diagrams for the $q\bar{q} \to \ell\bar{\ell}\gamma$ processes: (a,b) initial state radiation, (c) trilinear coupling, and (d,e) radiative decay.

the Z ($\ell = \{\nu_e,\ \nu_\mu,\ \nu_\tau\}$) the decay diagrams vanish as well, because neutrinos do not interact with photons.

Theoretical calculations of the SM and anomalous cross sections for the whole set of processes pictured in Fig. 2.2 were done by U. Baur and E.L. Berger who kindly provided us with a Monte Carlo generator [20] suitable for obtaining various differential cross sections for the $p\bar{p} \rightarrow \ell^+\ell^-\gamma + X$ and $p\bar{p} \rightarrow \nu\bar{\nu}\gamma + X$ reactions, where X denotes associated QCD jets and soft particles.[2] These calculations take into account finite Z-width effects, interference effects between the diagrams in Fig. 2.2, and a simple detector simulation. We further modified the code and incorporated a more sophisticated and realistic simulation of the DØ detector to enable a more precise comparison between the data and theoretical predictions (see sec. 3.7). However, all numerical results of the current (theoretical) section are obtained with the detector simulation switched off.

The main result of these calculations is that the cross section of the $p\bar{p} \rightarrow Z\gamma$ reaction for the anomalous coupling case ($h^V_{i0} \neq 0$) is *larger* than for the SM case. This means that the diagram in Fig. 2.2 (c) interferes *constructively* with the rest of the diagrams, which gives a very favorable experimental signature for the anomalous couplings: an excess of $\ell\bar{\ell}\gamma$ or $\gamma \not\!\!E_T$ events.

The cross section of $\ell\bar{\ell}\gamma$ production can be expressed as a bilinear form of the couplings h^V_{i0} with a minimum located very close to the SM values (h^V_{i0} = 0). Thus, it is possible to set limits on the anomalous couplings from a simple counting experiment. There are, however, more advanced and sensitive methods of obtaining these limits, and they will be discussed later in this section and in Chapter 5.

---

[2]In what follows we will omit the X term in the reaction notations, always assuming the inclusive $Z\gamma$ production.

$p\bar{p} \to \ell^+\ell^-\gamma$

The expression for the cross section for

$$p\bar{p} \to \ell^+\ell^-\gamma \tag{2.7}$$

exhibits several different divergences [20]. One is a *collinear divergence* which occurs when the photon is emitted parallel to one of the leptons. Another one is an *infrared divergence* which occurs when the photon has vanishing energy. However, a comparison with a real experiment does not suffer from these theoretical divergences in the Lagrangian for two reasons: (i) it is impossible to detect a photon below a certain energy threshold, and (ii) in order to distinguish between the photon and a lepton, one needs a sufficient spatial separation between these two objects in the detector.

Thus, any real experiment measures the cross section for (2.7) only in a fraction of the total available phase space. It is natural to perform theoretical calculations only for such restricted kinematics. In order to study the signatures for anomalous couplings, we will impose a set of basic cuts, typical for a general-purpose detector working at high energy hadron colliders (such as the DØ or CDF detector). The actual cuts used for event selection (see Chapter 4) are somewhat different from these basic cuts, but the qualitative behavior of the various kinematical distributions we are going to study remains the same. At this point we do not introduce any corrections for momentum smearing and do not consider the detection efficiencies, except for taking into account the finite acceptance of the detector for leptons and photons. The results in this section are calculated for the Tevatron energy ($\sqrt{s} = 1.8$ TeV) and correspond to a single lepton channel of Z-decay (e.g. e^+e^-). The MRSD$-'$ [29] set of structure functions is used in the simulation (see sec. 3.7 for the discussion of the structure function dependence of the cross section). The effects of next to leading order logarithmic (NLL) QCD corrections are simulated via a scaling factor $k = 1 + \frac{8\pi}{9}\alpha_s \approx 1.34$ (see sec. 2.3.4). The anomalous coupling contribution is calculated for a form factor scale of $\Lambda = 500$ GeV.

The basic set of cuts for the $\ell^+\ell^-\gamma$ production (2.7) is defined as follows:

$$\begin{gathered} p_T^{\ell^\pm} > 15 \text{ GeV}/c, \quad p_T^{\gamma} > 10 \text{ GeV}/c; \\ |\eta_{\ell^\pm}| < 3.0, \quad |\eta_\gamma| < 3.0; \\ \Delta R_{\ell^\pm\gamma} \equiv \sqrt{(\Delta\phi_{\ell^\pm\gamma})^2 + (\Delta\eta_{\ell^\pm\gamma})^2} > 0.7. \end{gathered} \tag{2.8}$$

Here p_T is the transverse momentum ($p_T \equiv \sqrt{p_x^2 + p_y^2}$ in the lab frame with z along the beam direction); η is the pseudorapidity of the particle: ($\eta \equiv \tanh^{-1}(\cos\theta)$; θ and ϕ are polar and azimuthal angles of the particle momentum in the lab frame, see sec. 3.2.1). In what follows we will refer to ΔR as to the *separation* (in η, ϕ space).

The theoretical cross section of the reaction (2.7) within this set of cuts per one lepton channel is $\sigma(SM) = 2.06$ pb. We will compare the SM and anomalous cases for two different couplings: $h_{30}^Z = 2.5$, and $h_{40}^Z = 0.5$ (varying only one coupling at a time). The theoretical cross section for the anomalous case is somewhat higher: $\sigma(h_{30}^Z = 2.5) = 2.85$ pb, $\sigma(h_{40}^Z = 0.5) = 2.49$ pb. The effect of the anomalous CP-violating h_{10}^Z/h_{20}^Z couplings is very similar (both qualitatively and quantitatively) to that of h_{30}^Z/h_{40}^Z. The contribution of the h_{i0}^γ couplings is a few per cent less than that of the h_{i0}^Z couplings of

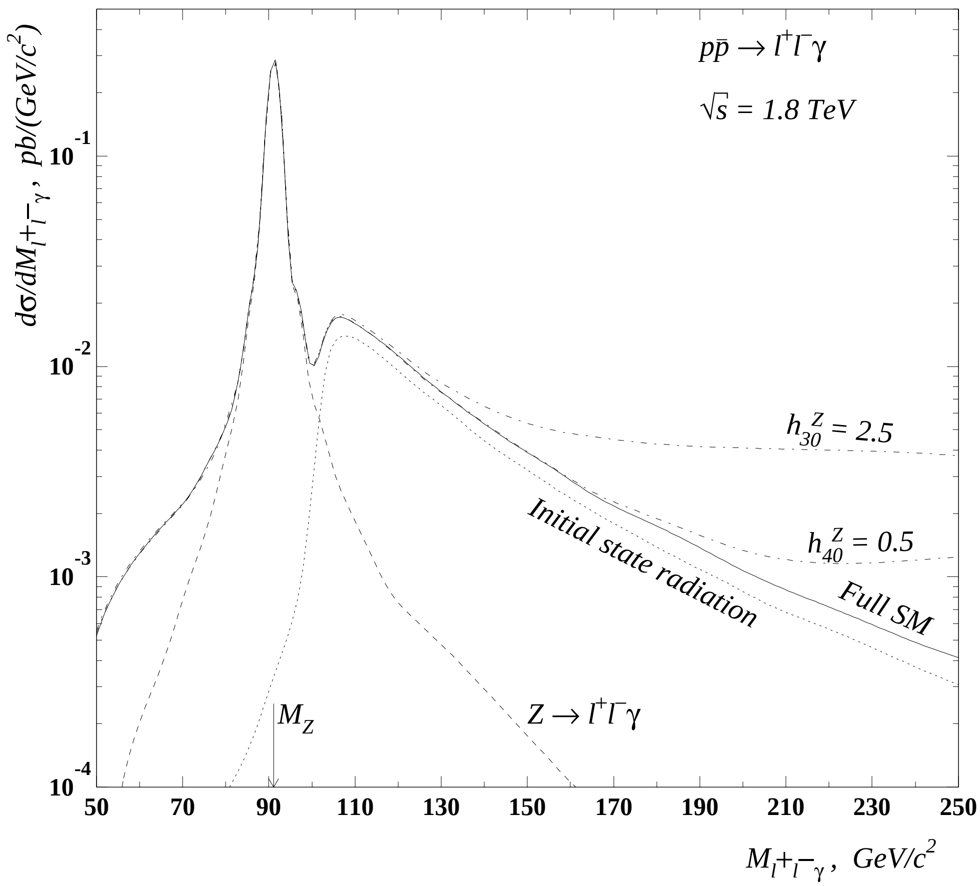

Figure 2.3: Invariant mass of the $\ell^+\ell^-\gamma$ system produced in the reaction (2.7) for different processes contributing to the $\ell^+\ell^-\gamma$ final state. For notations see text.

equal strength. This is true for all plots in this section, so this fact will not be emphasized further, and we will discuss only the signature of the h_{30}^Z and h_{40}^Z couplings.

The following five figures show different kinematical distributions for the final state particles in the reaction (2.7). The invariant mass distribution of the $\ell^+\ell^-\gamma$-system produced in (2.7) is shown in Fig. 2.3. The solid line corresponds to the full SM case. The dashed line shows the part of the SM cross section from the decay diagrams only (see Fig. 2.2 (d, e)), with a real Z produced in the s-channel. As one would expect, a clear Z-peak is seen in the three-body mass spectrum for the decay process. The contribution of the off-shell photon exchange in these diagrams (Drell-Yan production of $\ell^+\ell^-$ pair) is important only at masses below Z-peak and at high masses. It accounts for the difference between solid and dashed (dotted) lines at the lower (upper) edge of the plot. The dotted line represents the contribution of the production diagrams (see Fig. 2.2 (a,b)), or the initial state radiation. It is concentrated at masses above the Z mass, and clearly separated from the decay diagram contribution. At invariant masses $m_{\ell^+\ell^-\gamma} > 100$ GeV/c^2 the production diagrams dominate in the cross section. The sharp dip just above Z mass is due to the $p_T^\gamma > 10$ GeV/c cut. Finally, dash-dotted lines show the anomalous cross sections for the case of $h_{30}^Z = 2.5$ (top) and $h_{40}^Z = 0.5$ (bottom). The notations in the following figures of this section are the same as in Fig. 2.3.

It is important to point out that the effects of anomalous couplings are significant only for high masses of the $\ell^+\ell^-\gamma$ system, or at high $\hat{s}$. This is the reason why one needs a high energy collider to study anomalous trilinear couplings. Note that the effects of h_{30}^Z coupling become noticeable at smaller values of $\hat{s}$ than those of h_{40}^Z, which is a direct consequence of different powers of $\sqrt{\hat{s}}/m_Z$ for h_3^Z and h_4^Z in the vertex function (2.3). At very high energies ($\sqrt{\hat{s}} \gg \Lambda$), however, the asymptotic behaviors of these two couplings become the same due to the appropriate choice of the denominator power in the form factors (2.5) (see sec. 2.3.2).

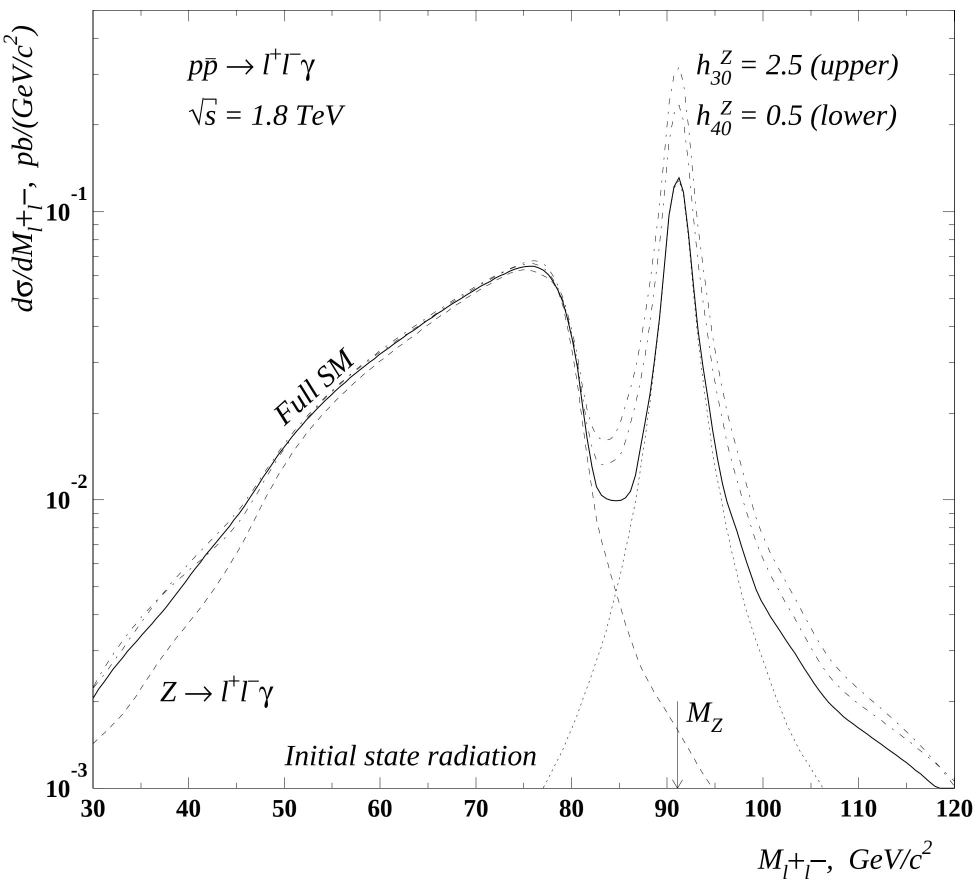

Figure 2.4: Invariant mass of the $\ell^+\ell^-$ system produced in the reaction (2.7) for different processes contributing to the $\ell^+\ell^-\gamma$ final state. For notations see text.

The invariant mass spectrum of the $\ell^+\ell^-$ pair is shown in Fig. 2.4. Here the initial state radiation and anomalous coupling effects are concentrated in the Z-peak region, whereas the decay diagrams populate the lower part of the spectrum. Again, decay and production diagram contributions are clearly separated. The strong dip at ≈ 80 GeV$/c^2$ is due to the finite p_T^γ cut, similar to that in the previous plot.

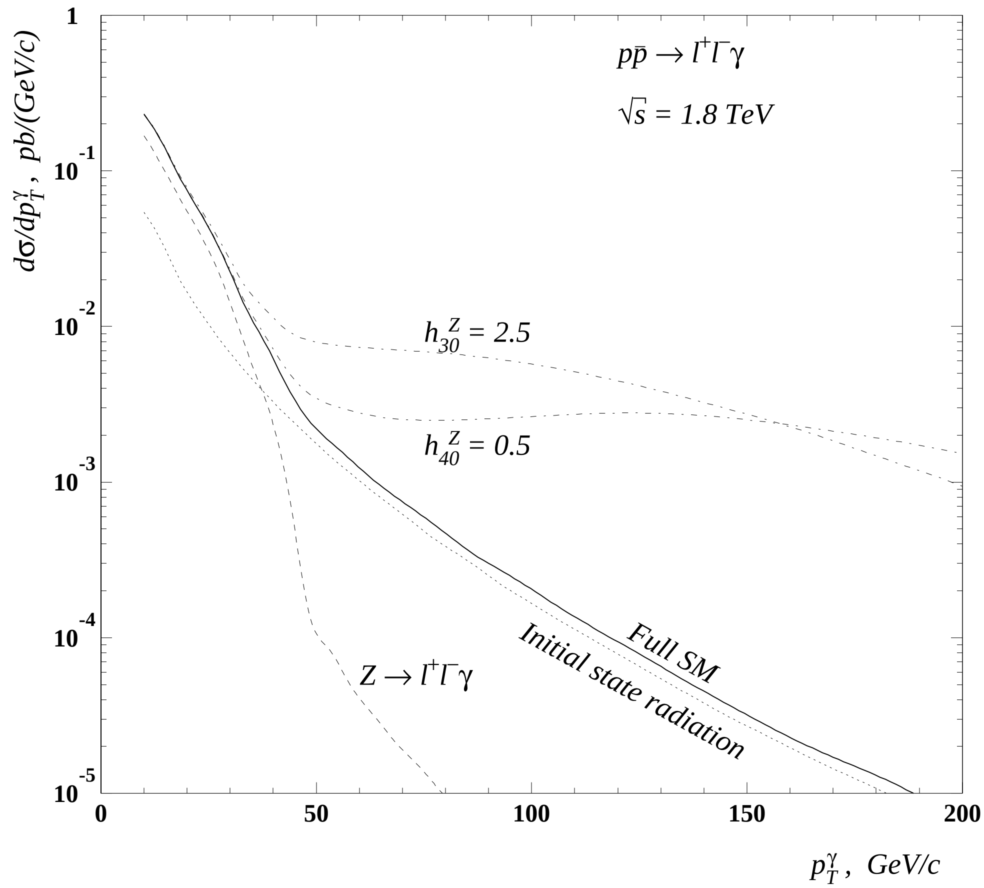

Figure 2.5: The p_T spectrum of the photon produced in the $p\bar{p} \to \ell^+\ell^-\gamma$ reaction for different processes contributing to this final state. For notations see text.

The most characteristic distribution for distinguishing between the SM and the anomalous coupling cases is the p_T^γ spectrum, as shown in Fig. 2.5. Anomalous couplings result in the emission of harder photons, and thus fitting the shape of the observed p_T^γ spectrum provides the tightest constraints on the anomalous couplings (see sec. 5.2). The $p_T^\gamma > 10$ GeV/c cut essentially does not affect the contributions from the anomalous couplings.

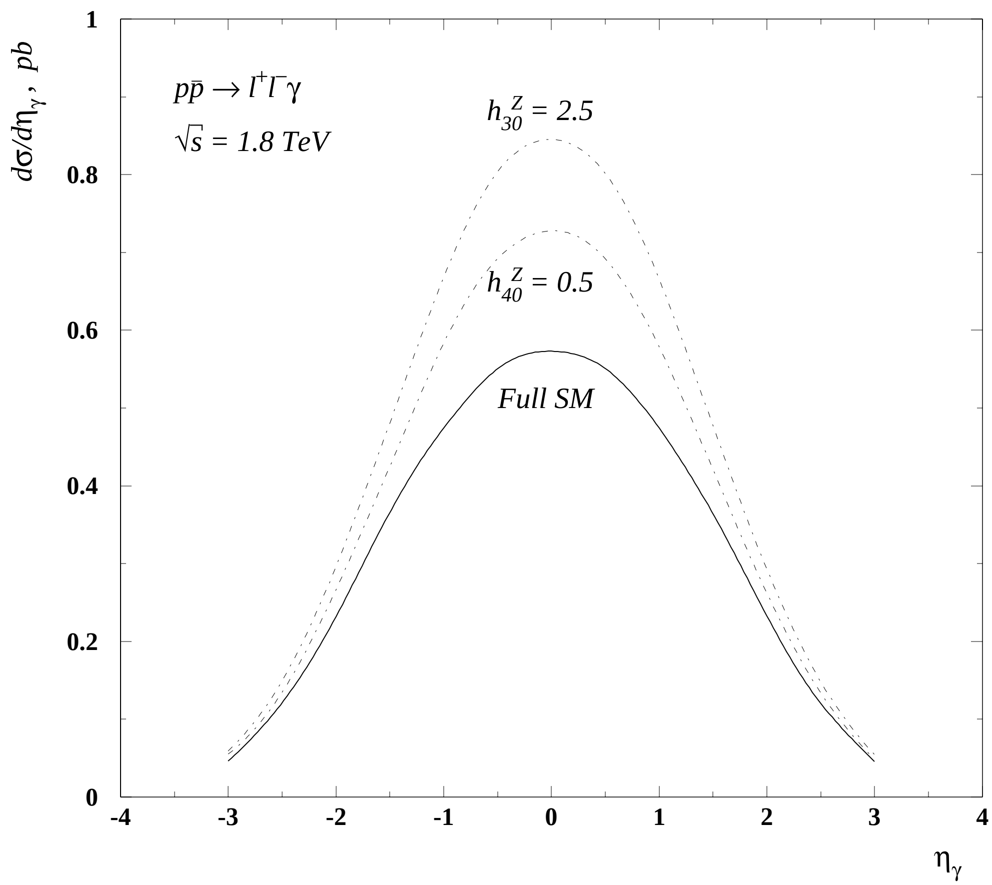

Figure 2.6: Pseudorapidity distribution for the photon produced in the $p\bar{p} \to \ell^+\ell^-\gamma$ reaction. For notations see text.

The photon pseudorapidity distribution is shown in Fig. 2.6. The contribution from the anomalous couplings is clearly concentrated in the central region. Both decay and initial state radiation contributions have the same bell shape, so they are not shown. A coverage of $|\eta_\gamma| < 2-3$ is thus quite sufficient to study the anomalous effects.

Finally, the separation distribution is shown in Fig. 2.7. Here we plot the ΔR between the photon and the closest lepton. As one would expect, the decay

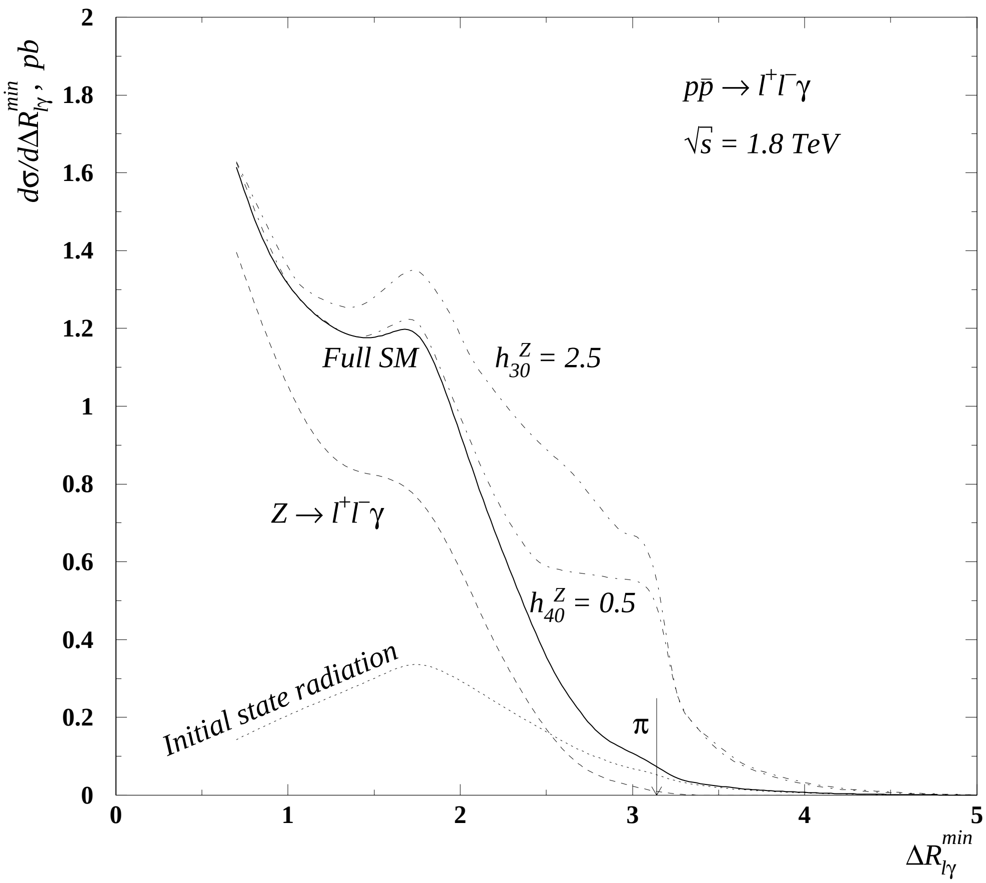

Figure 2.7: Minimum separation between the photon and charged leptons produced in the reaction (2.7) for different processes contributing to the $\ell^+\ell^-\gamma$ final state. For notations see text.

diagram contributions peak at low separations between one of the leptons and the photon, because of collinear nature of *bremsstrahlung*. The peak is not seen in the figure due to the ΔR-cut (2.8); instead there is a rapid decrease of the decay contributions as ΔR increases. Both initial state radiation and anomalous diagrams contribute for high lepton-photon separation. For the trilinear diagram (Fig. 2.2 (c)) the separation peaks approximately at π, which reflects the fact that the Z and the photon are very central and are emitted back-to-back with a very high transverse momentum which collapses both leptons of Z decay in the lab frame into a narrow cone around the parent Z momentum. The chosen cut $\Delta R \equiv \min(\Delta R_{\ell^+\gamma},\, \Delta R_{\ell^-\gamma}) > 0.7$ has essentially no effect on the anomalous coupling contribution.

Overall, there are significant differences between the differential cross sections of the reaction (2.7) in the SM and for anomalous couplings. Besides an increase of the total cross section for (2.7), photons produced by trilinear $ZV\gamma$ interactions have high transverse momenta, are central, and have a large separation from the leptons originating in the Z decay.

A potential background to the $p\bar{p} \to \ell^+\ell^-\gamma$ process originates from the $Z+j$ production with the jet hadronizing as a leading π^0. Such a jet might fake a photon in the detector due to the dominant $\pi^0 \to \gamma\gamma$ decay with two photon showers overlapping in the electromagnetic calorimeter. This background was estimated to be less than a few percent in [20] using the jet faking photon probability measured by the UA2 Collaboration [15] and a parton level Monte Carlo. A precise determination of this background for the DØ detector (using the real data) is discussed in sec. 4.5. This analysis confirms that the $Z+j$ background is small (of the order of few per cent) for DØ.

$p\overline{p} \to \nu\overline{\nu}\gamma$

In this section we will briefly describe the effects of the anomalous couplings in the other experimentally observable decay channel of the Z: $Z \to \nu\bar{\nu}$, which corresponds to a $\gamma \not{E}_T$ signature. Although $Z\gamma$ production in this decay channel has not yet been experimentally observed, it is interesting to explore the opportunities for studying anomalous couplings in the reaction

$$p\bar{p} \to \nu\bar{\nu}\gamma. \tag{2.9}$$

There are several very attractive features to this process. First, the decay diagrams (Fig. 2.2 (d,e)) vanish for the neutrino decay channel of the Z. Thus, the sensitivity to the anomalous couplings in reaction (2.9) should be higher than that in the process (2.7). Second, the observable anomalous cross section in the neutrino channel by itself is higher than that for the charged Z decay mode because $\mathrm{BR}(Z \to \nu\bar{\nu}) \approx 3 \cdot \mathrm{BR}(Z \to e^+e^- + \mu^+\mu^-)$ [9], and because the "acceptance" for neutrinos is not restricted by the detector geometry.

For the $Z \to \nu\bar{\nu}$ decay channel the basic set of cuts can be very simple:

$$p_T^\gamma > 10 \text{ GeV}/c, \ \not{E}_T \ > 10 \text{ GeV}, \ |\eta_\gamma| < 3.0. \tag{2.10}$$

At the Monte Carlo level, the $\not{E}_T$ requirement is satisfied automatically because of the transverse energy conservation. Experimentally, however, one needs an explicit $\not{E}_T$ cut because of the p_T-kick of the $Z\gamma$ system due to associated jet production.

The only observables in reaction (2.9) are the transverse momentum and the pseudorapidity of the photon. Contributions from the anomalous couplings are concentrated in the central region, as was the case for the charged lepton decay mode of the Z. Therefore the most interesting distribution is again the p_T^γ spectrum, as shown in Fig. 2.8 for the SM case and for the case of two different anomalous couplings: $h_{30}^Z = 2.5$ and $h_{40}^Z = 0.5$. The effect of the

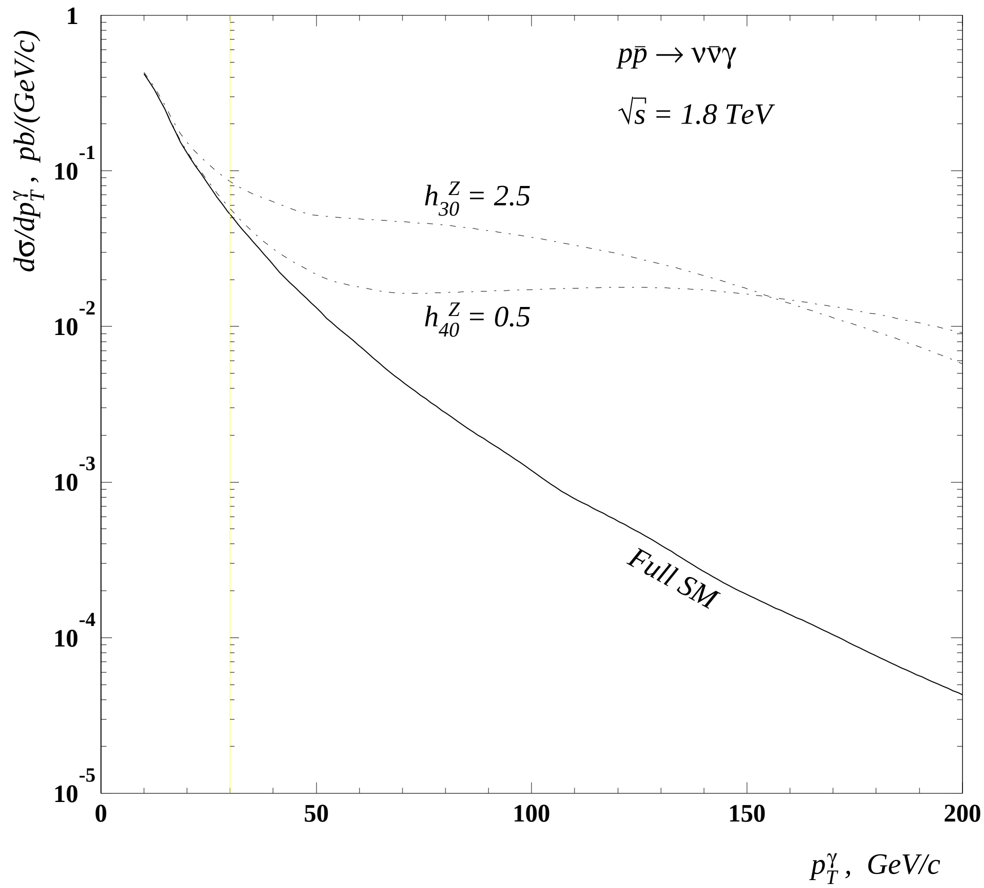

Figure 2.8: The p_T spectrum of the photon produced in the $p\bar{p} \to \nu\bar{\nu}\gamma$ reaction for the SM and anomalous coupling cases. For notations see text.

anomalous couplings is similar to that for the $\ell^+\ell^-\gamma$ final state. Quantitatively, however, it is stronger than for the charged decay mode of the Z, as one would expect. The theoretical cross sections for the SM and the anomalous cases for the set of cuts (2.10) for all three neutrino channels are as follows: $\sigma(SM) = 4.15$ pb, $\sigma(h^Z_{30} = 2.5) = 9.44$ pb, $\sigma(h^Z_{40} = 0.5) = 6.87$ pb. The anomalous and the SM cross sections differ by a factor of 2, which is to be compared with an increase of about 30% for the $Z \to \ell^+\ell^-$ decay mode.

The price for these advantages in the $\nu\bar{\nu}\gamma$ channel is two additional QCD background sources. The first one is dijet production with one jet faking the photon, whereas the second one fakes $\not\!\!E_T$ by escaping the detector through the beam-pipe, but still carrying away a significant amount of transverse energy. The probability for such a double-fake is, of course, very small, but the cross section for dijet production is several orders of magnitude higher than that for the reaction (2.9), so the background still might be significant. The other background is from direct photon ($j\gamma$) production with the jet faking $\not\!\!E_T$ by the same mechanism. These two backgrounds are very detector-dependent, and a detailed study for the DØ detector has yet to be done. In addition, there is another very serious instrumental background for this detector due to the $q\bar{q} \to W \to e\bar{\nu}$ production with electron being misidentified as a photon due to the tracking detector inefficiency. This background will be discussed in sec. 4.4. However, simplified calculations of [20] show that both QCD backgrounds are small for $p_T^\gamma > 30$ GeV/c. Such a high p_T cut essentially does not affect the sensitivity to the anomalous couplings, as is clear from Fig. 2.8. The dotted Y-axis in this figure emphasizes the part of the spectrum above this p_T-cut.

2.3.4 Radiative and QCD Corrections

So far we have not discussed how the radiative and QCD corrections to the tree level diagrams (Fig. 2.2) change the signature for the anomalous couplings.

Radiative QED correction calculations at the one loop level ($\mathcal{O}(\alpha)$) for the $ZV\gamma$ vertices can be found in the literature (e.g. [30, 31]). They contribute only

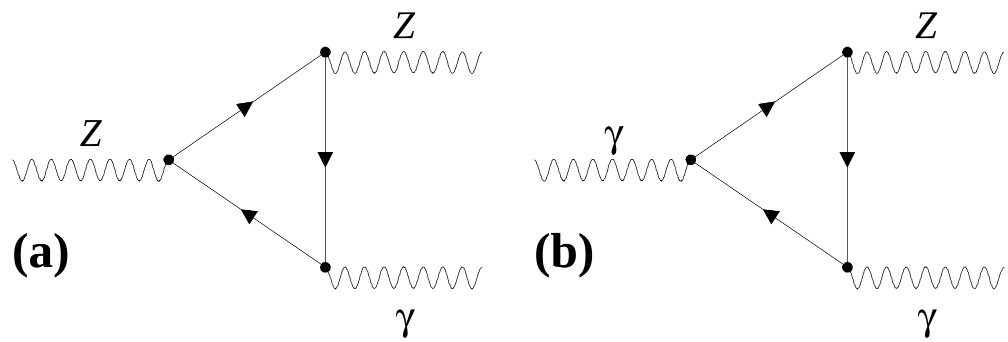

Figure 2.9: Typical loop correction diagrams for the (a) $ZZ\gamma$ and (b) $Z\gamma\gamma$ vertices.

to the CP-conserving couplings h_3^V, h_4^V. Typical triangle diagrams for these corrections are shown in Fig. 2.9. The triangular loops should be summed over the standard set of fermions [31]. The scale of these corrections is much less than the sensitivity of current and imaginable future experiments. For instance, for h_3^Z one finds [20]:

$$2.2 \cdot 10^{-4} < h_3^Z < 2.5 \cdot 10^{-4}$$

for top quark masses between 100 GeV/c^2 and 200 GeV/c^2. Thus, the QED radiative corrections can safely be neglected.

The QCD corrections, however, are important at Tevatron energies. Recently, some of these corrections were calculated to the NLL order for the SM case in the zero Z-width approximation [32]. There are two different types of processes which contribute to the set of diagrams in Fig. 2.2 at that level: virtual corrections and soft gluon emission. Typical Feynman diagrams for these corrections are shown in Fig. 2.10. Both types of the processes are of $\mathcal{O}(\alpha_s)$.

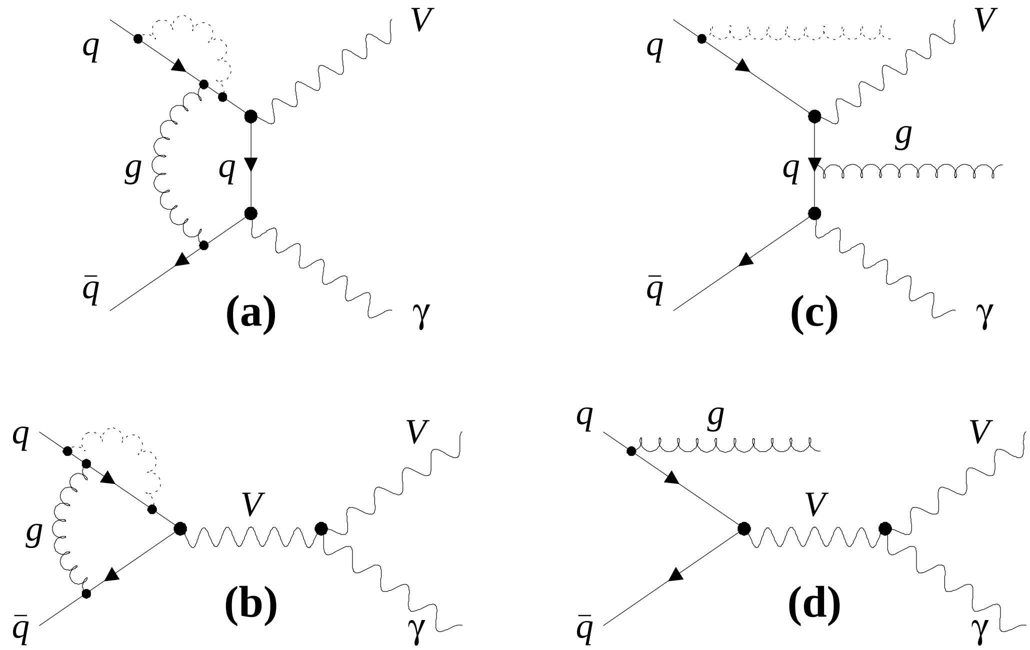

Figure 2.10: Virtual (a,b) and soft gluon radiation (c,d) QCD corrections to the initial state radiation (a,c) and trilinear (b,d) diagrams. Dotted lines show another possible type of gluon emission.

At present, the NLL QCD corrections are available only for the initial state radiation diagrams (see Fig. 2.10 (a,c)). As was shown in [32], the effect of these corrections is mostly a scaling of all discussed distributions by a constant factor. The contribution of $\mathcal{O}(\alpha_s)$ terms to the cross section depends on the set of cuts and is typically about 20% to 40%. These results justify using the so-called k-factor:

$$k = 1 + \frac{8\pi}{9}\alpha_s \approx 1.34$$

to scale the results of the LO calculations on which the Baur-Berger Monte Carlo [20] is based (see sec. 2.3.3 and 3.7).

The recent success of the same authors in calculating the NLL corrections for the anomalous $WW\gamma$ couplings [33] further shows that such a choice for the k-factor is a rather good approximation at Tevatron energies. At the LHC, however, a constant scaling will not work well because there is a significant p_T^γ dependence of the QCD corrections. Thus, the complete NLL calculation must be used for studying anomalous couplings at future higher energy hadron colliders.

Taking into account the QCD corrections is important in searches for anomalous couplings because, like the anomalous couplings themselves, they increase the cross section for the reactions (2.7) and (2.9). (At LHC and higher energies, the QCD corrections also change the shape of p_T^γ spectrum in a way similar to that of the anomalous couplings.)

2.4 Probing $ZZ\gamma$ and $Z\gamma\gamma$ Vertices in Low Energy Experiments

In this section we briefly describe the current limits on the anomalous couplings from low energy experiments. These experiments are sensitive to the anomalous trilinear couplings due to various loop corrections via penguin diagrams (see Fig. 2.11). Unlike the direct tests of couplings in high energy experiments, results at low energies are very sensitive to the regularization scheme and loop cutoff parameter used in the calculations, which makes them rather controversial and model dependent (e.g. [34]).

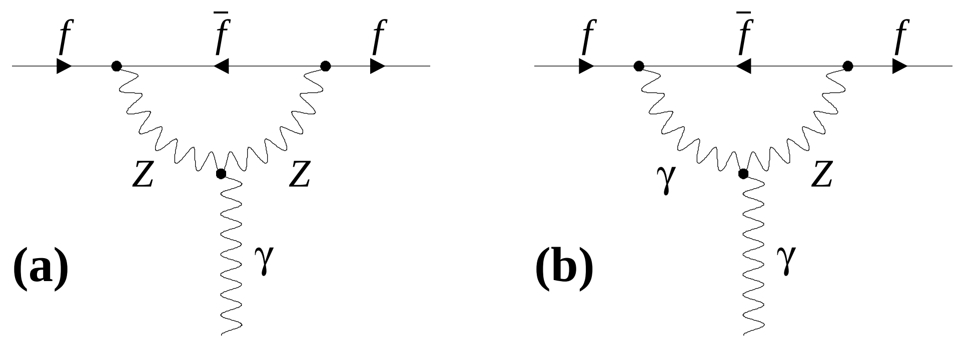

Figure 2.11: Typical loop correction diagrams contributing to the electromagnetic moments of a lepton or quark: a) via $ZZ\gamma$ vertex, b) via $Z\gamma\gamma$ vertex.

Generally, the limits from the loop-diagram corrections can be expressed in the following way [35]:

$$\left| h_{1,3}^V \cdot \left(\log \frac{\Lambda_c^2}{m_Z^2} + a \right) + h_{2,4}^V \cdot b \right| < C. \tag{2.11}$$

Here Λ_c is a cutoff parameter of the loop integration and a, $b = \mathcal{O}(1)$ are parameters depending on the regularization scheme used in the calculations.

It is important to stress that the limits on the anomalous couplings from (2.11) in the $(h_{1,3}^V,\, h_{2,4}^V)$ plane have the shape of a band, i.e. when both couplings are allowed to vary at the same time, the limits go to infinity, even if C is very small. Direct production experiments, on the contrary, produce closed contour limits in the same plane because the total cross section is a bilinear form of any pair of couplings (see sec. 2.3.3 and Chapter 5). However, when only one coupling is varied while the other is held fixed, the limits (2.11) can be very stringent.

The least model-dependent limits on CP-conserving couplings can be extracted from the recent CERN measurement of the gyromagnetic ratio for the muon (the so-called $(g-2)_\mu$ experiment) [36]. Various loop corrections to the magnetic moment of the muon are discussed in [37, 38]. The contributions from the $ZV\gamma$ anomalous couplings to the static electromagnetic properties of a fermion are shown in Fig. 2.11. Only the diagram Fig. 2.11 (b), however, contributes to the gyromagnetic ratio of the muon [38], thus making it sensitive only to the $Z\gamma\gamma$ CP-conserving couplings h_3^γ, h_4^γ. For instance, for $h_4^\gamma = 0$ one obtains at the 95% confidence level (CL) [20]:

$$\left| h_3^\gamma \log\left(\frac{\Lambda^2}{m_Z^2}\right)\right| < 9.$$

The most stringent constraints on the CP-violating couplings are expected from a precise measurement of the neutron electric dipole moment (EDM): $|d_n| < 1.2 \cdot 10^{-25}$ $e \cdot \mathrm{cm}$ [39]. The formalism is similar to that discussed above for the $(g-2)_\mu$ limits, except that the CP-violating couplings contribute to the EDM. The limits on the anomalous $WW\gamma$ couplings from this experiment, calculated in [40], are of the order of 10^{-4} for both dimension six and dimension eight couplings. The limits on the anomalous $ZV\gamma$ couplings have not been calculated yet, but the expected accuracy is of the same order of magnitude: $|h_{1,2}^V| < \mathcal{O}(10^{-4})$ when only one coupling is allowed to vary at a time [28].

Another way of probing anomalous $ZV\gamma$ couplings is to search for radiative Z-decays at LEP and SLC. Since the $Z \to \gamma\gamma$ decay is prohibited by Yang's theorem [21], the only decays sensitive to the anomalous couplings are $Z \to \ell^+\ell^-\gamma$ and $Z \to \nu\bar{\nu}\gamma$. This is a direct and model-independent way to probe anomalous couplings at low energies. However, from Fig. 2.3 it is clear that the contribution of the anomalous couplings to the cross section at the

Z peak is very small (of the order of 1%). So, despite the very high sensitivity of the LEP experiments, the limits are not very tight. For instance, the measurement [41]: $BR(Z \rightarrow e^+e^-\gamma) < 5.2 \cdot 10^{-4}$, translates into the following 95% CL limits on the h_{i0}^V with the assumption of only one coupling varying at a time (form factor scale $\Lambda = 500$ GeV) [20]:

$$|h_{10,30}^Z| < 23, \quad |h_{20,40}^Z| < 62, \quad |h_{10,30}^\gamma| < 14, \quad |h_{20,40}^\gamma| < 99.$$

These limits are far beyond the unitarity limits given by equation (2.6). However, they can be significantly improved by fitting the transverse energy spectrum of the photon produced in association with the Z [6].

The sensitivity of the $Z \rightarrow \nu\bar{\nu}\gamma$ decays to the anomalous couplings is higher, but only $ZZ\gamma$ couplings can be measured in this channel because photons do not interact with neutrinos (the same reason why the decay diagrams for the reaction (2.9) vanish). The most recent preliminary results from LEP [6] based on the measurement [42] and the p_T^γ spectrum fit are as follows:

$$|h_{10,30}^Z| < 1.1, \; |h_{20,40}^Z| < 3.1,$$

at 95% CL for the same form factor scale $\Lambda = 500$ GeV. The limits on $h_{20,40}^Z$ violate unitarity. A comparison of these preliminary results with the DØ and CDF data is discussed in Chapter 6.

Overall, the indirect limits on the anomalous $ZV\gamma$ couplings are at present significantly worse than those obtained in direct measurements, such as study of the radiative Z-decays at LEP or high-energy production of the $Z\gamma$ system in $p\bar{p}$ collisions at the Tevatron (see Chapters 5 and 6).

2.5 Models of the Anomalous Couplings

Do not expect too much of the end of the world.

Stanislaw J. Lec, "Aforyzmy. Fraszki"

Up to this point we have described the phenomenology of anomalous $ZV\gamma$ couplings without discussing any of the theoretical models which predict such phenomena. It should be stressed that there is no way to introduce a contact triple-boson interaction in any reasonable theory of anomalous couplings because of the high dimension of the operators in the vertex functions (2.3), (2.4). Any attempt to build a pointlike coupling with operators of dimension six and higher will result in a non-renormalizable theory. Thus the "blob" in Fig. 2.1 for the trilinear vertex is essential — it "hides" the exact structure of the non-pointlike interaction.

One possible way to introduce such a triple-boson interaction is through the triangle loop diagrams shown in Fig. 2.9. As it was discussed in sec. 2.3.4, the contribution of the regular SM QED-type of corrections is extremely small. However, it is possible to explain much stronger anomalous couplings by considering new types of particles in the triangular loops.

The most developed theory which gives rise to the CP-conserving anomalous couplings is the Minimal Supersymmetric Standard Model (MSSM) [43]. In this theory each particle has a supersymmetric (SUSY) partner. The partners for the fermions are bosons and *vice versa*. The MSSM also predicts an additional charged Higgs doublet in the gauge sector of the SM.

Although the SUSY partners have not yet been discovered, and masses below a hundred GeV have been excluded for most of them by various experiments [9], heavy supersymmetric particles may still contribute significantly to the anomalous couplings via the triangular loop diagrams.

These corrections were calculated for $WW\gamma$, WWZ couplings in several theoretical papers (see [44] and the references therein). Actual calculations of the loop corrections for the $ZV\gamma$ vertices have not been carried out yet. It is reasonable to expect that most of the corrections result in the anomalous couplings $h_i^V = \mathcal{O}(10^{-2})$ [28, 35]. But for certain values of the SUSY symmetry breaking parameters the deviations from the Standard Model can be much larger, and the dimension six CP-conserving couplings can be of order of 1. However, the application of perturbation theory in this region of parameter space is questionable. See [44] for details.

Currently, the only plausible model which predicts CP-violating $ZV\gamma$ couplings due to loop corrections is an extension of MSSM with two Higgs doublets [45]. The formalism of these calculations is given in Ref. [46].

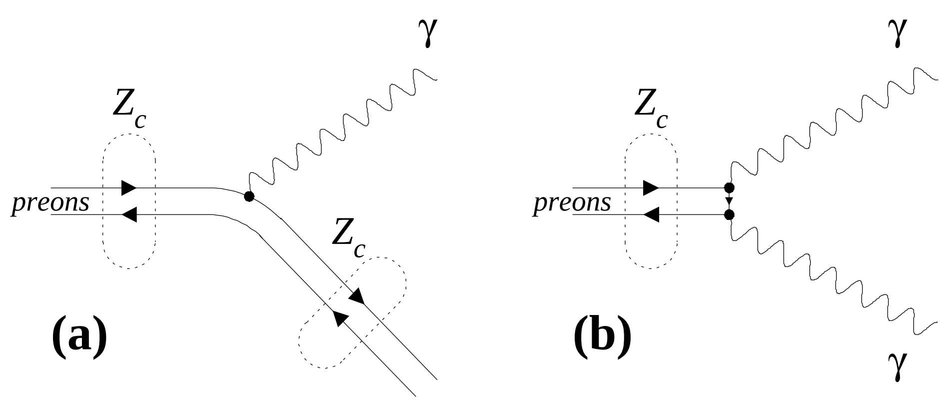

Figure 2.12: Trilinear gauge boson couplings in the models with a composite Z made of a preon-antipreon pair (Z_c): a) $ZZ\gamma$ vertex; b) $Z\gamma\gamma$ vertex.

Another theory of the anomalous $ZV\gamma$ couplings is one based on the assumption of a composite Z boson. In these models (e.g. [47]) the Z boson consists of a pair of hypothetical particles, a *preon* and an *antipreon*. The anomalous $ZV\gamma$ couplings in these theories naturally arise due to the diagrams in Fig. 2.12, analogous to the radiative meson decay diagrams [48]. The composite Z boson models predict anomalous couplings to be of the order of $h_i^V = 0.1 - 1$ [35].

The sensitivity of current experiments is not yet enough to rule out the MSSM or the models with a composite Z based on the limits on the anomalous couplings. This is a goal for future experiments (see Chapter 6).

Chapter 3

Detector and Monte Carlo

The bored tourists who pay their nine francs at the desk or are admitted free on Sundays may believe that elderly nineteenth-century gentlemen — beards yellowed by nicotine, collars rumpled and greasy, black cravats and frock coats smelling of snuff, fingers stained with acid, their minds acid with professional jealousy, farcical ghosts who called one another cher maître — placed these exhibits here out of a virtuous desire to educate and amuse the bourgeois and the radical taxpayers, and to celebrate the magnificent march of progress. But no...

U. Eco, "Foucault's Pendulum"

3.1 The Tevatron

The search for anomalous $ZV\gamma$ couplings requires high energies for the interacting particles. The Fermi National Accelerator Laboratory high luminosity proton-antiproton collider (Tevatron) with a center of mass energy of 1.8 TeV made it possible for the first time to study these couplings in hadronic collisions. This section contains a brief description of the accelerator and its main operating principles. More details on the Tevatron accelerator can be found in [49, 50].

3.1.1 Historical Sketch

The state-of-art Tevatron accelerator complex currently provides the highest energy proton and antiproton beams in the world, and most likely will remain the most powerful $p\bar{p}$ collider at least until the beginning of the next century. The existence of this machine became possible due to a number of important achievements in accelerator techniques, such as antiproton cooling and storage, developed at CERN [51], superconductor manufacturing and technology, detailed computer simulation of beam behavior, and many others. The Tevatron is truly the top of the line of the modern accelerators.

The machine was built in several steps. It started in 1970 with the installation of the 200 MeV high-current linear accelerator (Linac) [52]. From 1972 to 1982 the 8 GeV booster and the Main Ring [53] (typically running at 400 GeV energy) were built. The fixed target physics program at 400 GeV was conducted at Fermilab from the mid-70's through January 1984. During that time the superconducting Tevatron ring (then known as the Energy Doubler) [49] was installed in the Main Ring tunnel, and after a short shutdown the first 800 GeV fixed target run took place in July 1984, followed by the second similar run in 1985. The antiproton source [54] was commissioned in July 1985, and on October 12, 1985, the first Tevatron $p\bar{p}$ collisions were seen in the CDF detector. The first, low luminosity (~ 4 pb^{-1}), Tevatron run took place in 1988 – 1989 with only the CDF detector collecting physics data. During a three year shutdown another fixed target run was conducted, the accelerator system was improved, and the DØ detector was assembled and prepared for the first, high-luminosity (~ 20 pb^{-1}), run which took place from August 1992 through May 1993 (run Ia).

3.1.2 Tevatron Operation in Collider Mode

The Tevatron accelerator complex consists of several separate parts shown in Fig. 3.1. The Cockroft-Walton accelerator is used for initial acceleration of H^- ions obtained by ionizing hydrogen gas with electrons. This small accelerator uses a static electric field to accelerate ions to an energy of 750 keV. The ions are then transported to a 150 meter long Linac which accelerates them to $200 - 400$ MeV and shoots the beam through a carbon foil which strips off the electrons from the hydrogen ions leaving only protons in the beam. During the next stage, the protons are accelerated to 8 GeV in a small (500 meters in circumference) synchrotron ring (the Booster) and injected into the Main Ring (which is also a synchrotron), located in the tunnel with a circumference of 3.7 miles, or more than 6000 meters. The Main Ring consists of over 1000 conventional warm temperature copper-coiled magnets. The proton beam in the Main Ring is accelerated to ~ 120 GeV and formed into a set of short bunches with $\sim 2 \cdot 10^{12}$ protons per bunch. The bunches can be either transported into the superconducting Tevatron ring (in order to fill it with a proton store), or dumped on a nickel/copper target (located in the Target Hall), producing $\sim 2 \cdot 10^{7}$ antiprotons per proton bunch.

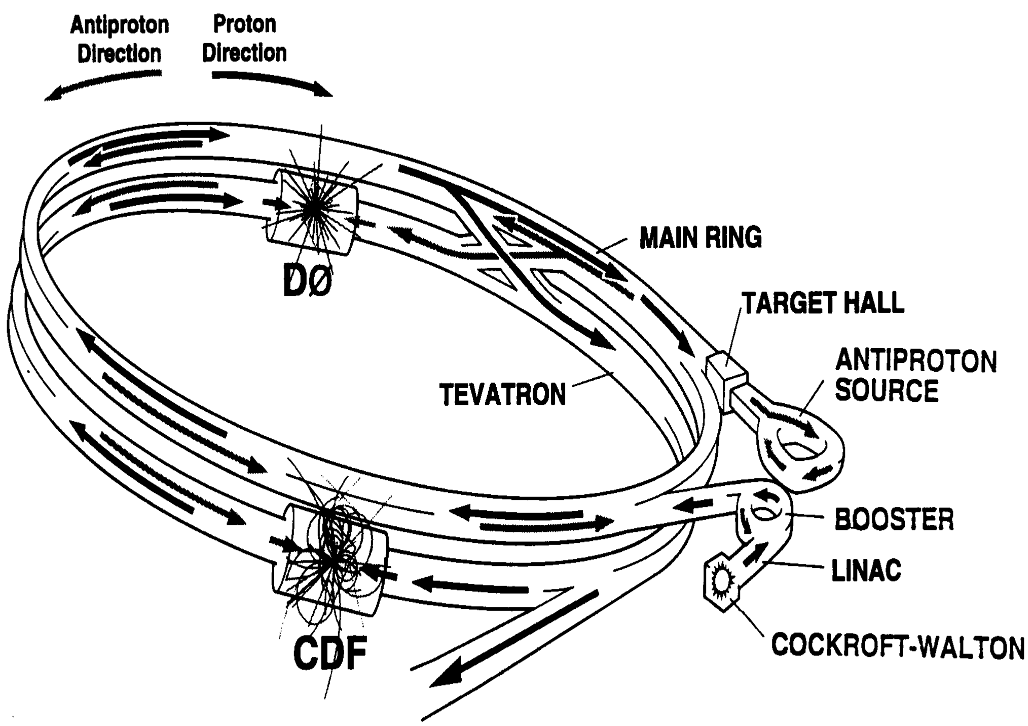

Figure 3.1: The Tevatron accelerator schematic layout.

The antiprotons created in these collisions have wide angular divergence and broad energy spectrum. They are initially focused with a lithium magnetic lens and injected into the first of two antiproton storage rings, the Debuncher. In this ring the antiproton energies are equalized, and the particles are formed into a compact beam (this process is known as *cooling*). Two processes are used to form such a mono-energetic antiproton beam: the debunching, and stochastic cooling. The former uses computer controlled radio-frequency pulses to smooth the antiproton store into a continuous ring where all particles have approximately the same momentum. The latter squeezes this ring in the transverse plane by using beam sensors which transmit information about the beam profile to kicker electrodes downstream. The electrodes introduce corrective magnetic fields which on average kick the antiprotons deviating from the beam center back into the beam. The cooling processes run continuously and prepare a monochromatic squeezed antiproton beam with $\sim 2 \cdot 10^6$ antiprotons for the second antiproton storage ring, or Accumulator. In the Accumulator the antiprotons are further cooled and their density is increased. When about $4 \cdot 10^{11}$ antiprotons are stored in the Accumulator (it typically takes 8 to 12 hours), they are transferred back into the Main Ring, accelerated, and injected into the Tevatron ring in the direction opposite to that of the proton beam.

The Tevatron ring uses superconducting magnets operating at liquid helium temperature (4 K) and producing a bending magnetic field of ~ 4 T which allows for higher energy protons and antiprotons. When the filling of the Tevatron ring with both p and $\bar{p}$ is completed, the particles are formed into six proton and six antiproton bunches with about 10^{11} and $5 \cdot 10^{10}$ particles respectively per bunch, and accelerated to the maximum energy (0.9 TeV currently). After reaching the final energy the beams contain considerable halos, which are scraped with a metal plate collimator, before the CDF and DØ detectors start to collect physics data. The beams are held apart in the accelerator except at the two beam crossing points BØ (CDF) and DØ. The typical lifetime of the Tevatron beams, determined by beam scattering on the residual gasses in the Tevatron vacuum pipe, is about 12 – 18 hours. During this time new antiprotons are stored into the Accumulator which allows for a continuous operation of the Tevatron. The downtime between two subsequent Tevatron stores is about 2 hours.

The maximum luminosity achieved in run Ia was $\sim 9 \cdot 10^{30}$ cm^{-2}s^{-1}.

3.1.3 The Tevatron Future

Currently, the Tevatron is in the middle of run Ib which started in 1994 and will continue till the end of 1995. The luminosity of the Tevatron was increased since run Ia and the highest luminosity achieved to date in the current run is $1.2 \cdot 10^{31}$ cm^{-2}s^{-1}. It is expected that the accelerator will deliver about 100 pb^{-1} of physics data per experiment by the end of run Ib, thus increasing the statistics collected in run Ia by a factor of ~ 5.

The near future of the Tevatron is based on the Main Injector upgrade [55]. The Main Injector which will act as a booster to the Tevatron, will be located in a separate tunnel about half of the size of the Main Ring. This intermediate ring will allow luminosity of $\sim 10^{32}$ cm^{-2}s^{-1} in run II which is expected to take place in 1998 with upgraded CDF and DØ detectors. The Main Injector will also make it possible to run the collider and the fixed target programs simultaneously.

The more distant future of Fermilab is not clear yet. There are several proposals for further upgrade of the accelerator complex. One is the Super-Luminous Tevatron, which will operate at $\sqrt{s} = 2$ TeV with the instantaneous luminosity of $> 10^{33}$ cm^{-2}s^{-1} [56]. Another possible scenario is a DiTeV machine with new superconducting magnets which will be able to handle 2 TeV beams [56]. However, it is clear that further upgrades will not take place before the 21st century.

3.2 The DØ Detector

This section contains a brief description of the multipurpose DØ detector and some more details on the different subdetectors used for the analysis described in this Dissertation. A more thorough description of the DØ detector can be found in Ref. [57].

3.2.1 Overview

The DØ detector is a general purpose 4π particle detector dedicated for extensive studies of the high-p_T physics in $p\bar{p}$ annihilations at the Fermilab Tevatron collider (see sec. 3.1 for brief accelerator description). It was designed with an emphasis on superior calorimetry and muon identification, with less attention payed to the identification of the charged particles within jets. For these purposes, the design efforts were focused on building a compact and hermetic calorimeter with excellent hadronic and electromagnetic energy resolution. The calorimeter based on the use of uranium as a passive material, and liquid argon as the readout medium, is the heart of the DØ detector. In the tradition of the UA2 detector, DØ does not have a central magnetic field, thus

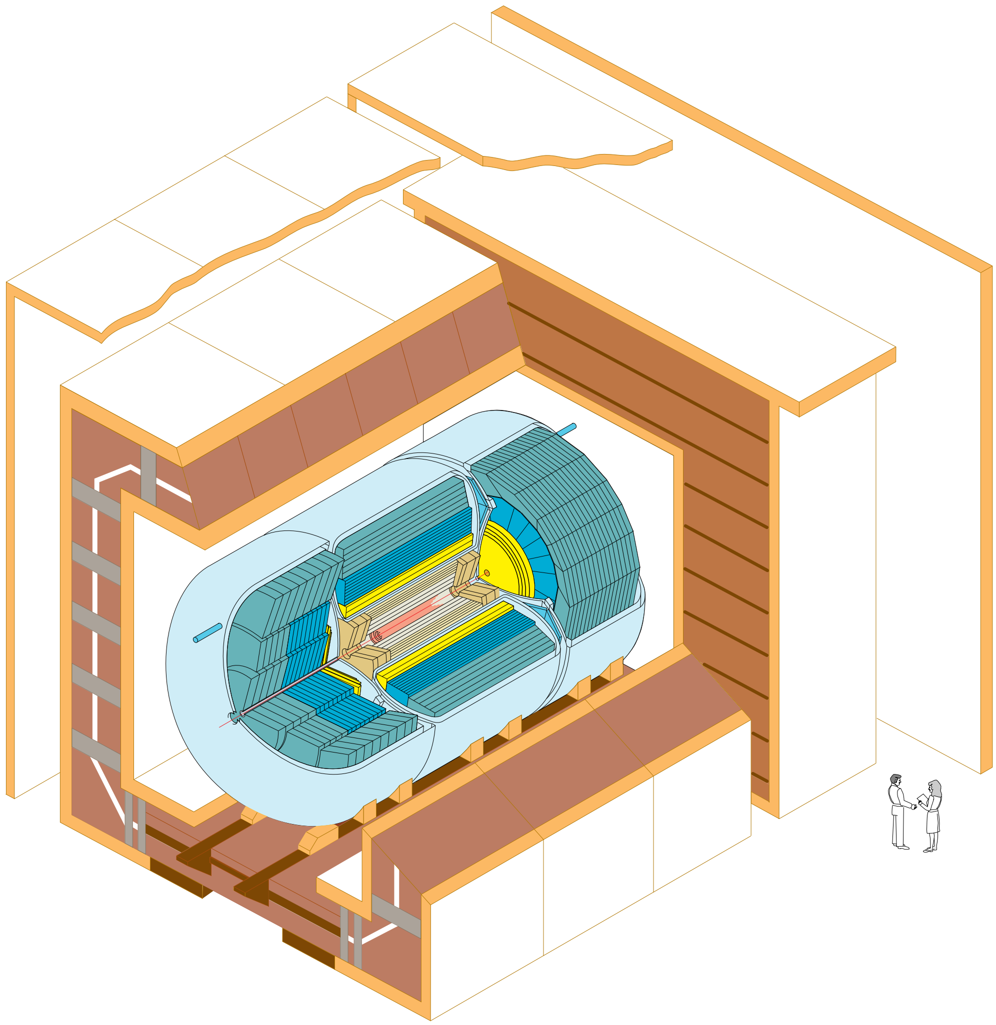

Figure 3.2: The DØ detector.

making the calorimeter extremely compact, and allowing for a full coverage muon system.

This philosophy made it possible to build DØ as a second generation detector complementary to the conventional warm-calorimetry CDF detector [58], operating at the same accelerator. Even without superior tracking, as CDF has, the DØ detector is capable of studying a wide variety of high energy phe-

Figure 3.3: The DØ Collaboration.

nomena, such as high precision electroweak physics, top-quark search, heavy quark physics, perturbative QCD, and new physics.

An isometric view of the DØ detector is shown in Fig. 3.2. Besides the liquid argon calorimeter, it consists of the other two main parts: the central tracking (located inside the calorimeter) and the three-layer muon tracking system with an iron toroidal magnet (surrounding the calorimeter).

The DØ detector is approximately 13 m high $\times$ 11 m wide $\times$ 17 m long with a total weight of about 5500 tons. The large dimensions and the weight are primarily due to the muon system. The detector was built and put into operation at a cost of thousands of man-years of labor (accomplished by engineers, technicians, and physicists) and 75 million dollars. As of today, the DØ Collaboration unites about 450 people of 44 scientific organizations located in 10 countries around the world (major participants are shown in Fig. 3.3).

The DØ Collaboration was organized in 1983 with Paul Grannis as its first spokesman. The full DØ proposal [59] was presented to the Physics Advisory Committee (PAC) of Fermilab in November, 1983. Detailed design and assembling of the detector took place in 1985 – 1992. The cosmic ray commissioning run was held in February – May, 1991. On February 14, 1992 the DØ detector was rolled into the collision hall, and on May 12, 1992 the first $p\bar{p}$ events were recorded on tape. At present, the detector is in the middle of its second physics run (run Ib). The spokesman duties are currently shared between Paul Grannis and Hugh Montgomery.

The DØ detector was built according to general principles of particle detection at high-energy hadron colliders (see, e.g. [60]). The tracking chambers are located as close as possible to the interaction point, prior to the massive calorimeter and muon system. The tracking detector is surrounded by the electromagnetic calorimeter layers, followed by a thick hadron calorimeter. The only particles which escape the calorimeter are muons (measured in the muon system) and neutrinos or other possible weakly interacting long-lived particles (detected by the energy imbalance in the detector). The calorimeter covers the pseudorapidity range $|\eta| < 4.5$ (see below for a definition of the pseudorapidity η), making the DØ detector almost hermetic. The only way energy can escape the detector is in the very forward region, through the beam-pipe traversing the center of the detector.

The azimuthal symmetry of the detector is violated by the Main Ring of the accelerator passing through the outer coarse hadronic layer of the calorimeter (see sec. 3.3) at a height of $89.2''$ above the Tevatron ring (see sec. 3.1), the rectangular design of the muon system chambers, and the absence of one layer of the muon detectors in the area right underneath the calorimeter, occupied by mechanical support structures.

The DØ detector uses a reference frame defined by the Central Drift Chamber (CDC, see sec. 3.4.3). It has a right-handed coordinate system with z-axis along the direction of the proton beam and with a vertical y-axis. The polar coordinate system, used for definition of many physics parameters, has azimuthal angle (ϕ) defined so that $\phi = \pi/2$ points along y direction, and polar angle (θ) measured relative to the z-axis ($\theta = 0$ corresponds to the z-axis direction). For ultrarelativistic particles it is more convenient to use an approximate Lorentz invariant, pseudorapidity (η), instead of the polar angle. The pseudorapidity is defined as

$$\eta \equiv -\log\left[\tan\frac{\theta}{2}\right] = \tanh^{-1}(\cos\theta). \tag{3.1}$$

The positions of the other subdetectors relative to the CDC were surveyed by precise geodesic measurements and finely adjusted by matching tracks reconstructed in different tracking subdetectors and shower centers in the calorimeter [61].

The following sections discuss the details of different subsystems of the DØ detector.

3.3 Calorimeter

Being the centerpiece of the DØ detector, the liquid argon calorimeter is used not only for energy measurements, but as a source of additional information necessary for identification of muons, electrons, photons, and jets, as well as for missing transverse energy ($\not\!\!E_T$) measurements. Moreover, since the DØ detector does not have a central magnetic field, the calorimeter is the only source for determining the energy scale precisely.

3.3.1 Calorimeter Concept

Most modern high energy physics calorimeters use the *sampling* principle for energy measurements. A sampling calorimeter consists of a multilayer "sandwich" made of slices of a dense material with high atomic number (in which electromagnetic and hadron shower are developed), interleaved with slices of an active media (usually a scintillator or an ionization medium) which measure fractional energy depositions, or *sampling fractions*. These fractions, in general, are proportional to the incident particle energy.

The primary particle can interact with the calorimeter material via electromagnetic or strong interactions. The products of the interactions are known as electromagnetic or hadronic showers. The features of these two types of showers are quite different, and the calorimeter is typically subdivided into two parts — the inner one for the electromagnetic shower detection, and the outer one for the hadronic shower measurements. Since the nuclear interaction length (λ) in most heavy materials is much larger than the radiation length

(X_0), even a thick ($\gg X_0$) electromagnetic part typically contains only a fraction of λ, and therefore the electromagnetic calorimeter is rather transparent to hadrons. On the other hand, the thickness of the electromagnetic calorimeter ($\approx 20\ X_0$ in the DØ case) in most of the cases is sufficient to absorb the electromagnetic shower energy, so the hadronic and electromagnetic calorimeters work relatively independent of each other for the single-particle showers.

There are many important rules which must be satisfied for optimizing the calorimeter characteristics, such as energy resolution. For instance, the best hadronic energy resolution can be achieved with the so-called compensating calorimeters [62], which have equal response to the electromagnetic and hadronic showers of the same energy. The reason for this is large fluctuations of the electromagnetic component (due to the π^0's, η's production with further radiative decays) in hadronic showers. If the calorimeter has different response for electrons and pions, these fluctuations translate into the statistical uncertainty in the energy deposited in the readout medium, and, therefore, into the resolution. For most of the sampling calorimeters electron response is higher than hadronic [63].

To equalize the electromagnetic and hadronic responses, the DØ calorimeter uses depleted uranium as a passive material (absorber) for the electromagnetic and inner hadronic layers. The idea to use uranium-238 in the hadronic calorimeters is rather old [64]. The original motivation was that due to the nuclear break-ups and neutron-induced fission in a radioactive uranium, part of the normally invisible energy converts into a detectable one, which increases the hadronic response. However, it turned out that in reality the compensation is mostly due to a decrease of electron response in a high-Z absorber material [63]. In addition to accounting for the nearly identical hadronic and electromagnetic response, the uranium, being very dense, makes the calorimeter extremely compact. Stainless steel and copper are used as absorbers in the outer hadronic layers. Liquid argon was chosen as an active (ionization) medium for all DØ calorimeters. This choice gives a unit gain and radiation hardness of the calorimeter at the cost of low operating temperature (86K) which requires a cryostat and a cryogenic system.

A detailed description of the calorimeter design principles and applications of liquid argon and other calorimeters in high energy physics can be found in Refs. [51, 62, 63, 65].

3.3.2 Readout Design

DØ calorimeters use absorber plates of different thickness ($3 - 46.3$ mm) made of different materials. However, usage of uniform readout structures made it easy to use the same cell design for all calorimeters. A schematic view of the unit cell is shown in Fig. 3.4. The gap between adjacent absorber plates is filled with liquid argon. The electron-ion pairs (created in the liquid argon by charged particles from electromagnetic or hadronic showers) are collected by the electrodes in presence of a strong electric field. Metal absorbers are used as ground electrodes (cathodes), and the readout boards at $+2.0$ to 2.5 kV, located in the center of the gaps, serve as anodes. Each board in most of the modules is a sandwich of copper readout pads between two 0.5 mm plates of

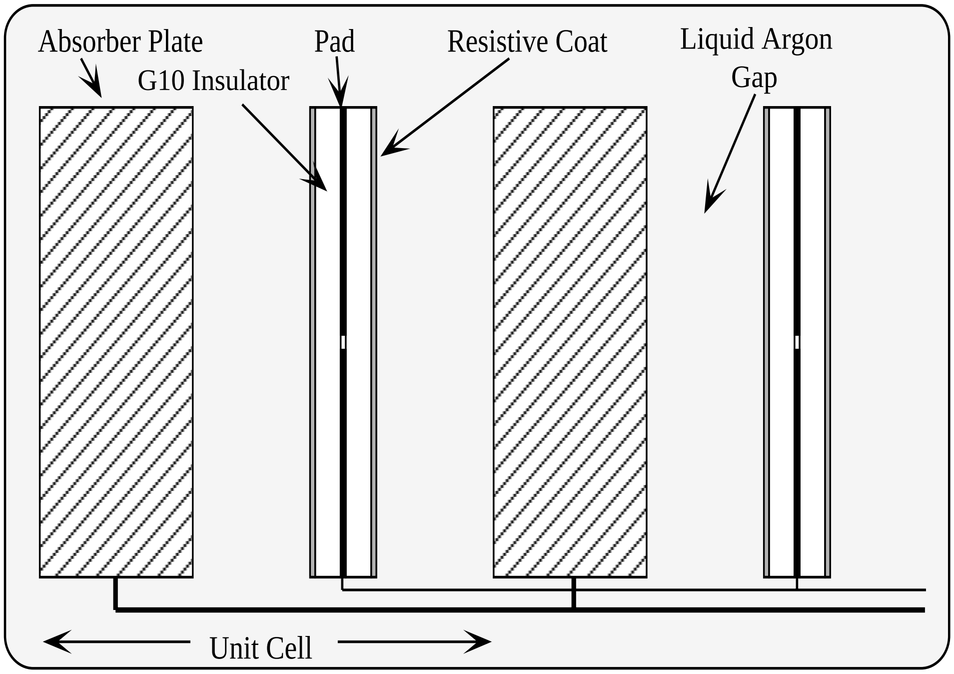

Figure 3.4: Schematic view of the liquid argon calorimeter unit cell.

G10 plastic covered with a resistive epoxy coating. High voltage is applied to the entire resistive coat, and the charge collection in this coat induces a charge on the copper readout pads via capacitative coupling. The electromagnetic and small-angle hadronic modules in the end calorimeter (see sec. 3.3.5) have multilayer printed circuit readout boards. The gap between absorber plate and readout pad in most of the cases is 2.3 mm, which corresponds to a typical electric field of 9 kV/cm and an average electron drift time of 450 ns. The gap thickness was chosen to be large enough to observe minimum ionizing particle signals in the calorimeters, which is an important requirement for muon identification (see sec. 4.1.3).

There is no charge multiplication in the liquid argon, so the signals from the readout pads can be small. To detect them, several pads are ganged together in depth to form a readout cell (see sec. 3.3.3). Charge-sensitive preamplifiers mounted on the calorimeter cryostat integrate the ganged signals and pass them to the base-line subtraction modules located on the detector platform. They split the signal into two paths — the one used by the fast Level 1 trigger (see sec. 3.6.2), and the main data path where signals are properly shaped, digitized in 12-bit analog-to-digital converters (ADC's) and fed into the data acquisition system (see sec. 3.6.3). Fast Level 1 trigger electronics combine the readout cells into $\Delta\eta \times \Delta\phi = 0.2 \times 0.2$ trigger towers and provide information about the energy deposition in each of the towers (within 2.2 μs from the beam-crossing time).

3.3.3 Calorimeter Geometry

The DØ calorimeter consists of the Central Calorimeter (CC) and two mirror-image End Calorimeters (EC) described in details in separate sections. Each calorimeter is located in its own cryostat and has a modular structure with the modules of three distinct classes: electromagnetic (EM), fine hadronic (FH), and coarse hadronic (CH). Such a design is determined by the differences in the longitudinal development of the electromagnetic and hadronic showers. An isometric view of the DØ calorimeter is shown in Fig. 3.5.

The transverse sizes of the readout cells in different modules are chosen to be of the same order as the diameters of the corresponding showers (≈ 2 cm for electromagnetic and ≈ 10 cm for hadronic). Physical cells are ganged together

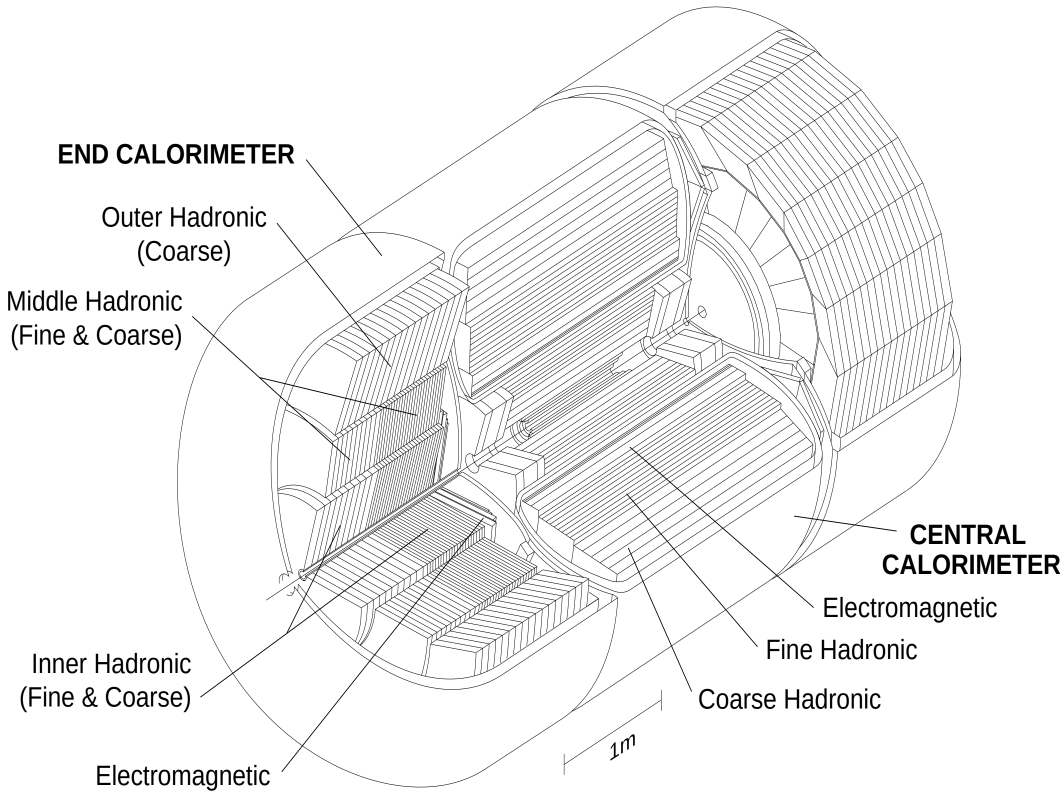

Figure 3.5: DØ liquid argon calorimeter.

in depth to form a readout cell using a pseudo-projective geometry, as shown in Fig. 3.6. The term *pseudo-projective* refers to the fact that the centers of the cells of increasing shower depth point to the interaction vertex, whereas the cell boundaries are perpendicular to the absorber plates [57]. Typically, the transverse segmentation of the readout towers is $\Delta\eta \times \Delta\phi = 0.1 \times 0.1$.

An important feature of the DØ calorimeter is the fine longitudinal segmentation which is essential for distinguishing between π^0's and electrons (see sec. 4.1.1), as well as for the jet reconstruction. The EM modules consist of four separate layers, EM1 to EM4. Each layer uses 3 mm or 4 mm thick de-

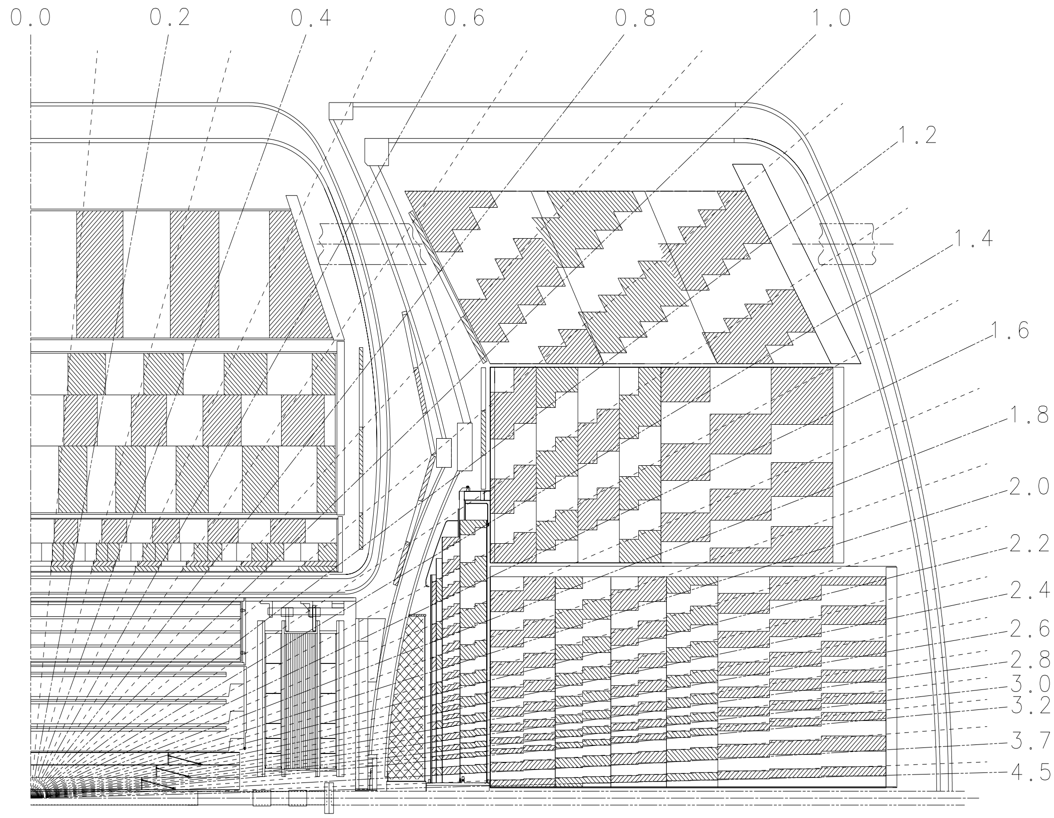

Figure 3.6: Pseudo-projective geometry of the readout calorimeter cells.

pleted uranium plates as an absorber. The FH modules consist of three or four layers with 6 mm depleted uranium (doped with 1.7% niobium) plates as an absorber. The outer CH module has only one layer with thick (46.5 mm) stainless steel or copper absorber. The longitudinal arrangement of the calorimeter towers as a function of η is shown in Fig. 3.7. The fine hadronic layers measure the energy and position of penetrating hadrons, such as charged pions. The coarse hadronic layer protects against punchthrough and leakage of hadronic showers due to large fluctuations in the longitudinal shower development. The total thickness of the calorimeter is $7-10\ \lambda$.

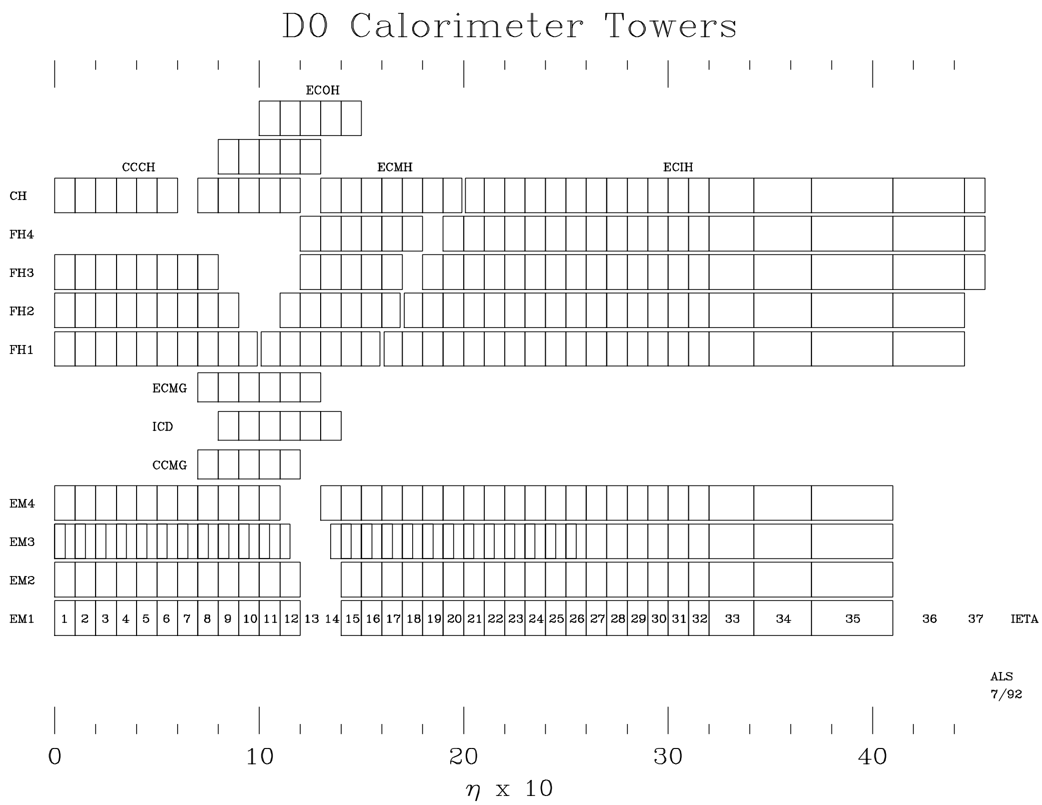

Figure 3.7: Longitudinal arrangement of the readout calorimeter cells.

3.3.4 Central Calorimeter

The Central Calorimeter (CC) [57] (see Fig. 3.5) consists of the inner ring of 32 CCEM modules and two hadronic calorimeter rings with 16 CCFH and 16 CCCH modules, respectively. The module boundaries in the three rings are shifted one relative to the other, so that no projective ray encounters more than one intermodule gap. The CC has a length of 2.6 m, and covers the pseudorapidity interval $|\eta| < 1.2$. The total weight of the CC modules and the support structure is 305 tons, with an additional 26 tons contributed by liquid argon [57].

Module type	CCEM	CCFH	CCCH
Pseudorapidity coverage	± 1.2	± 1.0	± 0.6
Number of modules	32	16	16
Absorber	U	UNb	Cu
Absorber thickness (mm)	3	6	46.5
Argon gap (mm)	2.3	2.3	2.3
Readout cells per module	21	50	9
Longitudinal depth ($\eta = 0$)	$20.5\ X_0 = 0.76\ \lambda$	$3.2\ \lambda$	$3.2\ \lambda$
Number of readout layers	4	3	1
Cells per readout layer	2/2/7/10	20/16/14	9
Depth per readout layer	$2.0/2.0/6.8/9.8\ X_0$	$1.3/1.0/0.9\lambda$	3.2λ
Sampling fraction (%)	11.79	6.79	1.45
Segmentation ($\Delta\phi \times \Delta\eta$)	EM1,2,4: 0.1×0.1 EM3: 0.05×0.05	0.1×0.1	0.1×0.1
Total number of channels	10,368	3,000	1,224

Table 3.1: Central Calorimeter vital statistics.

The first two EM layers with a thickness of $\approx 2\ X_0$ each and a transverse segmentation of 0.1×0.1 are used to measure the longitudinal profile of an electromagnetic shower near its origin. This profile differs statistically for the showers induced by electron/photon and π^0 decaying into a pair of spatially close photons. The third layer, located at the shower maximum has finer transverse segmentation of 0.05×0.05 in (η, ϕ), which allows for more accurate measurement of shower centroid positions. The fourth layer completes the total EM coverage of $\approx 21\ X_0$ or $\sim 0.8\ \lambda$.

Major characteristics of the CC are given in Table 3.1 [57, 66, 67].

3.3.5 End Calorimeters

Each of the two mirror-image End Calorimeters (EC) [57, 68] (see Fig. 3.5) also has a modular structure. It consists of an electromagnetic module (ECEM), an inner fine hadronic module (IFH), an inner coarse hadronic module (ICH), and two concentric rings of middle fine hadronic/middle coarse hadronic (MCF/MCH), and outer coarse hadronic (OCH) modules (16 modules in each ring). The ECEM and FH calorimeters have an uranium absorber[1]; stainless steel (SS) is used in the coarse calorimeters.

The EC primarily covers the pseudorapidity interval $1.1 < |\eta| < 4.5$. For pseudorapidities of $1.1 < |\eta| < 1.5$ particles traverse little or no EM layers, but do encounter the OCH or MFH modules (see Fig. 3.6). The reconstruction of the electromagnetic energy in this region is unreliable (see sec. 3.3.6). In the region $1.5 < |\eta| < 2.0$, particles pass through the ECEM, IFH, MFH, and MCH modules. In the very forward region, $2.0 < |\eta| < 4.5$, particles pass only through ECEM, IFH, and ICH modules. The OCH modules of the EC extend the rapidity coverage down to $|\eta|$ values of 0.8, which is the transition region between the CC and EC (see discussion in sec. 3.3.6).

The segmentation of the most of the EC readout cells is 0.1×0.1 in (η, ϕ), except for the segmentation of the EM3 layer of ECEM which is twice as fine (as in the CCEM case), and increasing transverse cell size in the very forward region ($|\eta| > 3.2$) which reaches the maximum of 0.4×0.4 in (η, ϕ) for cells in

[1]Some of the ECEM cells use the stainless steel absorber plates to achieve more uniform sampling fraction [68].

Module type	ECEM	IFH	ICH	MFH	MCH	OCH
$\|\eta\|_{min}$	1.3	1.6	2.0	1.0	1.3	0.7
$\|\eta\|_{max}$	4.1	4.5	4.5	1.7	1.9	1.4
N of modules	1	1	1	16	16	16
Absorber	U/SS	UNb	SS	UNb	SS	SS
Abs. thick. (mm)	4	6	46.5	6	46.5	46.5
Argon gap (mm)	2.3	2.1	2.1	2.2	2.2	2.2
Cells/module	18	64	14	60	12	24
Longitudinal depth	20.1 X_0 0.95λ	4.4λ	4.1λ	3.6λ	4.4λ	4.4λ
N of readout layers	4	4	1	4	1	3
Cells/readout layer	2/2/6/8	16	14	15	12	8
Sampling (%)	≈ 8	5.7	1.5	6.7	1.6	1.6
$\Delta\phi$ segmentation	0.1/0.05	0.1–0.4	0.1–0.4	0.1	0.1	0.1
$\Delta\eta$ segmentation	0.1/0.05	0.1–0.4	0.1–0.4	0.1	0.1	0.1
N of channels	7,488	4,288	928	1,472	384 + 64 + 896	

Table 3.2: End Calorimeter vital statistics.

the ECEM, IFH, and ICH at $|\eta| \approx 3.7$ (see Fig. 3.7). The EM1 layer of the ECEM is only 0.3 X_0 thick, since the cryostat wall brings the total absorber thickness of the first section up to ≈ 2.0 X_0.

The overall weight of the EC calorimeter is 238 tons. Many other parameters of the End Calorimeter are listed in Table 3.2 [57, 66, 67, 68].

3.3.6 ICD and Massless Gap Detector

The pseudorapidity interval $0.8 < |\eta| < 1.5$ is a transition region between the Central and End Calorimeters (see Fig. 3.6). It contains a large amount of uninstrumented material, like cryostat walls, module endplates, etc. The amount of energy deposited in this material is not detected. For instance, the electromagnetic energy is not reconstructed correctly in the pseudorapidity range $1.1 < |\eta| < 1.5$. To correct for the energy loss in the transition region, DØ implemented two separate devices, the InterCryostat Detector (ICD) [57], and the Massless Gaps (MG) [57].

The ICD is an array of the scintillating modules mounted on the surface of the EC cryostat between the CC and EC (see Fig. 3.6). The ICD of each EC consists of 384 scintillator tiles of size 0.1×0.1 in (η, ϕ), which match the pseudo-projective towers in the calorimeter. The ICD readout is based on the phototubes [57].

In addition to the ICD, there are three rings of the MG detectors mounted inside the cryostats on the surfaces of the CCFH, MFH, and OCH modules. The MG detector consists of two readout boards surrounded by three liquid argon gaps. There are no absorber plates in the MG. The size of the MG cells is 0.1×0.1 in (η, ϕ) [57]. There are 320 readout channels in the CCFH ring and total of 192 channels in the MFH and OCH rings.

Together, the ICD and MG provide a reasonable approximation to the standard DØ sampling of the electromagnetic showers.

3.3.7 Calibration and Energy Resolution

As was mentioned above, the calorimeter is the only source of a precise energy scale in the DØ detector. Therefore, a precise calorimeter calibration is very important. Approximate calibration constants were obtained using the electron and pion test beams [71, 72]. They were further adjusted *in situ* for the electromagnetic calorimeter by comparing the positions of the peaks in the measured dielectron mass spectrum with the world average values of Z, J/Ψ, and π^0 masses [73, 74]. It was shown [73, 74] that the nonlinearity of the energy scale in the calorimeter is $< 0.5\%$.

The energy resolution of a sampling calorimeter is determined by the fluctuation of the number of ion pairs produced by a shower in sampling media. Several sources contribute to these fluctuations (see [51, 62]): sampling fluctuations, or fluctuations in the actual energy deposited in active media, leakage of energy out of the calorimeter, fluctuations in the calorimeter response due to changing operating conditions (such as the temperature and purity of the liquid argon, high voltage, etc.), and noise in the active layers (due to natural radioactivity of the uranium, readout electronics thermal noise, etc.).

The resolution of the sampling calorimeter can be parameterized in the following form:

$$\left(\frac{\sigma_E}{E}\right)^2 = C^2 + \frac{S^2}{E} + \frac{N^2}{E^2}, \tag{3.2}$$

where constants C, S, and N represent calibration errors, sampling fluctuations, and noise contributions, respectively. The noise term is usually negligible, except for very low energies [51].

The resolution for the DØ calorimeter was measured in the test beam for electrons and pions [57]:

$$\left(\frac{\sigma(E_{EM})}{E_{EM}}\right)^2 = (0.003 \pm 0.002)^2 + \frac{(0.157 \pm 0.005)^2}{E_{EM}\ [\mathrm{GeV}]}, \tag{3.3}$$

$$\left(\frac{\sigma(E_h)}{E_h}\right)^2 = (0.032 \pm 0.004)^2 + \frac{(0.41 \pm 0.04)^2}{E_h\ [\mathrm{GeV}]}. \tag{3.4}$$

The noise term is indeed small (typical noise is $\sim$ 100 MeV per readout tower).

Complete compensation in EM and FH layers has not been achieved. The ratio of the e and π responses in these layers varies from 1.11 at 10 GeV to 1.04 at 150 GeV [50].

The hadronic energy resolution of the calorimeter determines the calorimeter missing transverse energy ($\not{E}_T^{cal}$) resolution (i.e. the resolution in the $\not{E}_T$ calculated based on the calorimeter information only). It was measured using dijet data as a function of scalar sum of the E_T of the event, S_T [69, 70]:

$$\begin{aligned}\sigma(\not{E}_T^{cal}) &= (1.89 \pm 0.05)\ \mathrm{GeV} + (6.7 \pm 0.7) \cdot 10^{-3} S_T + \\ &\quad (9.9 \pm 2.1) \cdot 10^{-6} S_T^2/\mathrm{GeV}. \end{aligned} \tag{3.5}$$

3.4 Central Tracking

Tracking is a special issue, since the DØ detector does not have a central magnetic field. On one hand this simplifies track-finding algorithms and the detector design. However, on the other hand, the absence of a magnetic field does not allow for the reconstruction of particle momenta which, together with the calorimeter information, could aid a lot to particle identification.

Central tracking is very important in DØ, since it is the only way to distinguish between electrons and photons. Furthermore, track information, like

dE/dx, multiplicity of the tracks, etc., is essential for distinguishing between converted photons/pions and electrons. Central tracking is also used for identification of other types of particles (e.g. muons). Additionally, central tracks are used for reconstruction of the z-position of the primary interaction point and possible secondary vertices.

The tracking in DØ is done in the Central Detector (CD) which consists of four independent subdetectors (see Fig. 3.8). Closest to the beam, there is a Vertex chamber (VTX), followed by the Transition Radiation Detector (TRD), and Central Drift Chamber (CDC). Tracking in the forward region is done in two Forward Drift Chambers (FDC's). The whole CD is contained in the cylindrical space (r = 78 cm, z = $\pm$135 cm) bounded by the calorimeter cryostats (see sec. 3.3).

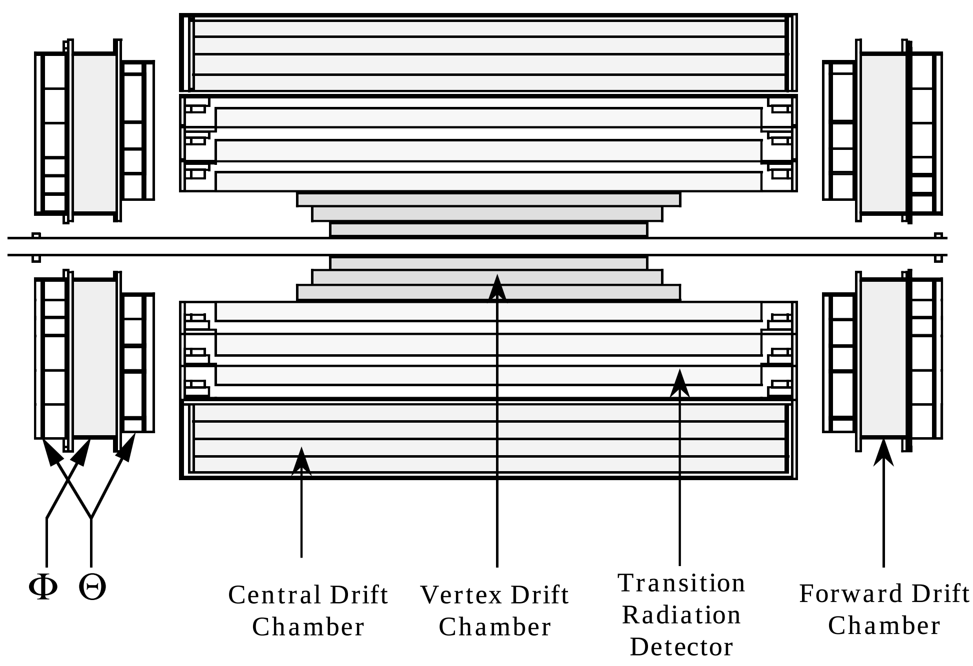

Figure 3.8: Central Detector layout.

All tracking detectors except the TRD are regular wire drift chambers (see Ref. [75] for details of the drift chamber operation). Both VTX and CDC have wires parallel to the beam for precise track measurement in the $r-\phi$ plane. The z coordinate is measured by a charge division method in the VTX and with the delay lines in the CDC. Each FDC has three sets of wire chambers: the middle one has radial wires and used for measuring ϕ information on the track; the two outer chambers have approximately axial wire planes. The outer chambers are rotated one relative to the other by $\pi/4$ (see sec. 3.4.4). The TRD also uses drift chambers for the detection of the X-rays of the transition radiation (see sec. 3.4.2).

The CD was designed to match the collider bunch-crossing interval of 3.5 μs, which allows for relatively long drift cells. The design was optimized to obtain a good spatial and two-track resolutions. Fast 8-bit flash analog-to-digital converters (FADC) [76] with ≈ 10 ns sampling time are used in the CD readout system for this purpose. With the typical drift velocity of $10-35$ μm/ns this corresponds to an effective detector granularity of $100-300$ μm with relatively small ($\approx 6,000$) total number of readout channels [57]. Before digitizing, the signals are amplified in Fujitsu MB43458 quad common base preamplifiers [77] mounted on the chamber surfaces, and further shaped by the shapers located in the DØ detector platform. The tracking electronics flow chart is shown in Fig. 3.9. The electronics is discussed in more detail in [57].

The following sections describe details of the CD subdetectors. Despite the fact that only the CDC and FDC information was primarily used in the

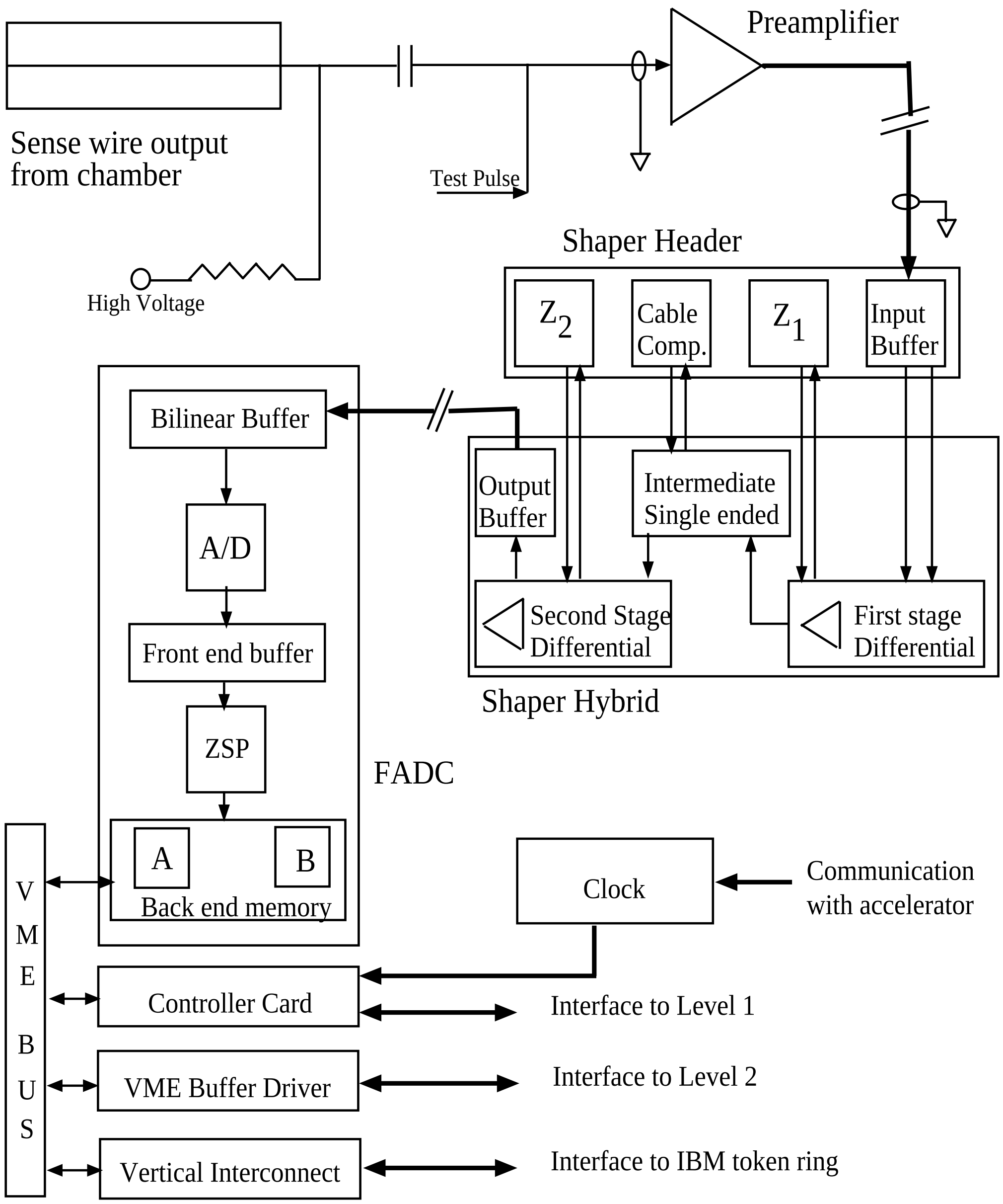

Figure 3.9: Schematics of the Central Detector electronics.

actual physics analysis described in this Dissertation, the details of the VTX and TRD chambers are also relevant to the extensions of this work, since we plan to utilize the information provided by these detectors for selecting $Z\gamma \rightarrow \nu\bar{\nu}\gamma$ events which are contaminated by a large $W \rightarrow e\bar{\nu}$ background (see sec. 4.4).

3.4.1 Vertex Chamber

The Vertex Chamber (VTX) [78] is the innermost tracking detector in DØ (see Fig. 3.8). Its inner radius (3.7 cm) is determined by the size of the beryllium beam pipe, and the outer active radius is 16.2 cm. It fully covers the pseudorapidity range of $|\eta| < 2.0$.

An original design goal of the VTX was to resolve secondary vertices from heavy quark decays and to complement the other tracking detectors in track parameter measurements. The VTX was designed to have the spatial resolution of $\sim$ 50 μm in $r - \phi$ plane. This requires an extremely precise placement of the sense wires ($\approx$ 25 μm, which is comparable with the diameter of the wire itself) and a drift time measurements with an accuracy of a few nanoseconds [60].

The chamber consists of three concentric layers of drift cells separated by a support structure of four carbon fiber tubes (see Fig. 3.10). The inner ring contains 16 drift cells; each outer ring has 32 cells. The $r - \phi$ coordinate in a cell is measured by 8 axial sense wires made of 25 μm NiCoTin alloy (38.3% Co, 19.3% Cr, 15.6% Ni, 13.3% Fe, and 11.4% Mo). Adjacent wires

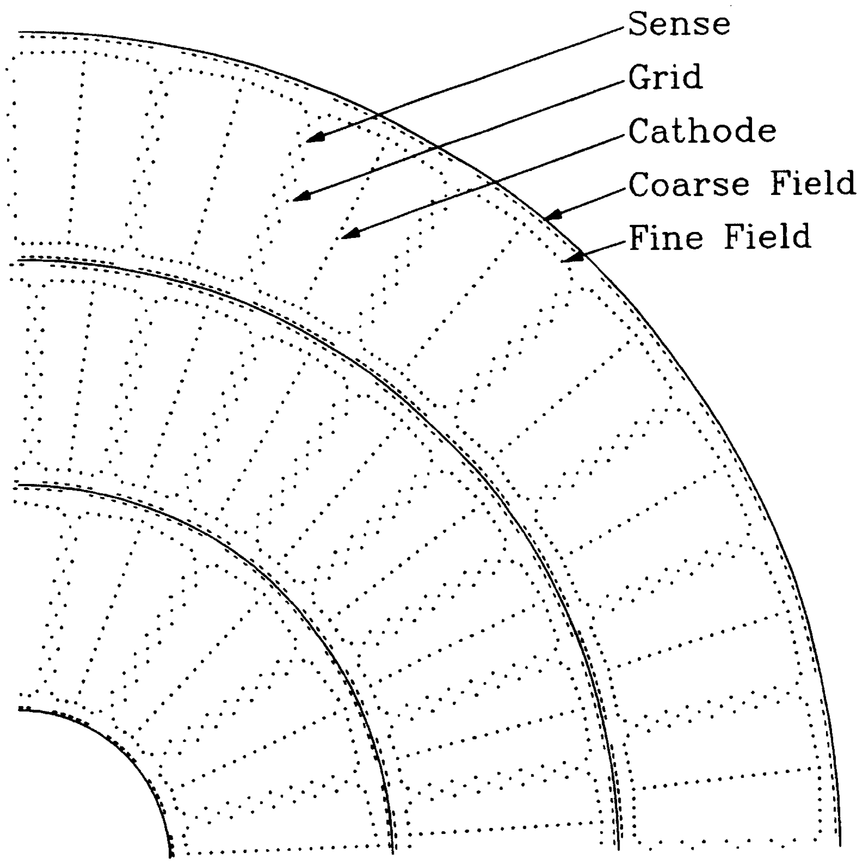

Figure 3.10: End view of a Vertex Chamber quadrant.

are staggered by $\pm 100\ \mu$m to resolve left-right ambiguities; the three layers are also shifted in ϕ relative to each other to further improve track reconstruction. Field and grid wires are made of 152 μm gold-plated aluminium. Coarse field shaping is provided by aluminium strips mounted on the support tubes. The wires are mounted on thin G10 plastic bulkheads with the tension supported by titanium rods (see Fig. 3.11) [57].

The z-coordinate in the VTX is reconstructed via the charge-division technique which is based on the difference in the signal amplitudes on both sides of the resistive sense wire [57].

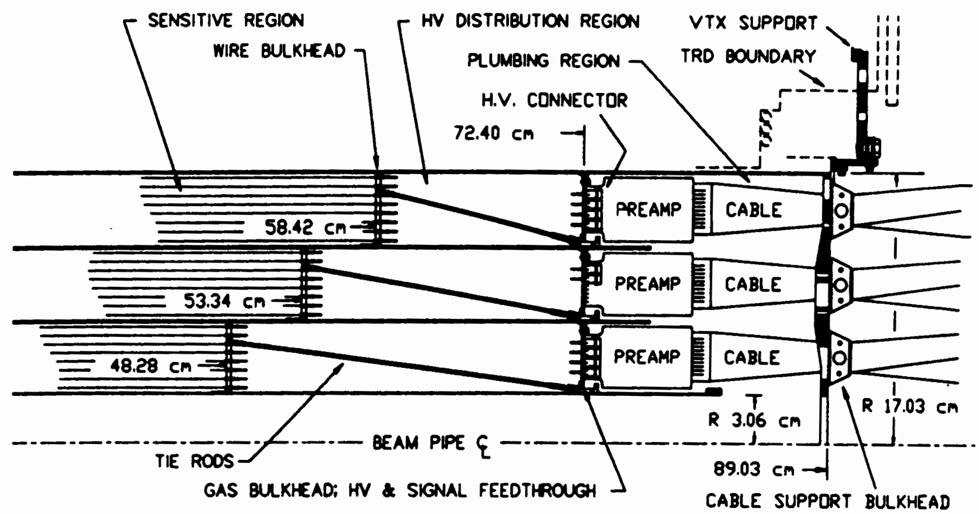

Figure 3.11: Endplate of the Vertex Chamber with wire and cable supporting structures.

The VTX uses a 95% CO_2/5% C_2H_6 gas mix with a small admixture of H_2O at the atmospheric pressure. This mix yields a relatively low drift velocity ($\approx$ 7 μm/ns), as required for high spatial resolution. The VTX resolution is typically 60 μm in $r - \phi$ and 1.5 cm in z directions [80].

For the real high-luminosity physical environment the track reconstruction in the VTX chamber has not been tuned well enough yet. Therefore, the VTX information is used for particle identification in the current analysis only for the cases when a reconstructed VTX track well matches a track in the CDC or FDC (which occurs only for $\approx$ 10% of CDC/FDC tracks). We, however, started to use the VTX hit information for improving the electron/photon separation for the $Z\gamma \to \nu\bar{\nu}\gamma$ event selection (see sec. 4.4).

The major parameters of the VTX chamber are listed in Table 3.3 [50, 57].

Parameter	Specification
Number of layers	3 (Layer0/Layer1/Layer2)
Radius [79] (R_{in}/R_{out})	Chamber: 3.7/16.2 cm Layer0: 3.73/6.9 cm Layer1: 8.40/11.60 cm Layer2: 13.00/16.23 cm
$\|\eta\|$-coverage [79] ($\|\eta_{in}\|/\|\eta_{out}\|$)	Chamber: 3.25/2.00 Layer0: 3.25/2.64 Layer1: 2.55/2.23 Layer2: 2.21/2.00
Length of active volume/layer	96.6/106.6/116.8 cm
Number of sense wires/cell	8
Number of sense wires	640
Radial wire interval	4.57 mm
Gas type	95% CO_2 + 5% ethane +0.5%H_2O
Gas pressure	1 atm
Sense wire potential	+2.5 kV
Nominal drift field	1.0 kV/cm
Average drift velocity	7.3 μm/ns
Gas gain	$4 \cdot 10^4$
Sense wire specifications	25 μm NiCoTin, 80 g tension
Field wire specifications	152 μm Au plated Al, 360 g tension
Spatial resolution	$r-\phi$: 60 μm; z: 1.5 cm

Table 3.3: Vertex Chamber specifications.

3.4.2 Transition Radiation Detector

The Transition Radiation Detector (TRD) [83] is located just outside the VTX (see Fig. 3.8). It is used exclusively as a source of an additional information for electron identification and separation of electrons from $\pi^0 \to 2\gamma$ decays or from prompt photons, converted outside the active TRD volume. The TRD is not used, however, in the analysis described in this work, because other particle identification criteria turned to be sufficient for the selection of rare $\ell^+\ell^-\gamma$ events (see sec. 4.1.1 and 4.1.2). It might be possible to use this detector for the $Z\gamma$ analysis in the future, particularly for selection of the $Z\gamma \to \nu\bar{\nu}\gamma$ events contaminated by a large $W \to e\bar{\nu}$ background (see sec. 4.4).

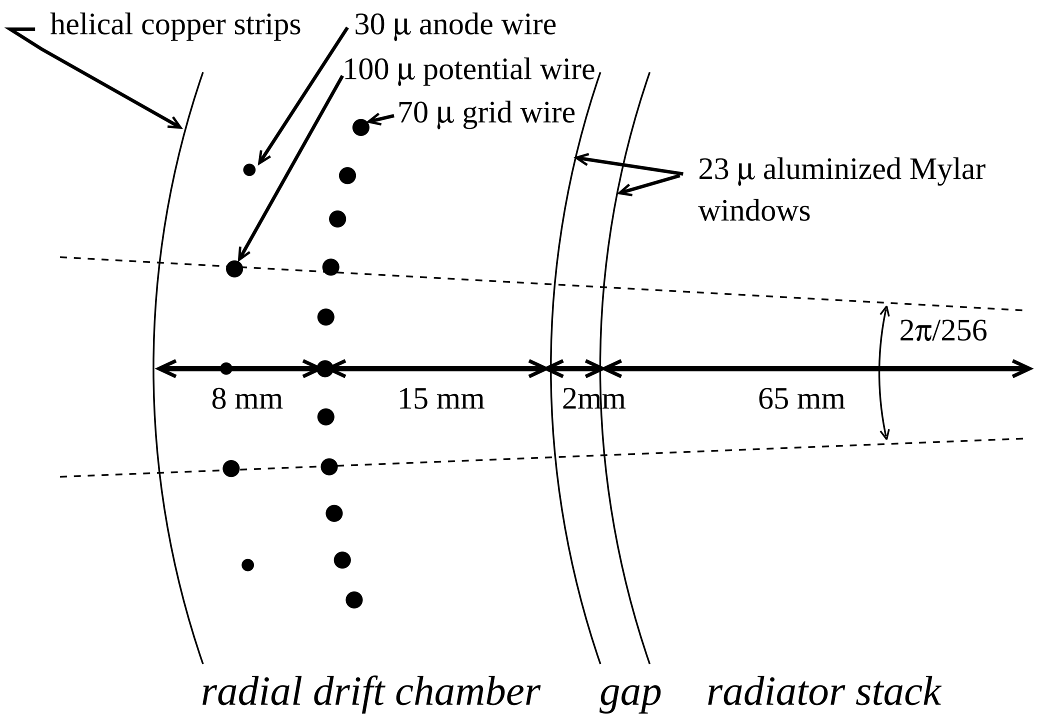

Figure 3.12: End view of a Transition Radiation Detector module.

The TRD detects the transition radiation of an ultrarelativistic charged particle crossing the boundary of two media with different dielectric properties [82]. For the DØ configuration this radiation is primarily emitted in form of X-rays with an energy peaking at 8 keV and mainly contained below 30 keV [57].

The TRD is made of three radial layers. Each layer consists of a radiator followed by a drift chamber for the X-ray detection. The radiator contains 393 layers of 18 μm thick polypropylene foils with a mean separation of 150 μm, in a volume filled with nitrogen gas. A large number of transitions (foil/gas) is essential, since the number of photons radiated in each transition is small.

The detection of the electrons produced by a photoelectric absorption of the X-rays, as well as by ionization induced by the relativistic charged particles passing through TRD, is done in a two-stage time-expansion drift chamber. The X-rays convert mainly in the first stage of the chamber filled by the Xe-based gas mix with low radiation length. The resulting electrons drift radially towards the sense wires in the second stage of the chamber, separated from the first one with a grounded wire grid (see Fig. 3.12). The sense wires measure the collected charge and the arrival time. The z-coordinate is determined by a set of helical copper pads mounted on the outer wall of the chamber.

The drift chambers are subdivided in sectors in ϕ; the inner two have 256 sectors each, and the outer one has 512 sectors, but the wires in the outer chamber are ganged in pairs, so the total number of readout channels for all three TRD layers is the same. The radiator and the chamber are separated by a gap between two concentric Mylar windows. Dry CO_2 gas is flowing inside the gap in order to prevent the pollution of Xe mix with high-penetrating nitrogen gas. The outer window of a gap is aluminized and used as a drift chamber cathode (by keeping it at a negative -1 kV voltage). The windows

Parameter	Specification
Number of layers	3
Radius	$R_{in} = 17.5$ cm, $R_{out} = 49$ cm
Length total/active	188/167 cm
Total thickness	0.081 X_0 at $\eta = 0$
Transition radiation energy	< 30 keV
Radiator foils	393 foils, 18 μm thick polypropylene
Radiator/Gap/Chamber thickness	65/2/23 mm
Gas type	Radiator: N_2; Gap: CO_2; Chamber: 91% Xe+7% methane+2% ethane
Gas pressure	Radiator: 1.012 atm; Gap: 1.010 atm Chamber: 1.008 atm
Sense wire specifications	30 μm Au plated tungsten, at 90 g
Field wire specifications	100 μm Au plated Cu/Be, at 400 g
Grid wire specifications	70 μm Au plated tungsten, at 350 g
Wire voltage	Sense: +1.6 kV; Field: +0.2 kV Grid: grounded
Drift field	0.7 kV/cm
Drift velocity	25 μm/ns
Maximum drift time	0.6 μs
Number of sense wires/layer	256/256/512
Number of pads/layer	256/256/256
Total channels	3×256 (wires) $+ 3 \times 256$ (pads)

Table 3.4: Transition Radiation Detector selected parameters.

are kept cylindrical by maintaining a small pressure difference (≈ 2 mbar) of the three gas mixes used in the modules. Usage of both the time and charge information in the TRD gives a rejection factor of 50 against pions with 90%

efficiency for isolated electrons [57].

Some important parameters of the TRD are listed in Table 3.4 [57, 83].

3.4.3 Central Drift Chamber

The Central Drift Chamber (CDC) [84] of the DØ detector covers the pseudorapidity range $|\eta| < 1.2$ and provides crucial information about charged particle tracks in the central region. This information includes geometrical parameters of tracks and the ionization (dE/dx) on the track.

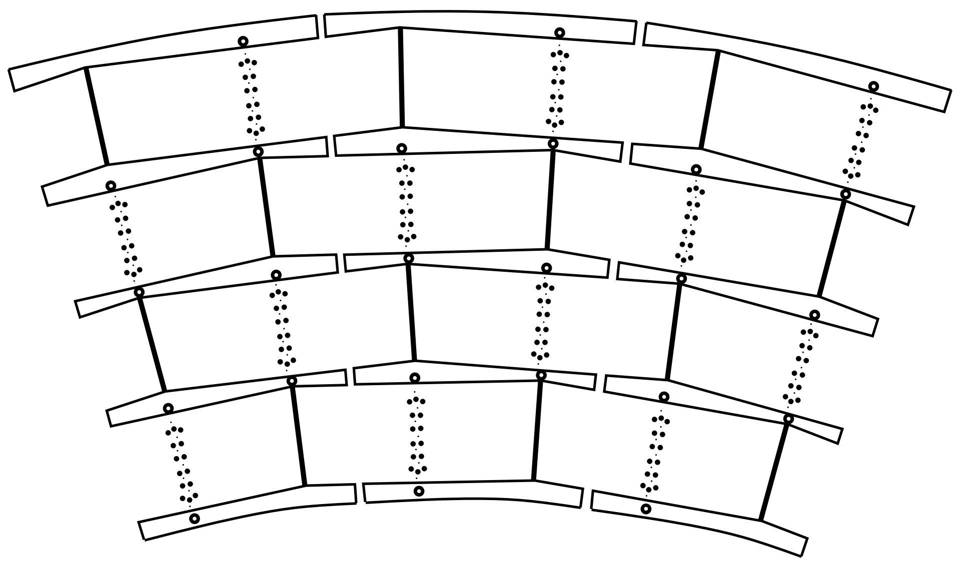

Figure 3.13: End view of a Central Drift Chamber section.

The CDC fills the space between the TRD and the CC cryostat (see Fig. 3.8). It consists of 4 concentric layers of drift cells, 32 cells per layer. Cells in adjacent layers are shifted in ϕ by one half cell for improved pattern recognition in the detector. Each cell has anode wires in the center and cathodes at cell boundaries (see Fig. 3.13). The 7 sense wires of a cell measure the

Parameter	Specification
Radius	$R_{in} = 49.5$ cm, $R_{out} = 74.5$ cm
Length	180 cm
Layers/sectors	4/32
Sense wires	7/cell, 896 total
Sense wire separation	6.0 mm radially, 200 μm stagger
Wire specifications	Sense: 30 μm Au plated W, 110 g tension Field: 125 μm Au plated CuBe; 670 g tension
Delay lines	2/cell, 256 total
Delay line velocity	2.35 mm/ns
Sense wire HV	+1.45 kV (inner), +1.58 kV (outer)
Gas type	93% Ar+4% CH_4 + 3% CO_2 + 0.5% H_2O
Gas pressure	1 atm
Gas gain	$2 \cdot 10^4$ (inner), $6 \cdot 10^4$ (outer)
Average drift field	620 V/cm
Average drift velocity	40 μm/ns
Total channels	$896 + 2 \times 256$
Position resolution	$r\phi$: 180 μm; z: 2.9 mm
Tracking efficiency	88% for isolated tracks

Table 3.5: Central Drift Chamber selected parameters.

drift time which is translated into the coordinate in $r - \phi$ plane. Sense wires are staggered by ± 200 μm for removing left-right ambiguities in hit positions. The z-coordinates are measured by two delay lines located just before the first and just after the last sense wire of a cell.

Mechanically, the CDC assembly is non-typical, since it consists of 32 free-standing modules (each of them in principle can be replaced). The modules are contained in a support cylinder with carbon fiber inner and 0.95 cm aluminium outer surfaces. The outer wall serves as a main support for the whole CDC. Each module is constructed of Rohacell foam covered with epoxy-coated Kevlar cloth and wrapped with a double-layer of 50 μm Kapton [57]. The G10 plastic endpieces hold wire plugs which match holes machined in the outer aluminium endcaps for precise wire positioning. The delay lines (magnetized wire wound around the carbon rods) are located into teflon tubes imbedded in the Rohacell foam. When the avalanche hits outer sense wires, it induces pulses on the delay lines, and the z-coordinate of the avalanche is measured by the difference in the pulse arrival times at the two ends of the delay line.

A single layer scintillating fiber detector with 128 individual fibers was installed on the CDC support cylinder for precise *in situ* calibration of the CDC drift velocities. It is described in detail in Ref. [85].

Major CDC parameters are listed in Table 3.5 [50, 57].

3.4.4 Forward Drift Chambers

The Forward Drift Chambers (FDC's) [67] extend the pseudorapidity coverage of the CDC up to $|\eta| < 3.1$. Two mirror-image chambers are located on the both sides of the VTX/TRD/CDC barrels before the EC cryostat (see Fig. 3.8). The inner FDC radius is 11 cm, and the outer radius of 62 cm is somewhat less than that for the CDC to allow passage of the cables connecting other central detectors.

Each FDC consists of three chambers (see Fig. 3.14) stacked along the

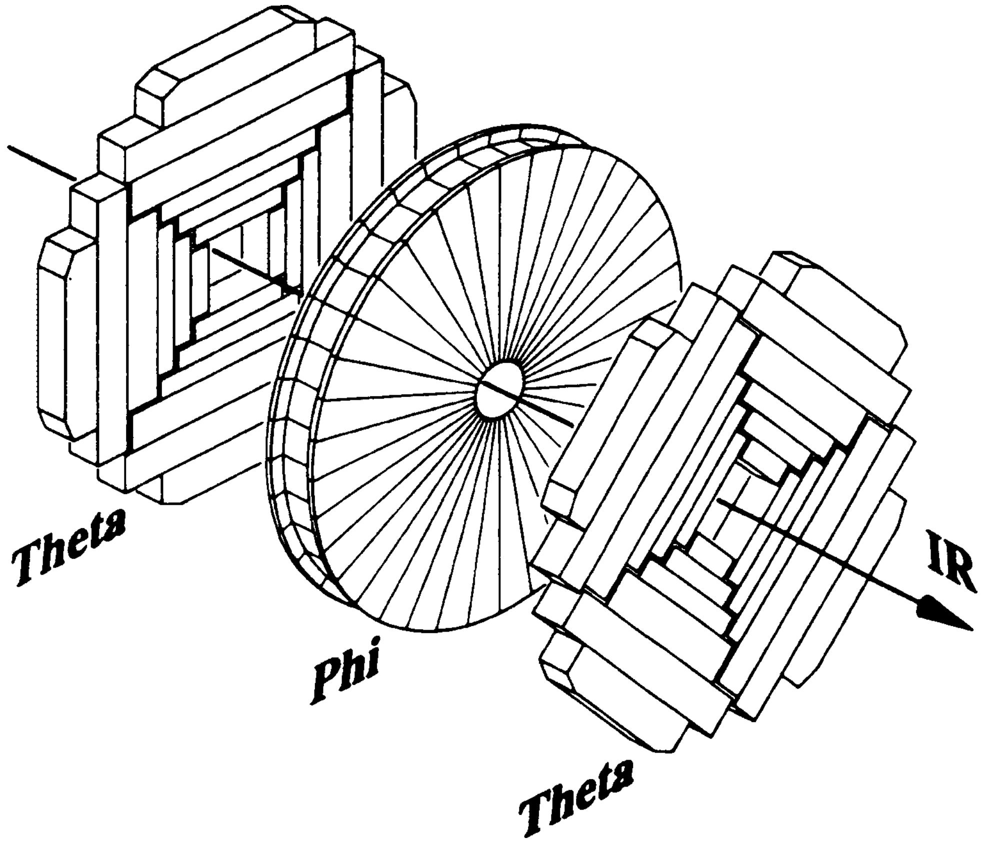

Figure 3.14: Forward Drift Chambers layout.

beam direction. The middle chamber (so called Φ-chamber) has radial wires and measures the ϕ-coordinates of the tracks. The outer two chambers (so-called Θ-chambers) have azimuthal wires and measure the polar angles of the tracks. The Φ-chamber is divided into 36 azimuthal sectors, with 16 sense wires each. The wires traverse the chamber plane along the radii, thus pointing toward the beam. Each Θ-chamber consists of four independent quadrants, each containing 6 rectangular cells at increasing radii. Each cell has 8 sense wires parallel to the beam direction. The inner 3 chambers are made of half-cells (so that electrons can drift only in one direction) which aids in resolving

Parameter	Θ-chamber	Φ-chamber
Radius	$R_{in/out} = 11.0/62.0$ cm	$R_{in/out} = 11.0/61.3$ cm
Position in $\lvert z\rvert$	$104.8 - 111.2$ cm $128.8 - 135.2$ cm	$113.0 - 127.0$ cm
Modules	4 quadrants of 6 layers	36 sectors
Sense wires	8 per cell, 192 total	16 per cell, 576 total
Sense wire separation	8.0 mm with 200 μm stagger	
Wire material/ tension	Sense: 30 μm Au plated W/$50 - 100$ g Field: 163 μm Au plated Al/$100 - 150$ g	
Delay lines	1 per cell, 24 total	none
Delay line velocity	2.35 mm/ns	N/A
Sense wire HV	+1.66 kV	+1.55 kV
Gas type	93% Ar+4% CH_4 + 3% CO_2 + 0.5% H_2O	
Gas pressure	1 atm	
Gas gain	Inner wires: $2.3 \cdot 10^4$ Outer wires: $5.3 \cdot 10^4$	$3.6 \cdot 10^4$
Average drift field	40 μm/ns	37 μm/ns
Maximum drift distance	5.3 cm	
Position resolution	≈ 300 μm	≈ 200 μm
Total channels	1×192 (wires) + 2×24 (delays)	1×576 (wires)
Efficiency	82% for isolated tracks	

Table 3.6: Forward Drift Chambers selected parameters.

left-right ambiguities. Adjacent sense wires of both Θ and Φ chambers are staggered by ± 200 μm for the same purpose. The outer Θ-chambers are rotated by $\pi/4$ one relative to the other for further improvement of pattern recognition. Each Θ-cell is equipped with one delay line (similar to ones used in CDC, see sec. 3.4.3) for measuring the z-positions of the hits.

The cell walls are made of G10 plastic or Kevlar coated Nomex covered with Kapton. As in the CDC, the cathodes are made of conductive strips attached to the walls of the supporting structure. Each cell of the Φ-chamber has a single field shaping wire; there are two analogous wires in the Θ-chamber cells. The FDC uses the same gas mixture as the CDC (see sec. 3.4.3).

The major parameters of both Θ and Φ chambers are listed in the Table 3.6 [50, 57, 67].

3.5 Muon System

Muons are highly penetrating particles, since they interact with matter only via electromagnetic or weak forces. Being heavy particles (if compared to electrons) they typically do not lose much energy via *bremsstrahlung* in the detector material; the energy loss mostly occurs due to the ionization of the detector media. Thus, muons with energy above a certain threshold ($\approx 3.5 - 5.0$ GeV) pass through the entire DØ detector. Therefore, the muon detection system is located outside the calorimeter, and it is well protected from the debris from the hadronic and electromagnetic showers by the massive calorimeter material (see sec. 3.3).

The DØ muon system consists of five separate solid-iron toroidal magnets and several multilayers of drift tube chambers. It covers the pseudorapidity range up to the very forward region ($|\eta| < 3.6$) (see Fig. 3.15). The central toroid (CF) (see Fig. 3.16) covers the pseudorapidity range $|\eta| \leq 1.0$, and

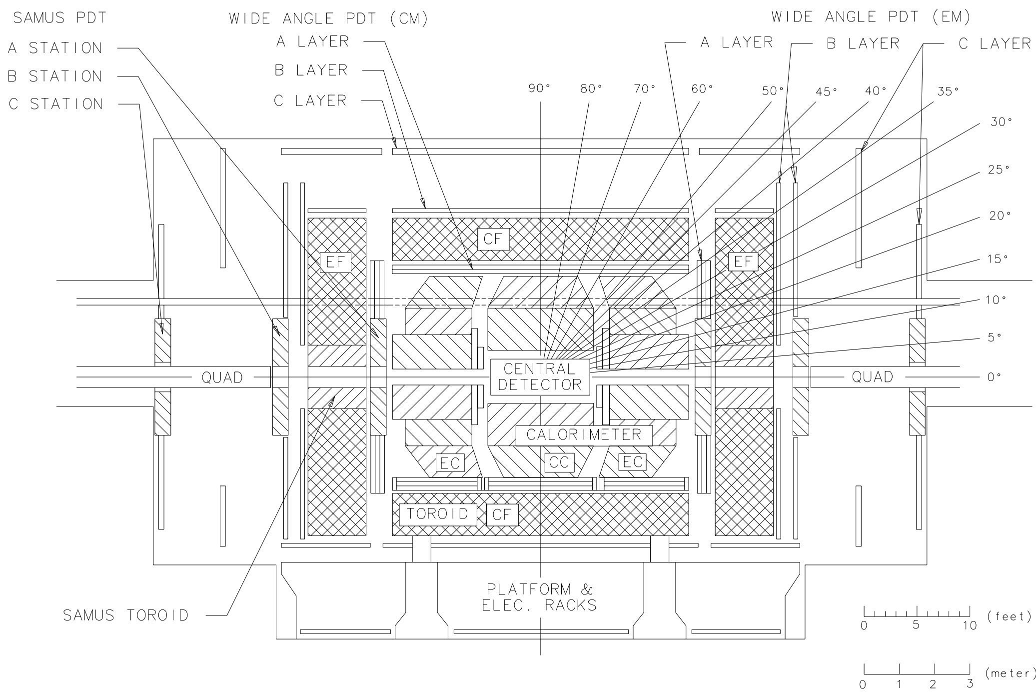

Figure 3.15: Muon System side view.

two end toroids (EF) extend the coverage to $|\eta| \leq 2.5$. They are the parts of the Wide Angle Muon System (WAMUS). The Small Angle Muon System (SAMUS) differs from the WAMUS. The two SAMUS toroids fit the holes in the EF toroids and cover the rest of the pseudorapidity range above. The magnetic field in the toroids varies across the square cross section, peaking at about 2 T. The field lines are azimuthal so that muon tracks are bent in the $r - z$ plane. Muon reconstruction uses a precise field map obtained by special pre-run measurements. The thickness of the calorimeter and toroid material (expressed in the interaction lengths) as a function of the polar angle θ is shown in Fig. 3.17.

The muon system readout electronics is mainly located on the chamber modules. Signal shaping, time-to-voltage conversion, chamber monitoring and

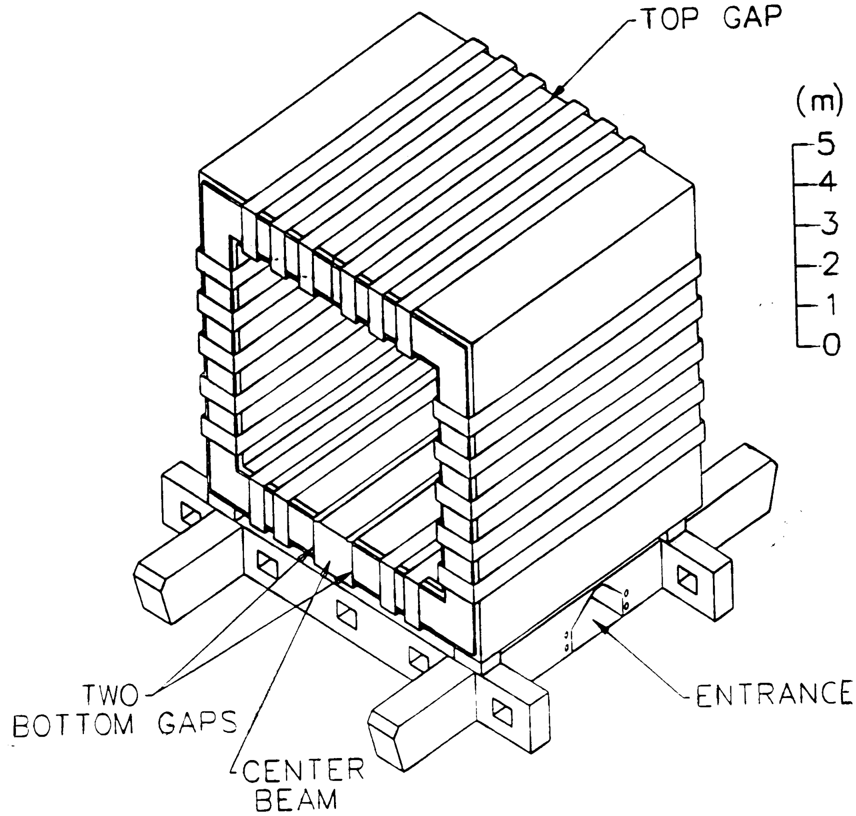

Figure 3.16: Muon System CF toroid.

signal multiplexing is done locally, while the digitizing and the trigger electronics reside outside the detector. Each electronic module processes signals from 6 adjacent drift cells. Digitizing of the muon signal is done with the 12-bit ADC's, analogous to those used in the calorimeter electronics (see sec. 3.3). There is a total of 50,920 analog channels in the system. As for the calorimeter case (see sec. 3.3.2), the coarse information about the muon event is passed to the Level 1 trigger using one latch bit per each PDT (see sec. 3.6). The Level 1/1.5 muon trigger uses the locations of the hit tubes for a coarse estimation of the number of muon candidates and their transverse momenta.

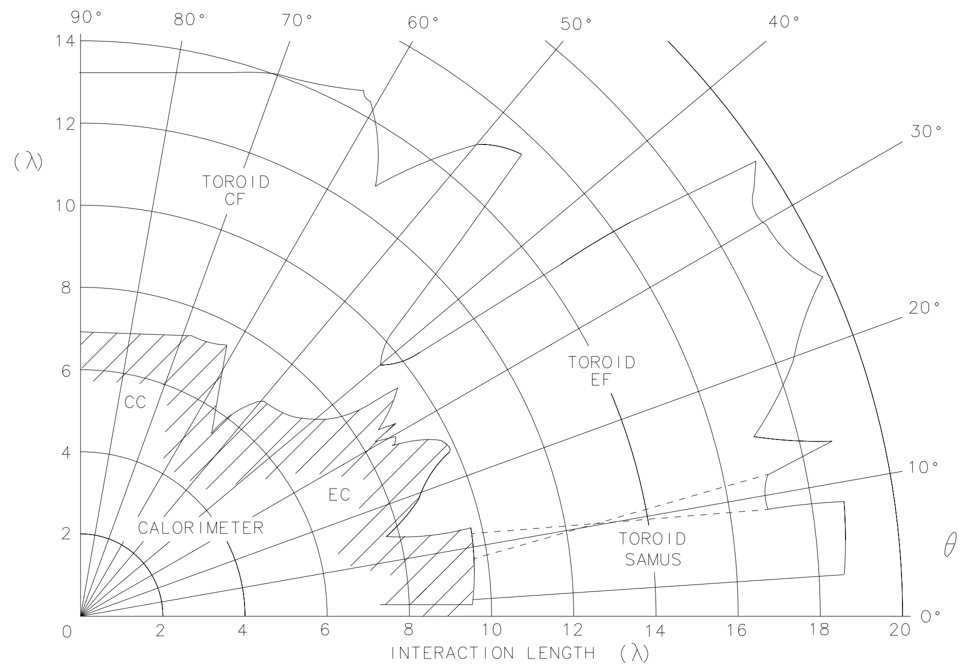

Figure 3.17: Amount of calorimeter and muon toroid material as a function of the polar angle.

The following sections discuss details of the SAMUS and WAMUS detectors.

3.5.1 Wide Angle Muon System

The Wide Angle Muon System (WAMUS) [86] provides measurements for all muons crossing the CF toroid and for most of the muons traversing the EF toroids. It covers the pseudorapidity range $|\eta| \leq 1.7$, and consists of 164 proportional drift tube chambers (PDT's) with chamber wires oriented along the magnetic field lines. The PDT's are grouped into 3 superlayers. The innermost, A-layer, is located inside the toroidal magnets, and the two outer layers, B and C, surround the magnet (see Fig. 3.15). The A-layer has four planes of PDT's; the B- and C-layers have three planes each. The PDT planes are shifted relative to each other in order to resolve left-right ambiguities as shown in the end view of a typical three-plane layer (see Fig. 3.18). There is a total of 11,386 PDT's in WAMUS. The WAMUS chambers are grouped into 8 sections (octants) in ϕ for triggering purposes.

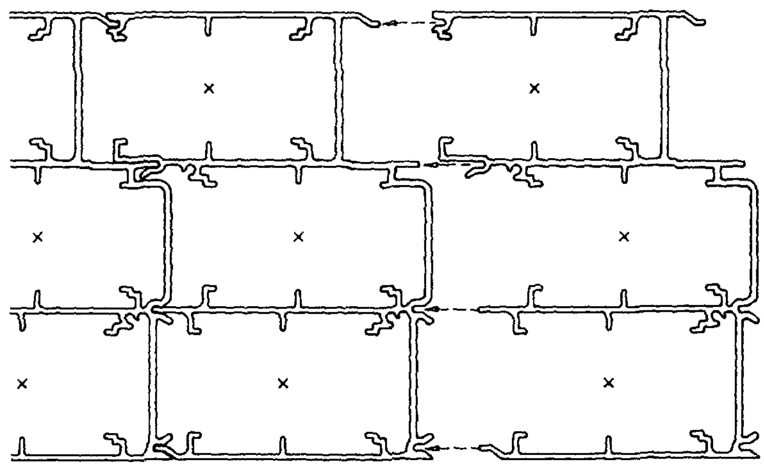

Figure 3.18: End view of a WAMUS chamber assembly.

An approximate drift field map in a single PDT is pictured in Fig. 3.19. The active volume of each PDT measures 102×55 mm^2. The cathode pad strips are located at the top and bottom of the tubes, and a single 50 μm anode wire is situated in the cell center. The anode wires and cathodes are held at +4.56 kV and +2.3 kV, respectively, with aluminium PDT walls being grounded. Tubes are filled with an $Ar/CF_4/CO_2$ gas mixture which yields 65 μm/ns drift velocity. The maximum drift distance is 5 cm. The coordinate in the direction of the wires (non-bend view) is measured with the cathode

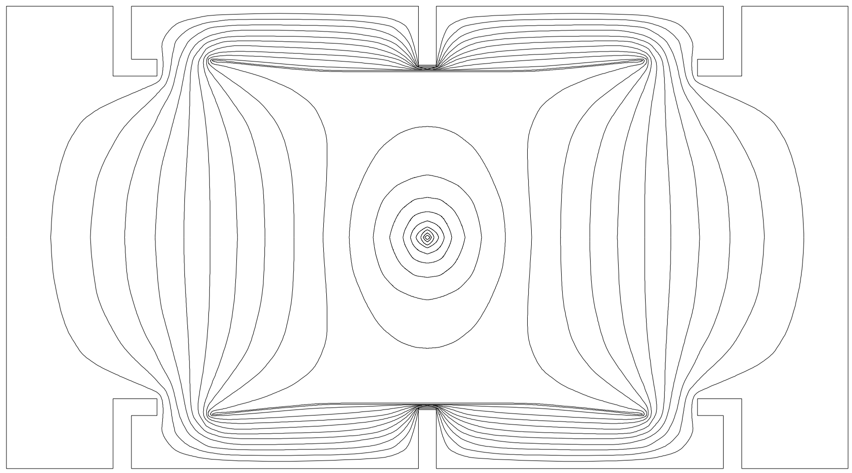

Figure 3.19: Drift field map in a WAMUS cell.

pads and using the timing information from the wires. (The wires of adjacent cells are jumpered at one end, and the signals are read out from the other end, which allows to measure a coarse hit position by the difference in the arrival times.)

The position resolution is 1.6 mm along the wires and 0.53 mm in the drift plane [57]. The muon momentum resolution of the WAMUS can be approximately described as [57]:

$$\left(\frac{\sigma(\frac{1}{p_\mu})}{\frac{1}{p_\mu}}\right)^2 = 0.18^2 + (0.01 \cdot p_\mu[\mathrm{GeV}/c])^2. \tag{3.6}$$

It is asymmetrical in p_μ because the momentum is calculated from the inverse of the track saggita. Some of the WAMUS parameters are listed in Table 3.7.

Parameter	WAMUS	SAMUS
Rapidity coverage	$\|\eta\| \leq 1.7$	$1.7 \leq \|\eta\| \leq 3.6$
Magnetic field	2 T at maximum	2 T at maximum
Number of chambers	164	6
Interaction lengths	13.4	18.7
Gas type	90% Ar/5% CF_4/5% CO_2	90% CF_4/10% CH_4
Avg. drift velocity	65 μm/ns	97 μm/ns
Anode wire voltage	+4.56 kV	+4.0 kV
Cathode pad voltage	+2.3 kV	N/A
Number of PDT's	11,386	5,308
Bend view resolution	$\pm$0.53 mm	$\pm$0.35 mm
Non-bend resolution	$\pm$3 mm	$\pm$0.35 mm

Table 3.7: Muon system characteristics.

3.5.2 Small Angle Muon System

The Small Angle Muon System (SAMUS) [87] is not used for the analysis discussed in this work, so we give only a brief description of this detector. The SAMUS system also have three superlayers of PDT's. However, the higher occupancy of the forward region requires smaller PDT's. They are made of stainless steel tubes (3 cm in diameter) filled with CF_4/CH_4 gas mixture which yields a drift velocity of 97 μm/ns. The maximum drift time is 150 ns. Like in the WAMUS case, the A-layer is located inside the toroid, while B- and C-layers are mounted outside. Each layer has three planes of PDT's oriented in x, y, and u-directions (the u-direction is rotated by 45° degrees with respect to the x and y axes). There is a total of 5,308 PDT's in SAMUS [57].

The position resolution in a single drift tube is 0.35 mm. Some of the important SAMUS parameters are listed in Table 3.7 [57].

3.6 Trigger and Data Acquisition

But we stuck to our starboard triggers

Though we yawned like dying cod.

Raymond Asquith, Letter, 4 March, 1900

The DØ detector works in a high-luminosity environment with a large number of particles traversing its active volumes for each collision. However, only a tiny fraction of events are of physics interest. In order to uncover these valuable events from the huge background of primarily elastic or minimum bias $p\bar{p}$ interactions, the DØ detector uses a complex multilevel trigger [57].

The DØ trigger framework is organized into 3 main levels of increasingly sophisticated event selection (see Fig. 3.20). The scintillator-based hardware Level 0 trigger deals with all $p\bar{p}$ collisions (which occur with a typical rate of 350 kHz at $5 \cdot 10^{30}$ cm^{-2}s^{-1} luminosity), and detects the occurrence of an inelastic collision. It reduces the input rate by about a factor of 3. The Level 1 triggers are based on hardware elements arranged in a flexible architecture via software specifications. Many of the Level 1 triggers operate within 3.5 μs time interval between bunch-crossings, thus contributing nothing to the deadtime (see Chapter 4). They typically slow down the counting rate to 200 Hz. Others require several bunch-crossing times for decision making and are referred to as Level 1.5 triggers. The Level 1.5 triggers suppress the event rate by an

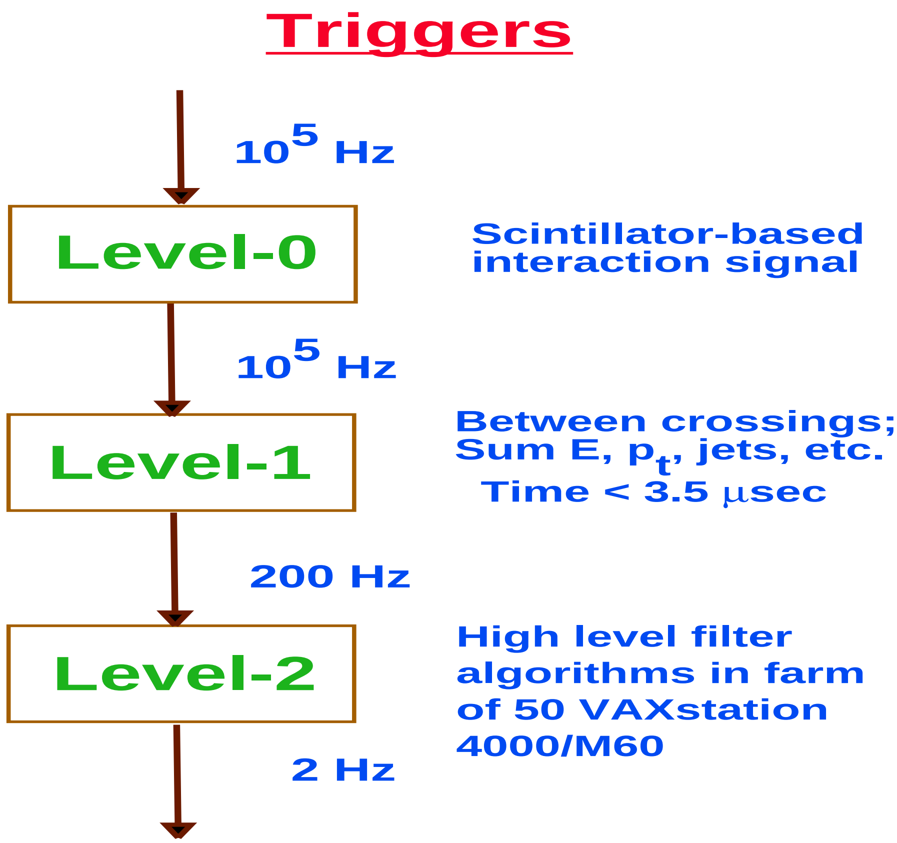

Figure 3.20: Trigger organization and typical trigger rates.

additional factor of 2. The output of Level 1 and Level 1.5 triggers is fed into the standard DØ Data Acquisition (DAQ) System and passed to the last, Level 2, trigger. The Level 2 trigger is software based. The event selection is done by a microprocessor farm which performs a coarse reconstruction of the event parameters, and uses calorimeter and tracking information for decision making. The events which pass at least one out of a broad collection of the Level 2 triggers are passed to the host computer (with a typical rate of 2 Hz) for recording and monitoring. A simplified block-diagram of the Level 2 trigger and DAQ system is shown in Fig. 3.21.

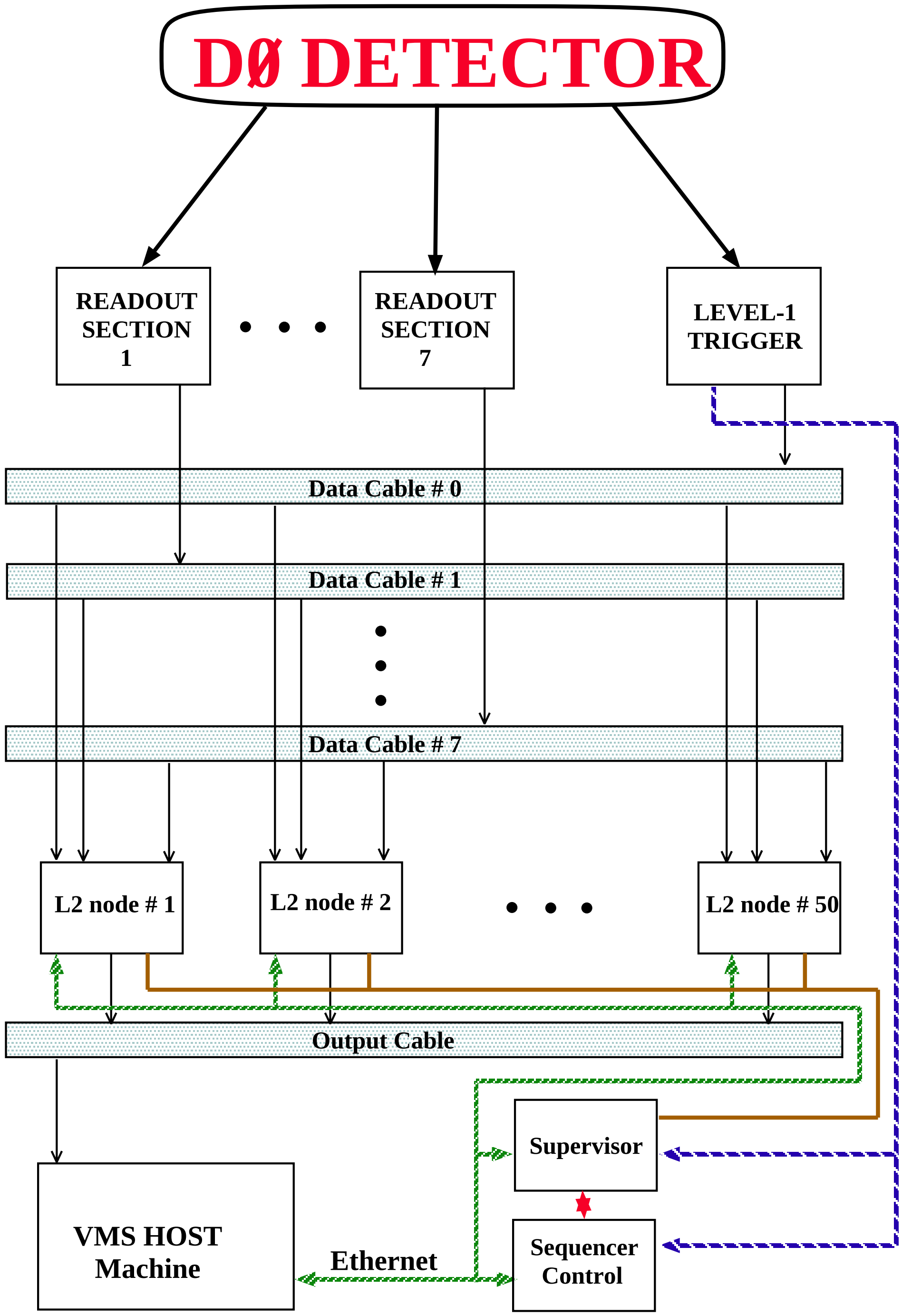

Figure 3.21: A simplified view of the Level 2 trigger and Data Acquisition System.

3.6.1 Level 0 Trigger

The Level 0 trigger [88] detects inelastic collisions and also serves as a luminosity monitor for the experiment (see sec. 3.6.7). The trigger is based on two scintillating hodoscopes mounted on the front surfaces of the EC's (see sec. 3.3). The hodoscopes have a partial coverage for the pseudorapidity range $1.9 < |\eta| < 4.3$, and a full coverage for $2.3 < |\eta| < 3.9$. The trigger is $\approx 99\%$ efficient for non-diffractive inelastic collisions. The Level 0 trigger also roughly measures the z-position of the interaction vertex by the time difference of the signals in the two hodoscopes. The z-position is then used by the Level 1 trigger for correcting the transverse energy. The vertex position resolution is $\sigma_z \approx 3.5$ cm for single interaction events and ≈ 6 cm for the case of multiple interactions [88]. A cut on the vertex position ($|z_{vtx}| < 100$ cm) is made at the Level 0 in order to separate $p\bar{p}$ collisions from the beam interactions with the residual gas. The Level 0 trigger also marks the event as a single or multiple interaction according to the spread of the signal arrival times in each hodoscope. The Level 0 trigger decision making is done completely by hardware. A rough vertex position (the so called "fast vertex") is measured within 0.8 μs after the interaction, and more precise ("slow vertex") information is available within 2.1 μs.

3.6.2 Level 1 Trigger

The Level 1 trigger [89] logic uses several inputs: Level 0 information, Level 1 Calorimeter trigger, Level 1 Muon trigger, Level 1 TRD trigger (the latter was not used in run Ia), and certain timing information, as shown in Fig. 3.22. Typical output of the Level 1 Calorimeter and Muon triggers is the number of struck trigger towers (see sec. 3.3.2), the transverse energy deposited in these towers, and the number of muon candidates and their p_T (see sec. 3.5). These quantities are fed into the Level 1 trigger framework which is based on the two-dimensional AND–OR network, which converts up to 256 inputs into a 32-bit word with the Level 1 trigger information. An event passes the Level 1 trigger if at least one bit of the trigger word is set.

Some of the Level 1 bits were prescaled, which means that they were set for only every k-th event which passes the corresponding path of the logical network. The numbers k are different for different bits and in general depend on the luminosity. The prescale technique makes it possible to collect samples of events corresponding to large cross section processes, such as multijet production, minimum bias events, etc. Without such a prescale these events would simply oversaturate the trigger and DAQ system bandwidths making the detector incapable of collecting rare and more interesting data. More flexible, Level 2 prescales are used in run Ib, allowing for unprescaled Level 1 triggers (see sec. 3.6.4).

Additional information used by the Level 1 trigger is the Main Ring activity (see sec. 3.1). Since the Main Ring of the Tevatron passes through the DØ detector and continuously operates during the collider run for stacking antiprotons, caution must be used when collecting the data during the Main Ring activity periods.

There are two trigger terms which were used during run Ia for vetoing

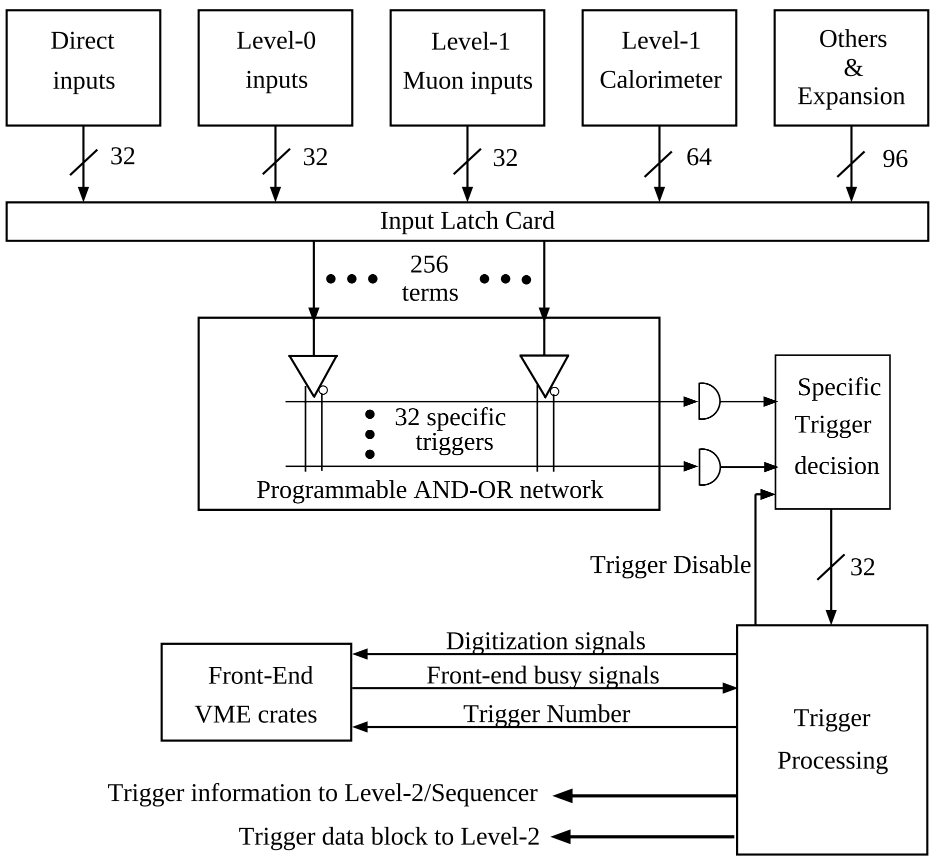

Figure 3.22: A block-scheme of the Level 1 trigger.

events which are likely to be contaminated by the Main Ring beam debris [90]. The first one is the MRBS_LOSS gate with a duration of 0.4 s which occurs during the Main Ring injection and transition, when the activity around the Main Ring results in a high noise in the DØ muon system and calorimeter. Most of the Level 1 triggers do not collect data during this gate. Since Main Ring injection/transition occurs every 2.4 s, the average dead time due to the MRBS_LOSS gate is about 17%. The second type of the Main Ring vetos is the so-called microblanking signal, which is generated if the Main Ring bunches pass through the DØ detector during ± 800 ns livetime of the muon system, centered on the Tevatron bunch-crossing.

Typically, the Level 1/1.5 muon triggers reject events if the microblanking signal is present. Calorimeter based Level 1 trigger still collect the data during the microblanking period, however the quality of this data is rather low, and it is normally rejected during the offline event selection by physics analyses which deal with rare events. Therefore, microblanking contributes $7-9\%$ to the detector deadtime. The total deadtime due to the Main Ring activity is about 25%, and thus quite significant. It was decreased by a factor of 2 in run Ib using the so-called active veto technique [91].

More details on the Level 1 trigger can be found in Refs. [57, 89].

3.6.3 Data Acquisition System

Once an event passes the Level 1 trigger, it is fed into the DØ Data Acquisition (DAQ) System [92] for further analysis by the Level 2 software trigger (see sec. 3.6.4). The system is based on a farm of 48 parallel nodes connected to the detector electronics and triggers via 8 high-speed 32-bit data busses. Each node has a VAXstation 4000-60 or 4000-90 processor (with memory board) connected to a multiport memory used for data exchange via VME bus. The fully digitized data from the calorimeter, CD, muon detector, and Level 0/1 triggers appear in the output buffers of approximately 80 VME crates with ADC's and FADC's about 1 ms after the receipt of the Level 1/1.5 trigger. Each crate prepares compressed information from its modules in a 512 kByte memory module controlled by VME Buffer Driver board which is capable of transferring the data via one of the high-speed busses at a rate of 40 MBytes/s. Each of the 8 busses is used for a particular subdetector or trigger.

The operation of the DAQ system is under the control of the Level 2 trigger supervisor processor, which initiates the data transfer from the VME crates to the multiport memory, and picks a node for the event processing (see Fig. 3.21). Each node has an identical copy of the Level 2 filtering software developed using high-level languages (FORTRAN, C, PASCAL).

Upon reaching the Level 2 nodes, the raw detector data is converted in ZEBRA [93] format, which allows dynamic data structuring and stores information of different types in form of data banks. This format is used in all subsequent data processing (see sec. 3.6.5), and is a standard within DØ.

3.6.4 Level 2 Trigger and Online Processing

The software event filtering performed by the 48 Level 2 trigger nodes (see sec. 3.6.3) reduces the input Level 1/1.5 rate of ≈ 200 Hz to 2 Hz output rate for the data. The filtering software performs a coarse reconstruction of the event parameters and then compares the event characteristics with a set of software-defined Level 2 trigger masks, depending on which particular Level 1 trigger bits were set. As a result, certain Level 2 bits (out of a total of 128 available) are set. A typical Level 2 trigger accepts events which satisfy certain requirements on the transverse energies of the electromagnetic/hadronic jets, number and transverse momenta of muons, missing transverse energy in the event, etc. Some of the Level 2 bits are prescaled in run Ib (see sec. 3.6.2 for prescale definition), thus allowing for usage of the unprescaled Level 1 triggers.

If at least one of the Level 2 bits is set, the event passes the Level 2 trigger, and is temporarily written on disk, and then transferred to 8 mm magnetic tape cartridge (Exabyte format) for further offline processing. All the events which pass Level 2 trigger are combined into the so-called ALL data stream; the events of a particular interest ($\approx 10\%$ of the ALL stream) which pass a certain set of the Level 2 triggers are also copied into an express-line stream (EXP) for immediate reconstruction and analysis. A small fraction of the events ($\sim 1\%$) is fully reconstructed online for the physical and technical monitoring purposes. This is done with the EXAMINE package [94] which runs separately for each sub-detector, and for global monitoring.

A typical event processing time in Level 2 trigger is less than 200 ms, which comfortably meets the Level 1/1.5 output bandwidth.

3.6.5 Offline Reconstruction

The preliminary reconstruction of the event which is done at the Level 2 trigger provides only coarse parameters of the event. The Level 2 timing requirements do not allow for a more thorough reconstruction. The complete event reconstruction is therefore done offline on the fast UNIX farm based on Silicon Graphics processors with a special package named DØRECO [57]. The DØRECO code was continuously improved throughout run Ia, so the data was originally reconstructed by a mixture of different versions of this package.

After the end of run Ia, the whole data set was reprocessed with the latest available version of DØRECO (v.11).

The DØRECO package uses the raw detector data stored in ZEBRA banks by the DAQ system (see sec. 3.6.3) as well as detector and enviromental information (detector surveys, calibration constants, etc.) stored in separate databases as an input. There are two output streams produced by the reconstruction program: the STA stream and the DST stream. The STA (STAndard) output contains raw detector information and various additional ZEBRA banks created by DØRECO during the full event reconstruction, such as banks with reconstructed hits, tracks, calorimeter clusters, identified particles, etc. The STA output files are typically large ($\approx$ 600 kBytes/event) and therefore used only at the final event selection stages, when the number of candidate events is small — typically for event display purposes. The DST (Data Summary Tape) stream contains a reduced version of the STA data. All raw detector data and most of the banks created on the intermediate reconstruction stages (such as hit-finding) are dropped. Only the physics information such as kinematical parameters of the identified particles and jets, compressed calorimeter information, and all parameters relevant to the missing transverse energy calculations are kept for the DST stream. The size of the DST files is approximately 50 times smaller than the STA output, which makes it possible to keep a significant sample of the events on the computer disks for fast physics analysis. At the same time, the information contained in the DST files is sufficient for application of most of the offline selection criteria, like the ones described in Chapter 4.

Details of the particle assignment, jet reconstruction, missing transverse energy calculations, etc. can be found in Chapter 4 and in Refs. [50, 69, 95].

3.6.6 High Voltage Power

All DØ subdetectors use standard High Voltage (HV) power supplies. A special VME based and computer controlled HV system [96] was developed for the DØ detector. Each VME crate contains 6 power supplies (modules) controlled by a Motorola 68020 microprocessor. Three different modules are used in DØ: negative and positive supplies with the voltage of 10 V to 5.6 kV (in 1.36 V increments) at maximum current of 1.0 mA, and positive supplies with the voltage of 10 V to 2.0 kV (in 0.49 V increments) at 3.0 mA maximum current.

The system is controlled and monitored by the host computer capable of changing the operational voltages on different subdetectors and monitoring the HV trips initiated by over-current or over-voltage. A special package for high-level monitoring and quick setting of different operational parameters of the HV system is used for HV control during the data taking. The system is capable of keeping the HV within 0.5 V of the desired value.

For more details on the DØ HV system see Ref. [57].

3.6.7 Luminosity Monitoring

The instantaneous luminosity monitoring is an important issue for any collider experiment, since precise cross section measurements completely rely on the known integrated luminosity of the data sample.

The DØ detector uses the rate for non-diffractive inelastic collisions for luminosity monitoring. This information is provided by the Level 0 scintillating hodoscopes (see sec. 3.6.1). Several corrections to the raw counting rate of the hodoscopes are applied in form of the so-called scalers at Level 1 trigger. Each of a total of 6×32 scalers correspond to one out of 6 possible bunch-crossings, and to one out of 32 possible Level 1 trigger bits. The scalers take into account the multiple interaction factor, the experimental dead time, possible Level 1 trigger prescales, the Main Ring activity veto (see sec. 3.6.2), and others corrections. See Ref. [97] for details.

The calibration of the luminosity monitor is based on the world average values of the total, elastic, and single diffractive cross sections, using the results from CDF [98] and E710 [99]. We use the average of 58.9 pb for inelastic and 9.5 pb for single diffractive cross sections [100]. The systematic error of the normalization constant is 12%. The major sources of systematics are the uncertainties in the efficiency and cross section measurements. It expected to be reduced in run Ib.

The values of the instantaneous luminosity are in agreement with the accelerator division information, based on the measurements of the beam current in the accelerator and on other store parameters [101]. However, this information is available only when beam conditions are stable, and it does not have all the DØ-specific corrections, therefore it can not be used for trigger-dependent luminosity calculations.

3.7 Monte Carlo

The comparison of the observed $Z\gamma$ signal with the SM predictions and the derivation of the limits on anomalous couplings rely very much on dependable and precise Monte Carlo calculations. There are several requirements which a Monte Carlo event generator must satisfy.

First, the generator should take into account the interference effects between production, trilinear, and decay diagrams and be capable of calculating total and differential cross sections of the reaction (2.7) for both the SM and anomalous cases. Second, the generator must simulate response of the different parts of the DØ detector and take into account various particle identification efficiencies, trigger effects, etc. And third, the generator must be capable of producing a large number of events fast. The last requirement is essential because anomalous effects are pronounced only at high p_T^γ, where the SM cross section is very small, and in order to make a precise fit of the p_T^γ spectrum (see sec. 5.2) one needs a significant number of events generated in the high photon transverse momentum region, which corresponds to thousands of the events in the whole phase space used for the analysis. Such a huge event sample should be generated many times for different values of couplings in order to derive the limits. And still more events need to be generated to optimize the set of cuts and derive systematic errors.

Currently there are two event generators which have $Z\gamma$ matrix elements incorporated. The first one is PYTHIA [102] which is capable of generating only SM $Z\gamma$ events. Unfortunately, it does not properly take into account the effects of the finite Z width and the interference between initial and final state radiation diagrams (see Fig. 2.2). Therefore, it fails the requirements listed above. The second generator by U. Baur and E.L. Berger [20] (in what follows called BAUR[2]), briefly described in 2.3.3, does have a full set of matrix elements necessary for the calculations of the processes (2.7), (2.9), and the capability to calculate the contribution of anomalous couplings. However, the detector simulation part of the original generator is rather simple and does not take into account hadronization effects, and the underlying event structure, as well as fine details of the DØ detector.

There are two options for incorporating the instrumental effects into the event generator. The first is simply to use the output of the BAUR generator (4-momenta of the final state particles) as an input for a comprehensive DØGEANT detector simulation program [103]. The overlap with the underlying event and conversion of the data into the GEANT format in this case can be done by means of the ISAJET event generator [104], which is a standard tool within DØ. However, the generation of thousands of events with the GEANT detector simulation is a very resource-consuming and slow task. Besides, it relies very much on a precise description of different detector components, which is not always in agreement with the measurements based on real data. Instead, we decided to use the other option and modified the original BAUR code to include a fast "toy Monte Carlo" simulation of the DØ detector as a part of this generator. Such a modified code in what follows will

[2]Authors' permission obtained.

be called DØBAUR.

The instrumental resolutions, particle identification efficiencies, trigger turn-on curves, and other crucial detector-specific parts of the fast simulation, are wherever possible based on data collected in the same run. Usage of the data-based numbers also takes into account the effects of the multiple interactions, underlying event, etc. Most of the efficiencies will be discussed in detail in Chapter 4, so here we will just list the main effects which were taken into account.

- Smearing of electron/photon and muon momenta as well as the missing transverse energy according to the resolutions (3.3), (3.6), and (3.5), respectively.

- Primary vertex longitudinal position displacement ($z^0_{vtx} = -11.0$ cm) and smearing ($\sigma_z = 29.0$ cm).

- Photon, electron, and muon identification efficiencies (see sec. 4.1 for details).

- Photon losses due to conversions in the material in front of the calorimeter and random track overlap (see sec. 4.1.2).

- Level 1 and 2 trigger efficiencies and turn-on effects (see sec. 4.2 and 4.3).

- Geometrical acceptance and CC/EC gap effects (see sec. 3.3).

- Transverse kick of the $Z\gamma$ system due to the associated jet production. The transverse momentum of the $Z\gamma$ system is generated according to the observed Z boson p_T distribution [105]. Presently, no complete theoretical calculation of the $Z\gamma$ p_T distribution (including soft gluon resummation effects) exists. However, the shape of the $Z\gamma$ transverse momentum distribution is expected to be similar to that in the Z boson production.

The code was transported and primarily used on DEC Alpha platforms which allows for a fast generation of high-statistics samples. The standard output of the generator is a total cross section within the cuts and a set of histograms with different kinematical distributions, like those shown in Figs. 2.3 – 2.7. An interface for writing out unweighted events for further processing with DØGEANT was also incorporated into the code for future studies of the detector response. Additionally, the program has a flag which allows for the choice between the muon and electron channels during the simulation.

An important question is the systematic error on the calculated cross section. Several different uncertainties contribute to this error. They are summarized in Table 3.8 for the electron and muon channels.

The sources of the detector related uncertainties are described in detail in Chapter 4. The momentum smearing error was calculated by varying the smearing parameters by $\pm 1\sigma$. For the muon channel the uncertainty also accounts for different smearing parameters for the low and high $\int B\,dl$ muons (see sec. 4.3).

The major source of theoretical uncertainties is due to different possible choices for the structure functions. We choose the MRSD$-'$ [29] set of the next-to-leading logarithmic (NLL) order structure functions, because they describe the recent measurements of the W-decay asymmetry [106] as well as other electroweak phenomena better than the other sets of structure functions. We calculated the SM cross section for both channels with 21 different NLL and leading order (LO) structure functions [107]. After neglecting the old and outdated structure functions which contradict other experimental results, we estimated the scattering of the results, and ended up with $\pm 6\%$ estimate on the cross section uncertainties. The band obtained also covers the predictions

Source of error	Systematic uncertainties	
	Electron channel	Muon channel
Detector related errors		
Photon ID efficiency	7%	7%
Dilepton ID efficiency	5%	8%
Trigger efficiency	1%	8%
Random track overlap	1%	1%
Momentum smearing	1%	5%
Theoretical errors		
Structure function choice	6%	6%
Structure function scale	1%	1%
$p_T^{Z\gamma}$ effect	3%	3%
Total	11%	16%

Table 3.8: Sources of the systematic uncertainties in the cross section predictions, as calculated by the DØBAUR generator.

of another popular set of the structure functions by CTEQ [108]. The difference between the cross sections calculated using various structure functions is shown in Fig. 3.23. As is clear from this figure, LO structure functions result in a systematically lower cross section, if compared to the NLL structure functions. The Monte Carlo calculations in the DØBAUR code are based on

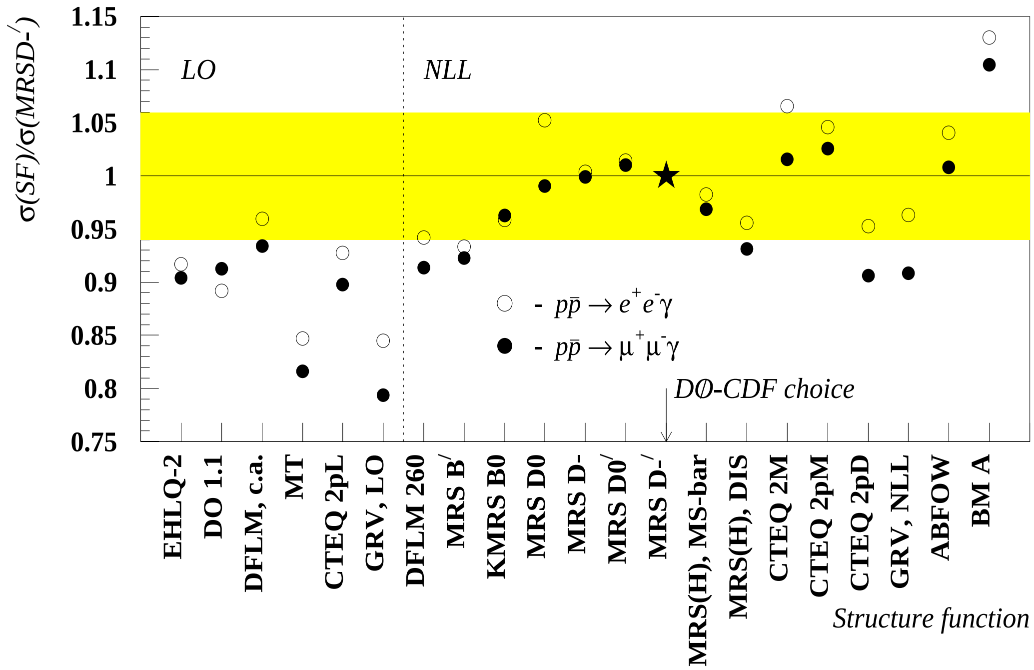

Figure 3.23: SM cross section of reactions (4.1) (open dots) and (4.2) (solid dots) for various sets of structure functions, normalized to that for the MRSD$-'$ set (DØ and CDF default set of structure functions for W/Z-physics, shown with the star). The shadowed band shows the $\pm 6\%$ systematic uncertainties which account for the cross section variations for different sets. Points to the left (right) of the dotted line correspond to LO (NLL) structure functions. Notations for the structure functions are given in Ref. [107].

the LO matrix elements (a full NLL calculation of $Z\gamma$ production, including anomalous $ZV\gamma$ couplings is presently not available). NLL QCD corrections are approximated by a k-factor (see sec. 2.3.3 and 2.3.4), so usage of NLL structure functions is more appropriate [35].

Another type of the theoretical uncertainty is the scale used for the structure function calculations. The error due to different scale definitions was estimated to be $\pm 1\%$ by varying the scale from the nominal value of $Q^2 = \hat{s}$ to $\hat{s}/2$ and $2\hat{s}$. Finally, the effect of the transverse kick of the $Z\gamma$ system due to the associated jet production was studied. It contributes less than 3% to the cross section uncertainty. The error originating from the p_T kick partially reflects the remaining uncertainty from QCD corrections beyond the NLL approximation.

Overall uncertainties in the cross sections for typical cuts (see sec. 4.2 and 4.3) and after the detector response simulation, as calculated by the DØBAUR Monte Carlo, are 11% for $e^+e^-\gamma$ and 16% for $\mu^+\mu^-\gamma$ cases. Combining the two channels, the error is 13%.

Chapter 4

Event Selection

Of all that is written I love only what a man has written with his blood.

F. Nietzsche, "Also Sprach Zarathustra"

This chapter contains a detailed description of the selection of the reaction (2.7) events with the DØ detector for both the electron and muon channels:

$$p\bar{p} \rightarrow e^+e^-\gamma; \tag{4.1}$$

$$p\bar{p} \rightarrow \mu^+\mu^-\gamma. \tag{4.2}$$

All available data from the first physics run of the DØ detector (run Ia, 1992–1993) at $\sqrt{s} = 1.8$ TeV was used in these analyses. The total integrated luminosity delivered to DØ by the Tevatron for this run was 27.8 pb^{-1} (see sec. 3.6.7 for details of luminosity calculations). The accepted luminosity, however, was about a factor of two smaller, 14.9 ± 1.8 pb^{-1}. The main reason for this inefficiency is a 27% dead time due to the Main Ring injection and microblanking (see sec. 3.6.2) forced by the fact that the Main Ring of the accelerator passes through the DØ detector. The other contributions to the total 46% dead time are as follows: DAQ system dead time — 8% (see sec. 3.6), HV trips — 6% (see sec. 3.6.6), run startup — 2%, and changing of the triggers — 3%. The integrated luminosities for the specific high p_T triggers used for selection of the electron and muon events are somewhat lower due to corrections for the bad and special runs (see sec. 4.2 and 4.3).

The raw data collected on magnetic tapes (Exabyte format) was reconstructed by version 11 of the standard reconstruction (DØRECO) program [57] — the latest one available for the run Ia (see sec. 3.6.5). Various energy corrections were introduced during the reconstruction. These corrections are necessary due to the different high-voltage and other environmental parameters in the physical run and during the liquid argon calorimeter test beam calibration [72]. Beyond this, we used additional electromagnetic and jet energy corrections [70] before applying specific cuts to the data. These corrections further tune the energy scale of the calorimeter, take into account the invisible energy in the hadronic jets (thus improving the $\not\!\!E_T$ resolution), and adjust the Z mass to the LEP value of 91.2 GeV [9] (see sec. 3.3.7). In what follows, we will use the corrected energies for defining the cuts unless otherwise stated.

4.1 Particle Identification

The selection of the reactions (4.1), (4.2) relies very much on a correct and trustworthy identification of the final state particles: electrons, muons, and photons. In this section we discuss the algorithms used to identify these three types of particles. Most of the algorithms are standard within the DØ Collaboration and are used in various physics analyses. Modifications to these standard algorithms are emphasized in the appropriate sections.

4.1.1 Electron Identification

Since the DØ detector does not have a central magnetic field, the initial stage of electron identification is based on EM calorimeter information. We use tracking information in the CD (see sec. 3.4) to distinguish between electrons and photons. This approach is an alternative to that used in the detectors with a magnetic field where it is possible to measure track curvature and momentum to energy ratio, P/E, and use them for particle identification. For the case of the DØ detector the absence of P/E information is compensated for by fine segmentation of the EM calorimeter, dE/dx measurements in the CDC and FDC (see sec. 3.4), and by the TRD information (see sec. 3.4.2). The major sources of background to electrons at DØ are converted photons and QCD jets with a high fraction of electromagnetic energy. Because of the absence of the magnetic field we are not able to distinguish between electrons and positrons, so in what follows we will talk about electrons, or e's, implying particles of both signs.

The reconstruction program loosely labels an electromagnetic cluster as an electron if there is a track in the "cone" of the width $\approx 0.1 \times 0.1$ in $\theta - \phi$ space, which points from the interaction vertex to the center of gravity of the cluster. (In what follows such a cone will be called the *tracking road*.) Information about the cluster matching such a track is stored in PELC ZEBRA bank (see sec. 3.6.5), while a cluster which fail this requirement is associated with a photon and stored in PPHO bank. Of course, such an assignment is rather poor, and thus both banks are heavily contaminated by background.

However, the DØ finely segmented calorimeter (see sec. 3.3) allows us to suppress these backgrounds drastically by means of a thorough multidimensional analysis of the longitudinal and transverse profiles of the electromagnetic showers. Shower shapes are in general different for the case of an $e^+e^-/\gamma\gamma$ pair and a single electron/photon with the same total energy due to fluctuations of the shower origin for each particle. One would expect a shower from a converted photon/π^0 to develop earlier, because the probability of the initial interaction in the first layer of the calorimeter for two particles is twice as high as that for a single one. At the same time, unlike measurements based on the P/E ratio, the DØ electron identification algorithm is not very sensitive to δ-ray electrons (i.e. electrons kicked out of atoms) and electrons which radiate photons in the material before the calorimeter via *bremsstrahlung*, because secondary electrons and photons generally have much lower energy than the parent particle and thus do not significantly change the shower energy profile.

A further improvement of the electron identification can be achieved by measuring the ionization (dE/dx) along a track in the CD. However, the efficiency of this algorithm for electrons is not very high (about 85% per electron for background rejection factor of 2), so we do not use the dE/dx information in this analysis due to the very limited statistics of the signal events. The TRD information (see sec. 3.4.2) is not used for similar reasons.

The analysis of the shower profile is done by the so-called *H-matrix* algorithm [109]. It analyzes the observed energy depositions in different cells of an electromagnetic cluster found by the reconstruction program (see sec. 3.6.5). In order to compare the energy profile of a particular cluster with the expectations, a 41×41 covariance matrix is built from the energy depositions for the electrons in the Monte Carlo sample. The inverse of this matrix is called the H-matrix. A χ^2-like function is then calculated in a standard way on a cluster-by-cluster basis using the H-matrix as an error matrix. This χ^2-like function is therefore a quantitative measure of the probability that the cluster is due to a single electron/photon. Optimum cuts on the H-matrix χ^2 for electron identification were determined using the electron and pion test-beam data [110].

All cuts for the electron selection which we are going to discuss were studied using the background-subtracted $Z \to ee$ event sample collected in the same run. The efficiency of a certain cut was obtained by comparing the total number of events in the Z-peak before and after the cut was applied. The efficiency for a set of cuts was calculated in a similar way (which correctly takes into account the correlations between cuts). The values of the cutoff parameters were chosen to optimize the signal-to-background ratio in the background-contaminated $Z \to ee$ sample while retaining relatively high efficiency for the signal [111].

The basic set of cuts is summarized in Table 4.1. The efficiency as a function of cutoff parameters is shown in Fig. 4.1 [111]. The cuts used in the analysis are indicated by the arrows in the plot. The cuts are somewhat different for the CC and EC (see sec. 3.3 for the calorimeter description) because of the different amount of material in front of the central and end calorimeters which results in different multiple scattering and conversion probabilities for electrons and photons hitting the CC and EC.

The H-matrix χ^2 cut is a likelihood cut on the cluster energy profile. It has a higher cutoff in the EC because of the larger electromagnetic shower fluctuations in the forward region. The electromagnetic fraction cut accepts only the clusters with at least 90% of the energy being deposited in the electromagnetic layers of the calorimeter. The isolation cut requires the clusters to be rather narrow. The definition of the isolation is as follows:

$$\mathrm{ISO} = \frac{E^{tot}(\Delta R = 0.4) - E^{EM}(\Delta R = 0.2)}{E^{EM}(\Delta R = 0.2)}. \tag{4.3}$$

Here $E(\Delta R)$ is the energy deposited in a cone of radius ΔR in $\eta - \phi$ space.

Cut description	CC		EC	
	Cutoff	ε	Cutoff	ε
H-matrix χ^2	< 100	0.930 ± 0.011	< 200	0.987 ± 0.022
EM fraction	> 0.90	0.995 ± 0.005	> 0.90	0.995 ± 0.005
Isolation	< 0.10	0.970 ± 0.008	< 0.10	0.982 ± 0.023
Loose cuts (all above)		0.902 ± 0.013		0.971 ± 0.029
Track in road	see text	0.879 ± 0.022	see text	0.820 ± 0.024
Track match	$< 10\sigma$	0.977 ± 0.006	$< 10\sigma$	0.881 ± 0.023
Tight cuts (all above)		0.781 ± 0.023		0.708 ± 0.034

Table 4.1: Definitions and efficiencies [111] for the electron identification cuts in the central and end calorimeters.

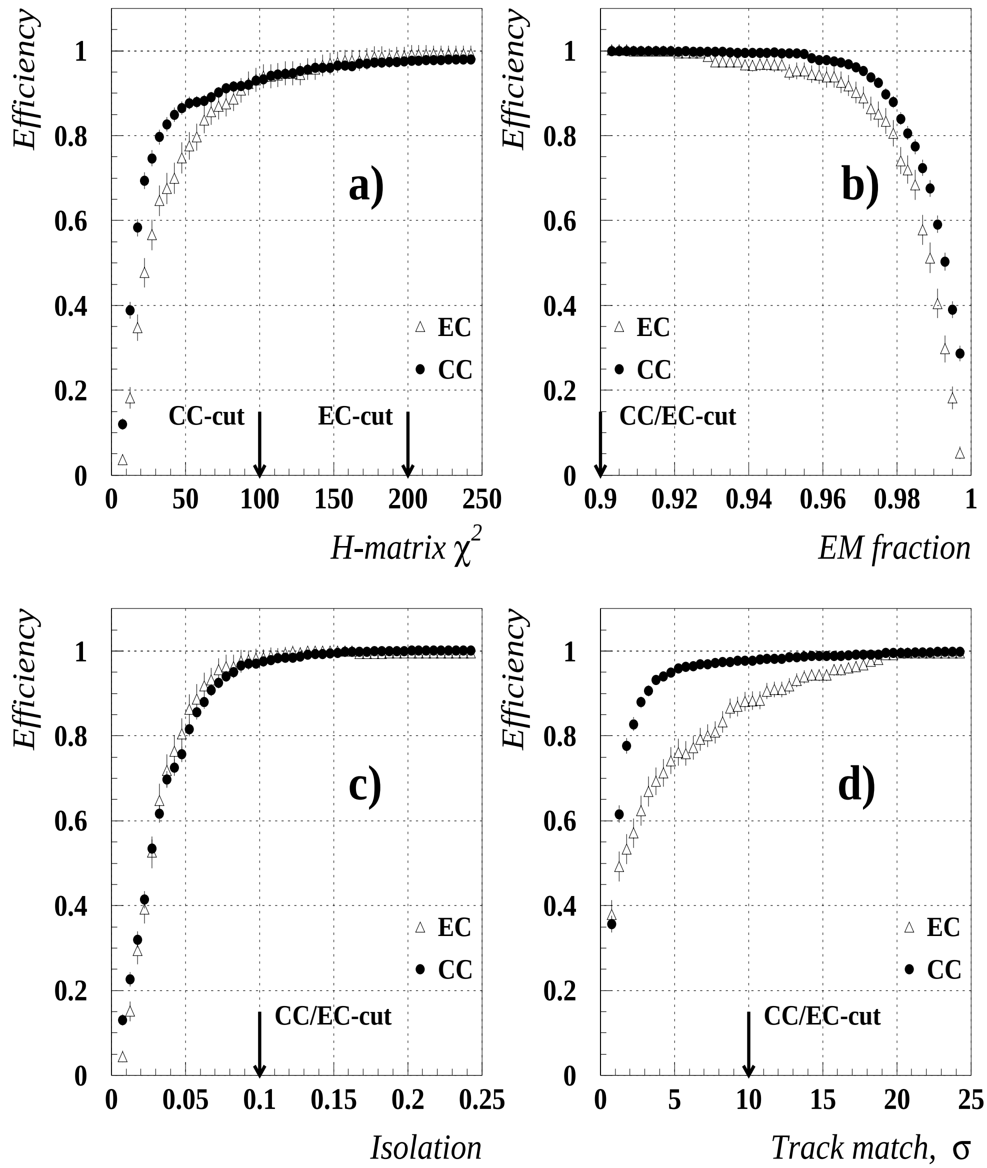

Figure 4.1: Efficiencies for various electron identification cuts: a) H-matrix χ^2 cut; b) electromagnetic fraction cut; c) isolation cut; d) track match significance cut. Dots — central calorimeter; open triangles — end calorimeters. Arrows show the actual values of cutoff parameters used in this analysis.

This cone is drawn from the event vertex to the center of gravity of the electromagnetic cluster. The smaller the value of ISO, the more compact a cluster is. Since an electromagnetic shower should be fully contained in the $\Delta R = 0.2$ cone, this cut selects electrons (photons) which are well separated from other particles (i.e. *isolated*).

The set of these three cuts is called the *loose electron/photon* selection criterion. If in addition the cluster was reconstructed as an electron by DØRECO (see above) and matches within 10σ one of the reconstructed central tracks, we refer to it as to passing the *tight electron* cut. The parameter σ in the track match definition is a combined error of tracking and cluster position reconstruction due to multiple scattering, vertex z-position mismeasurements, etc.

Because of the small signal cross section, and a low expected background (see sec. 4.5), we optimize the selection efficiency by requiring only one electron to pass the tight electron cut, while for the second it is sufficient to satisfy only the loose selection criterion. The motivation for this less stringent requirement is a significant tracking inefficiency which results in $\approx 13\%$ of the electrons to be placed into the PPHO (photon) banks.

The overall electron identification efficiency for two electrons was estimated using the ratio of tight-loose (N_{tl}) to tight-tight (N_{tt}) $Z \to ee$ events. This ratio was measured to be 1 : 3 which is consistent with the tracking efficiency (measured by several other techniques), $\varepsilon_t = 84 - 87\%$ (see Table 4.1):

$$\frac{N_{tl}}{N_{tt}} = \frac{2\varepsilon_t(1-\varepsilon_t)}{\varepsilon_t^2} = 2\left(\frac{1}{\varepsilon_t} - 1\right). \tag{4.4}$$

Identification efficiencies for both electrons in the CC and both electrons in the EC were found to be:

$$\varepsilon_{CC}^{ee} = 0.64 \pm 0.02, \quad \varepsilon_{EC}^{ee} = 0.56 \pm 0.03. \tag{4.5}$$

Efficiencies for the CC–EC topologies were also calculated and used in the DØBAUR Monte Carlo (see sec. 3.7).

4.1.2 Photon Identification

Photon identification is similar to electron identification in the DØ detector. We require an electromagnetic cluster to have no track in the 0.1×0.1 cone in $\theta - \phi$ space (i.e. to belong to the PPHO bank). Beyond this we require the cluster to satisfy loose electron/photon selection criteria (see sec. 4.1.1). Thus, the identification efficiency for a photon which belongs to the PPHO bank is given by the "loose cuts" line of the Table 4.1.

However, a certain fraction of photons are reconstructed as electrons (and thus are misplaced into PELC banks) due to conversions in the material in front of the CDC or FDC and due to the overlap of random tracks with the electromagnetic cluster associated with the photon. The conversion probability, P_c, was calculated [112] using the DØGEANT [103] detector simulation program. P_c as a function of the photon pseudorapidity measured in the calorimeter (η_{det}) is shown in Fig. 4.2 (a) for the case of the interaction vertex in the center of the detector ($\eta_{det} = \eta$). It was then multiplied by the tracking efficiency in order to get η-dependent probability of photon losses due to conversions. This probability was used in the Monte Carlo calculations of the theoretical cross section (see sec. 3.7).

The probability of a random track overlap was calculated using real $Z \rightarrow ee$ data. The electrons in this sample have a similar pseudorapidity distribution as one would expect for photons in the $Z\gamma$ production (see Fig. 2.6). We calculated the probability of observing a random track from the underlying

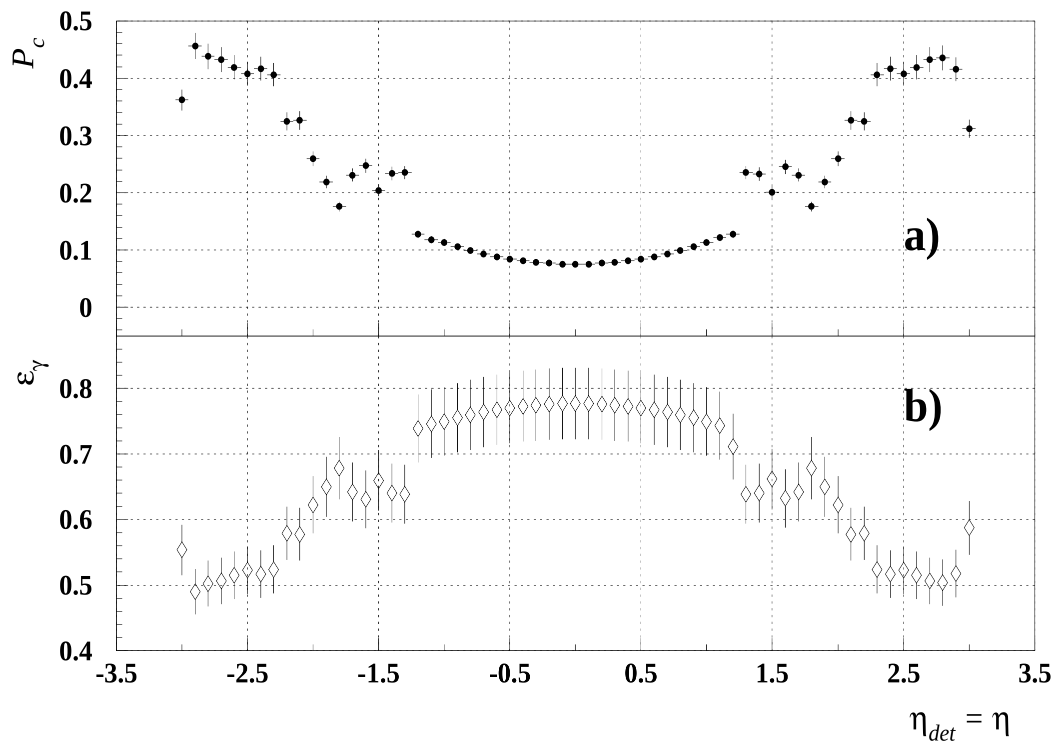

Figure 4.2: a) η-dependent probability for photon conversion (P_c) in the material in front of the CDC/FDC; b) η-dependent efficiency of the photon identification (ε_γ) for high p_T photons. Error bars show a 5% systematic uncertainty in the conversion probability calculations, and an overall 7% systematic uncertainty in the efficiency estimations.

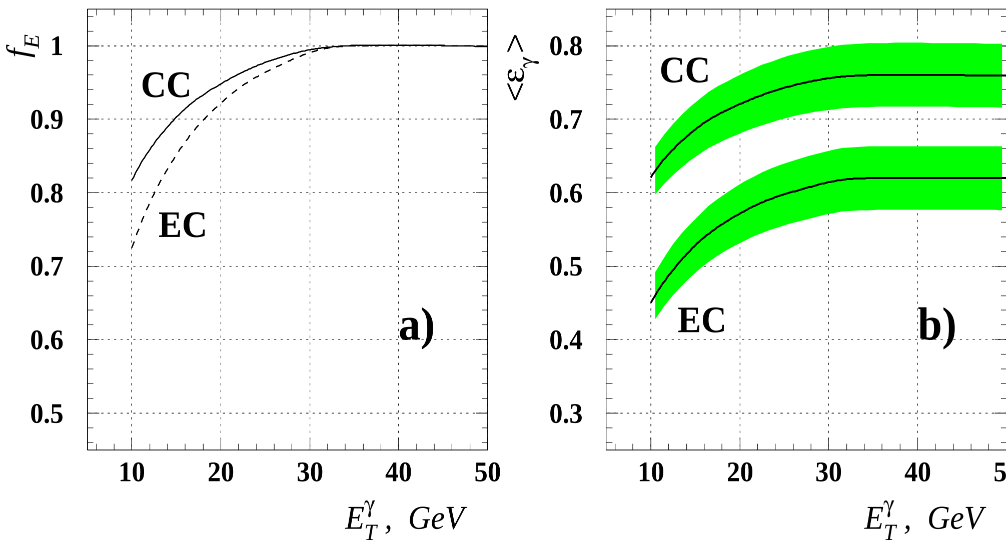

Figure 4.3: a) E_T^γ-dependent correction factor (f_E) for the H-matrix cut efficiency in the CC (solid line) and EC (dashed line); b) E_T^γ-dependent photon identification efficiency, averaged in η_γ, ($\langle\varepsilon_\gamma\rangle$) for CC (upper) and EC (lower); the shadowed bands represent $\pm 7\%$ systematic uncertainty.

event in a random cone of $\theta \times \phi \approx 0.1 \times 0.1$ size — the same as used in DØRECO's coarse electron/photon identification algorithm. The cones have the same η_{det} as electrons in the $Z \to ee$ sample, but the ϕ-coordinate was chosen randomly. The efficiency due to a random track overlap was found to be $94 \pm 1\%$ in CC and $85 \pm 1\%$ in EC, the latter being lower due to the higher density of tracks in the forward region.

The η-dependent efficiency of the photon identification for the $\eta_{det} = \eta$ case after applying loose electron cuts and taking into account conversions and random track overlap losses is shown in Fig. 4.2 (b).

The efficiency of the H-matrix cut in Table 4.1 was calculated for electromagnetic clusters with $E_T > 25$ GeV. For photons we would like to go much lower in transverse energy, so an additional E_T-dependent correction to the efficiency must be introduced. The correction factor as a function of the photon transverse energy was measured in the test beam [110]. It is shown in Fig. 4.3 (a) for the CC (solid line) and EC (dashed line). The overall E_T dependent photon identification efficiency in the CC and EC after integration over a typical η distribution (see Fig. 2.6) is shown in Fig. 4.3 (b).

After taking into account the E_T-dependent corrections, the average efficiencies for photons produced in the reaction (2.7) in the central and forward regions are found to be 67% and 52%, respectively. The overall error in the photon identification efficiency calculations is 7% and is dominated by the systematic errors in f_E and the conversion probability.

4.1.3 Muon Identification

The basic algorithms used for the muon identification were developed and studied in great detail for the top-quark search in the reaction $p\bar{p} \rightarrow t\bar{t} \rightarrow e\mu + jets$ [95, 113] as well as for other physics analyses which involve muons. The efficiencies of the muon identification cuts were calculated using the $W \rightarrow \mu\bar{\nu}$ and $Z \rightarrow \mu\mu$ data and Monte Carlo samples.

The analysis of the reaction (4.2) was restricted to the CF muon system only (see sec. 3.5 for notations) because of the present low efficiency of the forward EF system and higher background from accidentals in the forward region. The muons in the reaction (4.2) are expected to be mostly central, so this restriction does not decrease the acceptance significantly.

Cut description	Cutoff definition	ε
Cosmic rejection cuts		
No back-to-back muon tracks or hits		0.84 ± 0.01
No cross-octant muon tracks		0.99 ± 0.01
Vertex consistence	$d_{3D} < 22.0$ cm	0.99 ± 0.01
Muon quality cuts		
A-layer hits requirement		0.86 ± 0.01
Number of layers hit	$N_L \geq 2$	0.95 ± 0.03
Muon track quality	$IFW4 \leq 1$	0.99 ± 0.01
CD track match	$\Delta\phi < 0.25,\ \Delta\theta < 0.30$	0.95 ± 0.02
Calorimeter MIP deposition	$E > 1.0$ GeV	0.99 ± 0.01
Isolation	$\Delta R(\mu - jet) > 0.5$	0.96 ± 0.02
Cuts common for both muons	All above, per 2μ	0.55 ± 0.04
Additional cuts which only one out of two muons must pass		
Hits in all three layers		0.97 ± 0.03
Fiducial cut	$\int B\, dl > 1.9$ Tm	0.97

Table 4.2: Definitions and efficiencies for the muon identification cuts in the central muon system.

The basic cuts used for the muon identification are summarized in Table 4.2. Three separate cuts were applied to suppress the cosmic ray background. First of all, we reject the tracks and hits which are back-to-back in the $\theta - \phi$ plane (i.e. with both $\Delta\theta$ and $\Delta\phi$ greater than $170°$). Second, the tracks which cross octant boundaries (see sec. 3.5) are discarded because they can not come from the interaction vertex. Finally, we require the three-dimensional impact parameter, d_{3D} (i.e. the closest distance from the muon track to the interaction vertex) to be less than 22 cm, which ensures the consistency of the track with the vertex and aids significantly in cosmic rejection. These cuts were studied and optimized by analyzing single muon and cosmic ray tracks with $p^{\mu} > 7$ GeV/c.

Several quality criteria are used to ensure that only good tracks are kept. We require at least two out of three muon layers to have hits consistent with the track. Among these two layers the innermost A-layer is always required to be hit. The absence of hits in one of the outer layers is usually due to the "holes" in the muon system coverage, and such events were "verified" by eye-scanning of the events.

The standard muon reconstruction code of DØRECO returns a special flag, $IFW4$, which contains information on the "goodness" of the track fit. Several parameters, like the χ^2 of the fit in both the bend and the non-bend views, are used to set this flag. If the track fails a certain requirement, DØRECO adds 1 to the value of $IFW4$. Thus the flag is equal to 0 for "golden" muons; all muon candidates with $IFW4 > 2$ are discarded by the reconstruction program. We further tightened this cut and accepted only the muons with $IFW4 \leq 1$. Such a cut reduces number of fake muons significantly.

Finally, we require a matching track for the muon in the CD, and a minimum ionizing particle (MIP) energy deposit in the calorimeter along the muon track. Furthermore, we accept only muons isolated from jets with $E_T^j > 10$ GeV ($\Delta R_{\mu j} > 0.5$) to reject secondary muons from decaying hadrons in jets. This cut also reduces the background from muons faked by jets due to the energy leakage into the muon system in the areas with a low amount of the calorimeter material.

The cuts discussed above are combined to define the *loose muon* selection criterion. Both muons of reaction (4.2) must pass the loose cuts. In addition we require two cuts which only one of the muons must satisfy. The first of these is the requirement of a three-layer track. The second one is a fiducial volume cut which improves the momentum reconstruction of the muon. We require one of the muons to traverse a field integral $\int B\,dl > 1.9$ Tm. These two additional cuts are applied independently, so different muons of the pair may satisfy each of them. It was checked using $Z \rightarrow \mu\mu$ data that the loose selection criteria efficiencies are not correlated with these two extra requirements. The momentum resolution for the low $\int B\,dl$ region ($\int B\,dl < 1.9$ Tm) was studied in detail and parameterized by the following formula:

$$\left(\frac{\sigma(\frac{1}{p_\mu})}{\frac{1}{p_\mu}}\right)^2 = 0.18^2 + (0.0175 \cdot p_\mu[\mathrm{GeV}/c])^2, \qquad (4.6)$$

which should be compared with (3.6) for high $\int B\,dl$ muons. Such a degraded resolution in the low $\int B\,dl$ region does not affect the cross sections calculated with the DØBAUR Monte Carlo program within the systematic uncertainty of the calculations (see sec. 3.7).

The overall efficiency of the identification of a pair of muons passing tight selection criteria was calculated using the $Z \rightarrow \mu\mu$ samples from data and from the DØGEANT Monte-Carlo. It was found to be:

$$\varepsilon_{CF}^{\mu\mu} = 0.54 \pm 0.04. \qquad (4.7)$$

4.2 Selection of $p\bar{p} \to ee\gamma$ Events

Now, after discussing the particle identification, we will address the actual algorithms used in the selection of the events of reaction (4.1). Beyond the standard electron and photon quality cuts we introduce additional kinematical and fiducial requirements for the final state particles:

$$
\begin{gathered}
|\eta_{det}^{e/\gamma}| \leq 1.1 \text{ or } 1.5 \leq |\eta_{det}^{e/\gamma}| \leq 2.5; \\
p_T^e > 25 \text{ GeV/c}, \quad p_T^\gamma > 10 \text{ GeV/c}; \\
\Delta R_{e^\pm\gamma} > 0.7.
\end{gathered}
\tag{4.8}
$$

Here and in what follows η_{det} is the pseudorapidity of an object in the detector frame with a vertex at $z = 0$ (in the center of the detector). It coincides with the physical pseudorapidity, η, when the vertex of the interaction also has $z = 0$. We use η_{det} for the acceptance cuts because they are determined by the geometry of the detector. We also reject events which have an electron or photon in the region of $1.1 < |\eta_{det}| < 1.5$ where the amount of the EM calorimetry material is small (see sec. 3.3) and the EM energy measurement is not reliable. The upper limit for the electron or photon pseudorapidity of 2.5 is motivated by a large amount of the material in front of the FDC (see sec. 3.4.4) beyond this pseudorapidity threshold and by the large particle flux in the very forward region which diminishes the tracking efficiency. Furthermore, the conversion probability for such a forward photon is very high (see Fig. 4.2), as is the random track overlap probability.

Finally, the transverse momentum cuts for the electrons were chosen based on the optimization of the signal to background for the $Z \to ee$ sample. The transverse momentum cut for the photon is motivated by the efficiency of the H-matrix cut which is not only low but also not well understood for electromagnetic clusters with $E_T < 10$ GeV. Therefore, lowering the photon p_T threshold to a value below 10 GeV/c is very problematic.

Based on the set of cuts listed in (4.8) we choose the ELE_2_MAX Level 2 trigger for the selection of reaction (4.1) candidates. This trigger corresponds to the EM_2_MED Level 1 trigger, which requires transverse energy depositions greater than 7 GeV in at least two trigger towers of the EM calorimeter. The Level 2 trigger further requires two electromagnetic clusters with the transverse energy greater than 20 GeV which pass certain isolation and quality cuts. Neither trigger was prescaled during run Ia. The integrated luminosity for the ELE_2_MAX trigger (after correction for bad and special runs) is $13.9 \pm 1.7\ \mathrm{pb}^{-1}$ (see sec. 3.6.7 for details of the luminosity calculations). The efficiency of the trigger for the offline cuts of $p_T > 25$ GeV/c for two electrons was calculated using the $Z \to ee$ event sample. It was found to be:

$$\varepsilon_{L1+L2} = 0.98 \pm 0.01. \tag{4.9}$$

The efficiency of the fiducial (η) cuts (or the acceptance) depends on the actual pseudorapidity distribution of the photons and electrons. It was calculated by the DØBAUR Monte-Carlo program (see sec. 3.7). For the SM case the fiducial cuts are 53% efficient. This efficiency is slightly higher for the non-zero anomalous couplings because the pseudorapidity distribution of the final state particles is more central in this case (the DØBAUR Monte Carlo describes the efficiency increase correctly). The overall efficiency and cross section for the reaction (4.1) within the set of cuts (4.8) for the SM case are:

$$\varepsilon_{SM} = 0.20 \pm 0.02; \tag{4.10}$$

$$\sigma_{SM} \cdot \varepsilon_{SM} = 0.225 \pm 0.025 \text{ pb.} \tag{4.11}$$

We started the event selection from the standard $Z \to ee$ sample with very loose cuts imposed. The sample was selected from the so-called RGE offline stream which contains all events which pass at least one of a large number of different offline filters. (The RGE acronym stands for "Really Good Events".) This data stream basically contains all the events interesting to different physics groups doing a broad spectrum of analyses. The $Z \to ee$ sample was selected by a standard W/Z-finder package [114] which requires at least two electromagnetic clusters with uncorrected transverse energy (E_T^{uncor}) greater than 15 GeV which pass some cluster quality cuts, significantly looser than the set listed in Table 4.1. The additional offline energy corrections are less than 10%, so the $E_T^{uncor} > 15$ GeV requirement is guaranteed to be less stringent than the $E_T > 17$ GeV cut. Since only two clusters are required to pass the E_T cut, the photon transverse energy is unrestricted if we require both electrons to have $E_T > 17$ GeV. However, we superimpose a loose cut on the third electromagnetic cluster ($E_T > 5$ GeV) in order to get rid of soft and fake photons (in practice, low-energy electromagnetic clusters found by the reconstruction program). We also require at least one of the clusters to belong to PELC bank and to have a track match significance $< 10\sigma$. The starting sample after these (very loose) requirements consists of 77 events.

Cut description	No. of survived events
Starting sample	77
$\chi^2 < 100$ (CC), 200 (EC)	25
EM fraction > 0.90	25
ISO < 0.10	21
Fiducial cuts	15
μ-blanking	13
$p_T^e > 25$ GeV/c	10
ELE_2_MAX trigger	10
$\Delta R_{min}^{e\gamma} > 0.7$	8
$p_T^\gamma > 10$ GeV/c	4

Table 4.3: Number of $ee\gamma$ candidates passing different selection criteria.

After applying the H-matrix cuts (see Table 4.3), the sample is reduced to 25 events. All events pass the EM-fraction cut; 4 events fail the ISO < 0.10 cut on the electron/photon isolation. Thus, after particle identification requirements on all three final state particles we get only 21 events in the sample. Another 6 events fail the fiducial cuts (4.8); 2 events have a microblanking bit set, which means that they were taken during the Main Ring activity, and are thus unreliable (see sec. 3.6.2). After requiring both electrons to pass the $p_T > 25$ GeV/c requirement, we end up with 10 events. All of them pass the Level 2 trigger requirements; 2 events fail the separation cut. Among the remaining 8 events, 4 have a photon with transverse energy below 10 GeV (see Table 4.3).

The final sample consists of 4 events; 3 of them have two "tight" electrons, and one has one "tight" and one "loose" electron, which is exactly what one would expect from the DØ tracking efficiency (see sec. 4.1.1). The "loose" electron for that one event (58796/247, see Table. 4.4) does not have an associated track and thus belongs to the PPHO class. However, there is no ambiguity in associating one of the two PPHO banks with the electron. Eye-scanning of the event 58796/247 clearly shows a trace of hits in the CDC (see sec. 3.4.3) along the line from the vertex to one of the PPHO clusters. There are no

Particle	Type	p_T	η	ϕ	N_j/E_T^j	$\not\!\!E_T$	$M_{ee\gamma}$	M_{ee}	$\Delta R_{e\gamma}$
Run/Event: 58486/212									
e_1	tight	53.8	−1.86	6.03	1/26.9	5.5	159.5	92.8	2.96
e_2	tight	43.7	−1.85	2.30					3.51
γ		12.2	0.76	4.65					
Run/Event: 58796/247									
e_1	tight	29.3	−0.20	2.91	0	6.3	90.5	67.5	1.13
e_2	loose	36.0	0.47	0.14					2.64
γ		18.1	−0.54	3.99					
Run/Event: 63120/16499									
e_1	tight	28.3	1.82	1.34	0	4.4	90.0	74.9	2.40
e_2	tight	26.5	0.13	4.08					1.73
γ		11.5	0.26	5.81					
Run/Event: 64425/1906									
e_1	tight	35.2	−0.63	3.86	0	7.3	86.4	73.0	2.31
e_2	tight	30.3	0.36	0.41					1.28
γ		12.2	0.06	1.66					

Table 4.4: Parameters of the final $p\bar{p} \to Z\gamma \to ee\gamma$ candidates. Unit for masses is GeV/c^2; for transverse momenta — GeV/c; for E_T and $\not\!\!E_T$ — GeV.

associated hits along the line to the other PPHO cluster. Moreover, the real photon is close to the "tight" electron in the event as one would expect for a decay event, while the "loose" electron is almost back-to-back with the tight electron. The $\not{E}_T$ in all four candidates is very small, as one would expect for $ee\gamma$ events. Only one out of four events has a jet with transverse energy above 7 GeV, which is in agreement with the k-factor of 1.34 (see sec. 2.3.4).

The parameters of the four observed candidates are listed in Table 4.4. Transverse energy of the photon, masses of the ee-pair and $ee\gamma$ system, as well as the minimum separation for the candidate events are shown in Fig. 4.4. The SM predictions obtained from the Monte Carlo with fast detector simulation are shown in the same plots as histograms. It is clear from the table and from the plots that three events can be naturally associated with the decay mechanism, while one event with high invariant mass of the $Z\gamma$ system is a production event. The $ee\gamma$ invariant mass for this event is somewhat higher than one would expect from SM, but with such a limited number of candidates such a difference is not statistically significant. The anomalously large ΔR in the same event can be explained by the presence of a hadronic jet in the event, which boosts the whole $Z\gamma$ system.

The display of the production event, produced with the standard DØ event viewer, PIXIE [115], is shown in Figs. 4.5 and 4.6. The top plot in the first figure is an $r - z$-view of the event, integrated and the folded over ϕ. Two EM clusters corresponding to electrons are in the North EC (left side of the figure). The tracks pointing toward these clusters are clearly seen in the North FDC. They point to the vertex (small cross on the z-axis) which

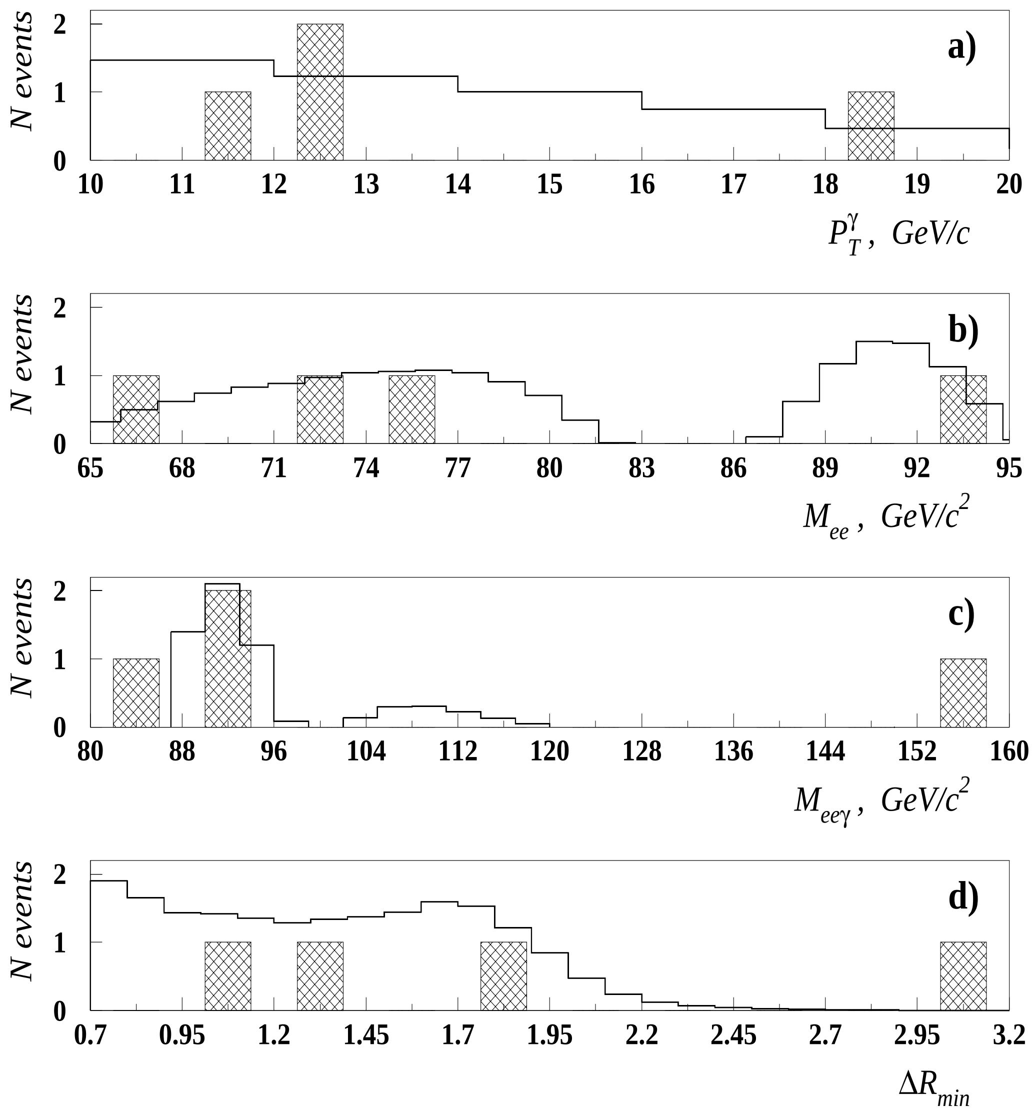

Figure 4.4: Comparison of the parameters of the observed $p\bar{p} \to Z\gamma \to ee\gamma$ candidates and the SM predictions: a) transverse momentum of the photon; b) invariant mass of the electron pair; c) mass of the $ee\gamma$ system; d) minimum separation between the photon and electrons. Hatched bars — observed events; histograms — SM predictions (arbitrary units). The x-axis labels show the bin size for the data points.

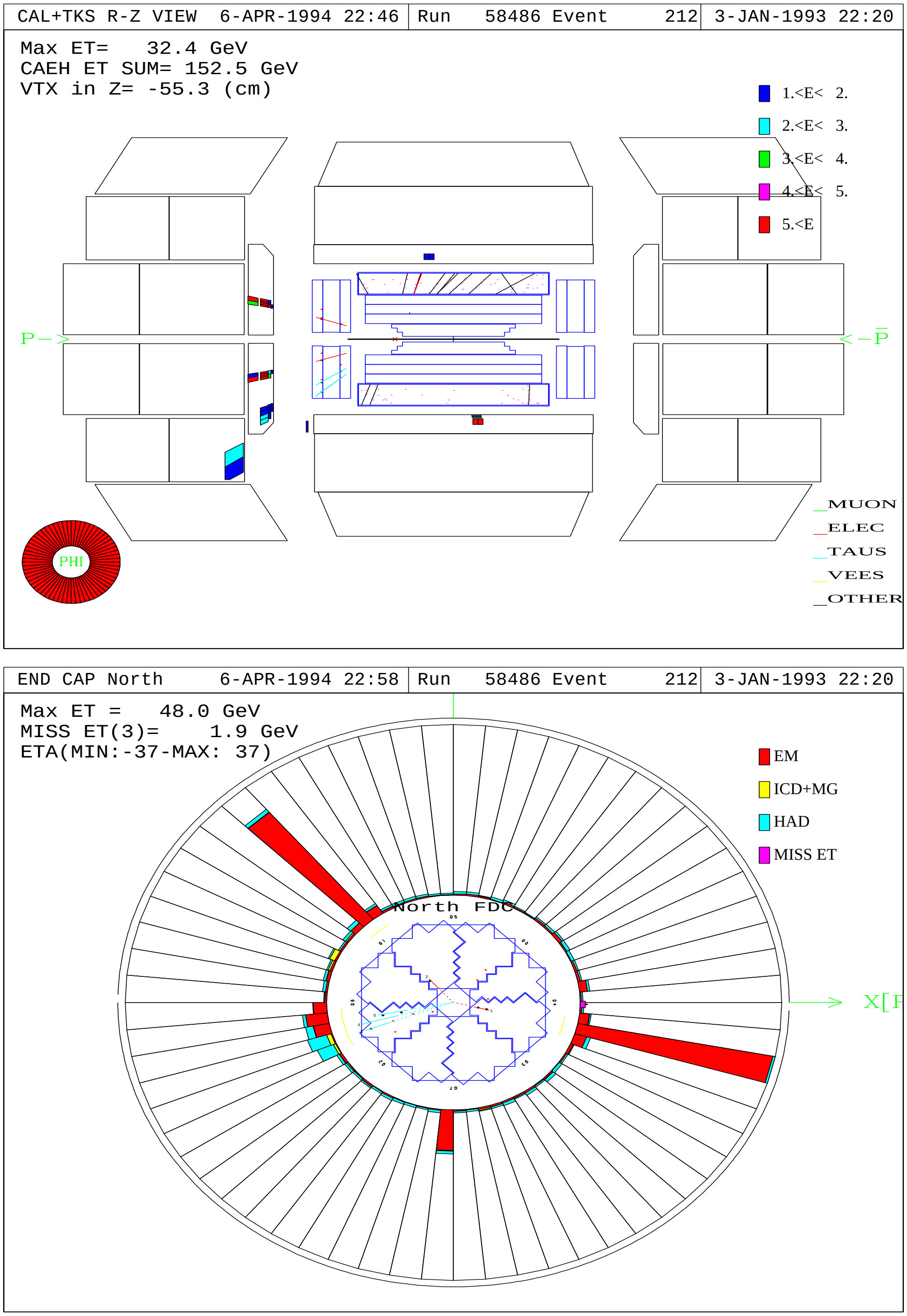

Figure 4.5: Event display of the production $ee\gamma$ candidate. See text.

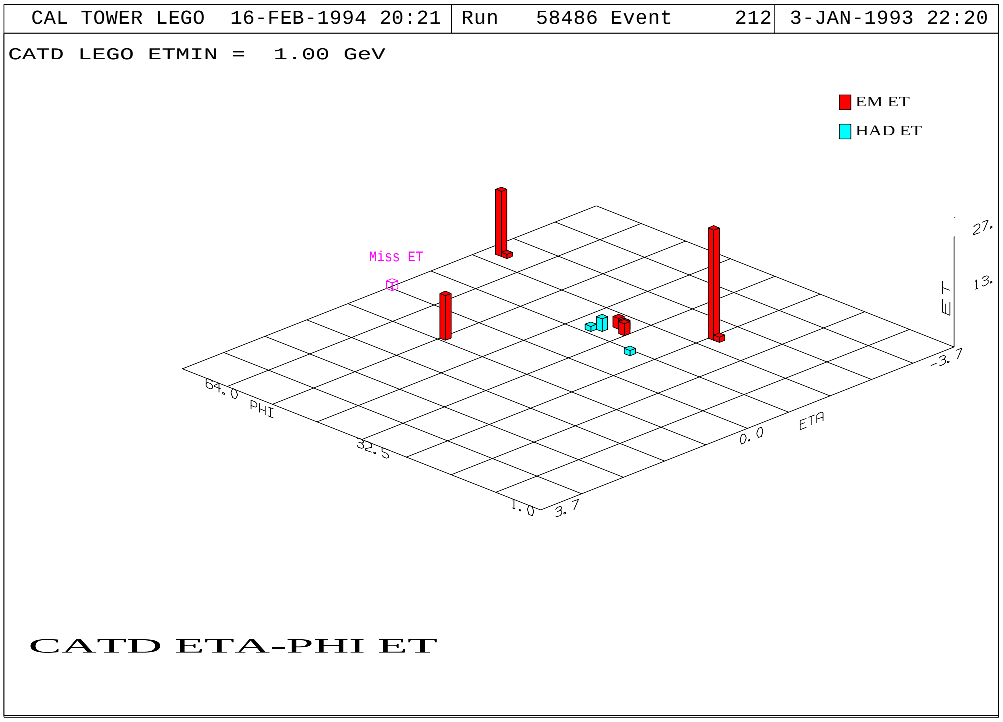

Figure 4.6: Event display of the production $ee\gamma$ candidate (cont'd).

is located just outside the vertex chamber of the detector. The photon is located in the CC (EM cluster in the lower half of the picture). There are no tracks or hits along the line from the vertex to the photon EM cluster. The event also has a jet which can be seen in the lower left part of the picture. It is contained in the forward calorimeter and also deposits some energy in the ICD (see sec. 3.3.6). The bottom plot in Fig. 4.5 shows the end-view of the detector integrated over η_{det} from -3.7 to $+3.7$. The lengths of the filled bars in the calorimeter display of a given event are proportional to the energy depositions. PIXIE displays uncorrected energies; more precise values can be found in Table 4.4. Two electrons with matching FDC tracks are represented by the long bars. The photon is shown as a small bar in the bottom of the plot. The jet is shown as a cluster of filled and hatched bars and a bunch of tracks in the FDC. Finally, the LEGO plot in Fig. 4.6 shows the topology of the event in the $\eta - \phi$ phase space. The vertical scale of the LEGO plot in this figure is proportional to the transverse energy measured in the calorimeter towers. All three electromagnetic clusters are well separated, which is typical for a production event.

4.3 Selection of $p\bar{p} \to \mu\mu\gamma$ Events

The following set of kinematical and fiducial cuts was used for selection of the reaction (4.2):

$$\begin{gathered} |\eta^{\gamma}_{det}| \leq 1.1 \text{ or } 1.5 \leq |\eta^{\gamma}_{det}| \leq 2.5; \\ |\eta^{\mu^{\pm}}_{det}| \leq 1.0; \quad \Delta R_{\mu^{\pm}\gamma} > 0.7; \\ p_T^{\mu_1} > 15 \text{ GeV}/c, \quad p_T^{\mu_2} > 8 \text{ GeV}/c, \quad p_T^{\gamma} > 10 \text{ GeV}/c. \end{gathered} \tag{4.12}$$

The photon selection cuts are the same as for the $ee\gamma$ case (see sec. 4.2). The acceptance cut for the muons coincide with the η-region covered by the CF (see sec. 3.5). It should be mentioned that the requirement of $\int B\,dl > 1.9$ Tm for one out of two muons essentially squeezes the available $|\eta|$ range for this muon to ≈ 0.8, so we will consider the $\int B\,dl$ cut as a fiducial cut. Different requirements on the momenta of the two muons originate from the fact that the muon momentum resolution (3.6) is modest (see sec. 3.5), and it is even worse for the muon which does not pass the $\int B\,dl > 1.9$ Tm cut (see sec. 4.1.3, Eq. (4.6)). Being asymmetric in p_μ, such a degraded resolution results in a long lower p_μ tail for the reconstructed muon momenta. Furthermore, for radiative Z decays (see sec. 2.3.2) which are expected to dominate for this set of cuts, the momentum of the muon which radiates the photon in the final state will be on average smaller than that for the other muon. Note that the $p_T^\mu > 15$ GeV/c cut is only about one sigma away from the average muon transverse momentum in the Z-decay, which is ≈ 40 GeV/c. This difference in the p_T^μ cuts was properly taken into account by the Monte Carlo calculations of the theoretical cross section (see sec. 3.7).

The so-called "top trigger" (MU_EM) was used for the selection of the candidate sample. This trigger requires one muon with $p_T^\mu > 5$ GeV/c and one electromagnetic cluster with $E_T > 7$ GeV at the Level 2 trigger. By design this trigger requires the muon to be within $|\eta_{det}| < 1.7$ and the electromagnetic tower with $E_T > 7$ GeV (Level 1 trigger). The integrated luminosity collected in run Ia for this trigger is 13.3 ± 1.6 pb^{-1} after correction for bad and special runs (see sec. 3.6.7 for details of the luminosity calculations).

Similar selection criteria applied to the $p\bar{p} \to t\bar{t} \to e\mu + X$ analysis [95, 113] which allowed us to use the very clean sample of 713 events verified by eye-scanning for reconstruction and trigger efficiency studies. This sample contains events with a muon with transverse momentum above 5 GeV/c and an electron/photon with transverse energy above 7 GeV. The efficiency of the single muon trigger was estimated by triggering on the electromagnetic cluster in this sample and counting the number of muon candidates which pass the muon trigger requirements. It was found to be:

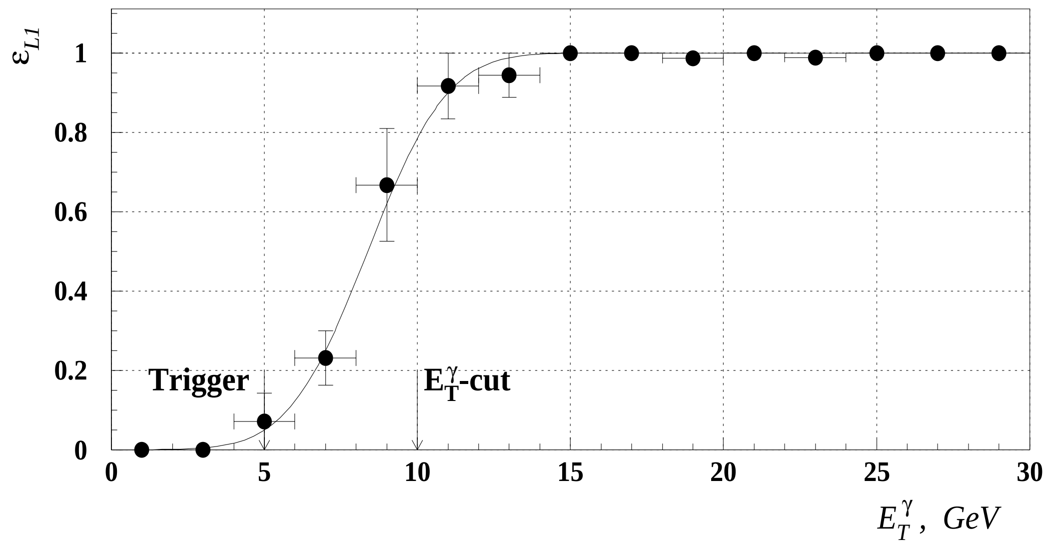

Figure 4.7: Turn-on curve for the Level 1 electromagnetic trigger.

$$\varepsilon_\mu = 0.76 \pm 0.06,$$

independent of muon transverse momentum above 8 GeV/c. This gives the following efficiency for a pair of muons assuming no correlations between muon momenta:

$$\varepsilon^{\mu}_{L1+L2} = \varepsilon_\mu(2 - \varepsilon_\mu) = 0.94^{+0.06}_{-0.09}. \tag{4.13}$$

The efficiency of the photon trigger is governed by the Level 1 trigger turn-on curve shown in Fig. 4.7 [116]. The efficiency is as high as 80% at the p_T^γ offline cutoff (4.12). The trigger is fully efficient for $p_T^\gamma > 14$ GeV/c. The average efficiency for the SM distribution in photon transverse energy is about 97%. The overall p_T^γ-dependent trigger efficiency is taken into account in the Monte-Carlo calculations of the cross section (see sec. 3.7).

The acceptance for the reaction (4.2) was calculated in a similar manner to that for the electron case. For the SM case it is 19%. The overall efficiency and cross section for the reaction (4.2) within the set of cuts (4.12) for the SM case are:

$$\varepsilon_{SM} = 0.064 \pm 0.010; \tag{4.14}$$

$$\sigma_{SM} \cdot \varepsilon_{SM} = 0.184 \pm 0.030 \text{ pb.} \tag{4.15}$$

The whole data set of run Ia was used for event selection. It contains only four non-cosmic events with muons in the CF or EF muon system accompanied by a photon, with all three particles passing the identification and p_T cuts. One out of four events has both muons in the EF system, where the reconstruction efficiency is not yet well understood; furthermore it fails the Level 1 trigger requirements. Another one fails the separation requirement (4.12). The other two events are our final reaction (4.2) candidates. The parameters of these two events are listed in Table 4.5. Both events have no accompanying jets. The muon momentum resolution is quite modest, so the errors on the $M_{\mu\mu}$ and $M_{\mu\mu\gamma}$ are large (of the order of 15 GeV/c^2), and it is challenging to determine if a certain event is due to a production or a decay diagram. However, both events have a low separation between the photon and one of the muons, so most likely they are of the decay type. The large missing transverse energy in these events is most probably due to the poor muon momentum resolution.

The muons in the first event were found to have opposite charges, whereas the muons in the second event have identical charge. However, the efficiency of charge determination is only about 60% for the chosen p_T^{μ} cuts (4.12), so we do not require muons to have the opposite charge.

<table>
<tr><th>Particle</th><th>Type</th><th>p_T</th><th>η</th><th>ϕ</th><th>$\not\!\!E_T$</th><th>$M_{\mu\mu\gamma}$</th><th>$M_{\mu\mu}$</th><th>$\Delta R_{\mu\gamma}$</th></tr>
<tr><td colspan="9">Run/Event: 58970/2551</td></tr>
<tr><td>μ_1</td><td>2-layer</td><td>19.3</td><td>-0.23</td><td>6.05</td><td rowspan="3">19.0</td><td rowspan="3">59.1
(-10.5
$+31.2$)</td><td rowspan="3">44.7
(-9.4
$+26.2$)</td><td>0.93</td></tr>
<tr><td>μ_2</td><td>low $\int B\,dl$</td><td>18.4</td><td>0.96</td><td>2.94</td><td>3.10</td></tr>
<tr><td>γ</td><td></td><td>16.0</td><td>0.70</td><td>6.13</td><td></td></tr>
<tr><td colspan="9">Run/Event: 63629/15585</td></tr>
<tr><td>μ_1</td><td>2-layer</td><td>26.4</td><td>0.14</td><td>2.99</td><td rowspan="3">30.8</td><td rowspan="3">47.0
(-5.9
$+12.7$)</td><td rowspan="3">35.0
(-5.9
$+12.0$)</td><td>0.73</td></tr>
<tr><td>μ_2</td><td>low $\int B\,dl$</td><td>9.4</td><td>-0.83</td><td>5.81</td><td>2.93</td></tr>
<tr><td>γ</td><td></td><td>18.2</td><td>-0.31</td><td>2.41</td><td></td></tr>
</table>

Table 4.5: Parameters of the final $p\bar{p} \to Z\gamma \to \mu\mu\gamma$ candidates. Unit for masses is GeV/c^2; for transverse momenta — GeV/c; for E_T and $\not\!\!E_T$ — GeV.

Run/Event	$p_T^{\mu_1}$, GeV/c	$p_T^{\mu_2}$, GeV/c	$\not\!\!E_T$, GeV	$M_{\mu\mu}$, GeV/c^2	$M_{\mu\mu\gamma}$, GeV/c^2	χ^2/N_{deg}
58970/2551	18.9	36.4	4.1	62.0	80.6	2.9/2
63629/15585	24.8	37.7	2.4	67.8	87.9	11.2/2

Table 4.6: Parameters of the $\mu\mu\gamma$ candidate events after the kinematical fit.

A simple attempt to correct the low masses of both the dimuon and $Z\gamma$ systems due to the long lower tail of the muon momentum resolution (see Eqs. (3.6), (4.6)) was made. The $\mu^+\mu^-\gamma$ production within the chosen set of cuts (4.12) has a low expected background (see sec. 4.5), so it is assumed that both events are due to the reaction (4.2). Therefore, the missing transverse energy in these events should be very close to zero (likewise the $\not\!\!E_T$ for the $e^+e^-\gamma$ channel, see Table 4.4). Thus we perform a kinematical fit of the event parameters, requiring missing transverse energy to be compatible with zero within the errors (3.5). We assume that muon momenta resolution is the major source of the missing transverse energy mismeasurement. The high and low $\int B \cdot dl$ muon momenta were smeared according to the formulas (3.6) and (4.6), respectively. The corrected parameters of the two candidate events after such a "poor man's fit" are given in Table 4.6. The fit has a reasonable χ^2 per degree of freedom and gives the masses of the $Z\gamma$ system much closer to the Z-mass than that before the fit. The fact that the $\mu^+\mu^-\gamma$ mass after the fit is very close to the Z mass is further evidence in favor of the decay type hypothesis for the two candidate events.

The comparison of the event parameters and the SM predictions is shown in Fig. 4.8. For the dimuon mass (b) and the overall mass distribution (c) the data points are shown both before (hatched bars) and after (filled bars) the constrained fit. The former should be compared with the SM predictions with realistic momentum smearing (solid histograms); the latter should be compared with the unsmeared momenta case (dashed histograms).

The event displays of the first candidate are shown in Fig. 4.9 and 4.10. The top plot in the first figure shows the top view of the full DØ detector. There are two muon tracks pointing to the interaction vertex. One (bottom) track has hits in all 3 layers of the CF; the other one has hits only in the two inner layers, and as is clearly seen from the picture, it hits the gap in the outer layer, which explains the absence of the hits in the outer layer. The three layer track has $\int B\, dl = 1.1$ Tm while the two layer track passes the tight $\int B\, dl$ requirement. The second event has a similar topology. The bottom

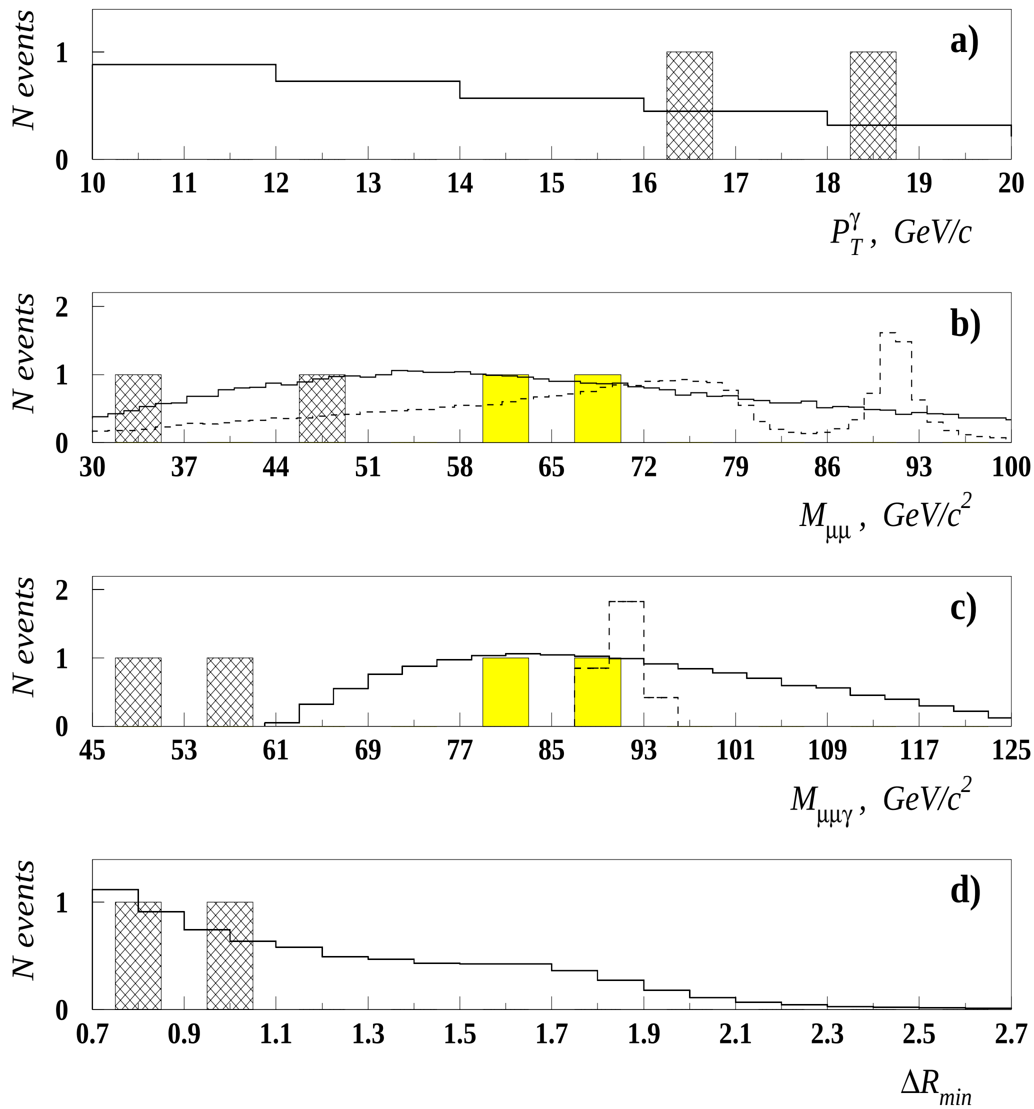

Figure 4.8: Comparison of the parameters of the observed $p\bar{p} \to Z\gamma \to \mu\mu\gamma$ candidates and the SM predictions: a) transverse momentum of the photon; b) invariant mass of the muon pair; c) mass of the $\mu\mu\gamma$ system; d) minimum separation between the photon and muons. Hatched bars — observed events; histograms — SM predictions (arbitrary units). Filled bars — masses after constrained fit which should be compared with the unsmeared distributions shown by the dashed histograms The x-axis labels show the bin size for the data points.

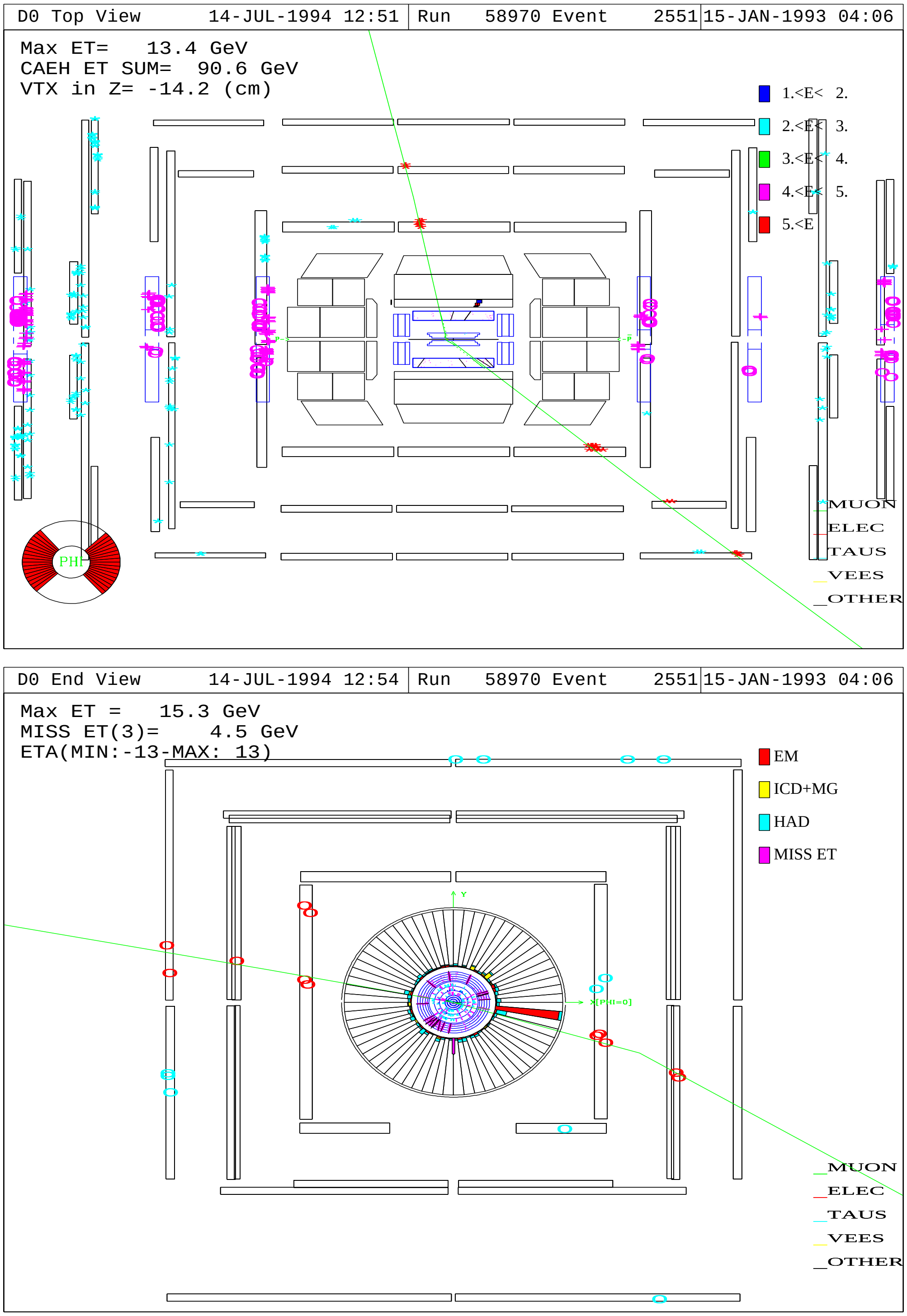

Figure 4.9: Event display of one of the $\mu\mu\gamma$ candidates. See text.

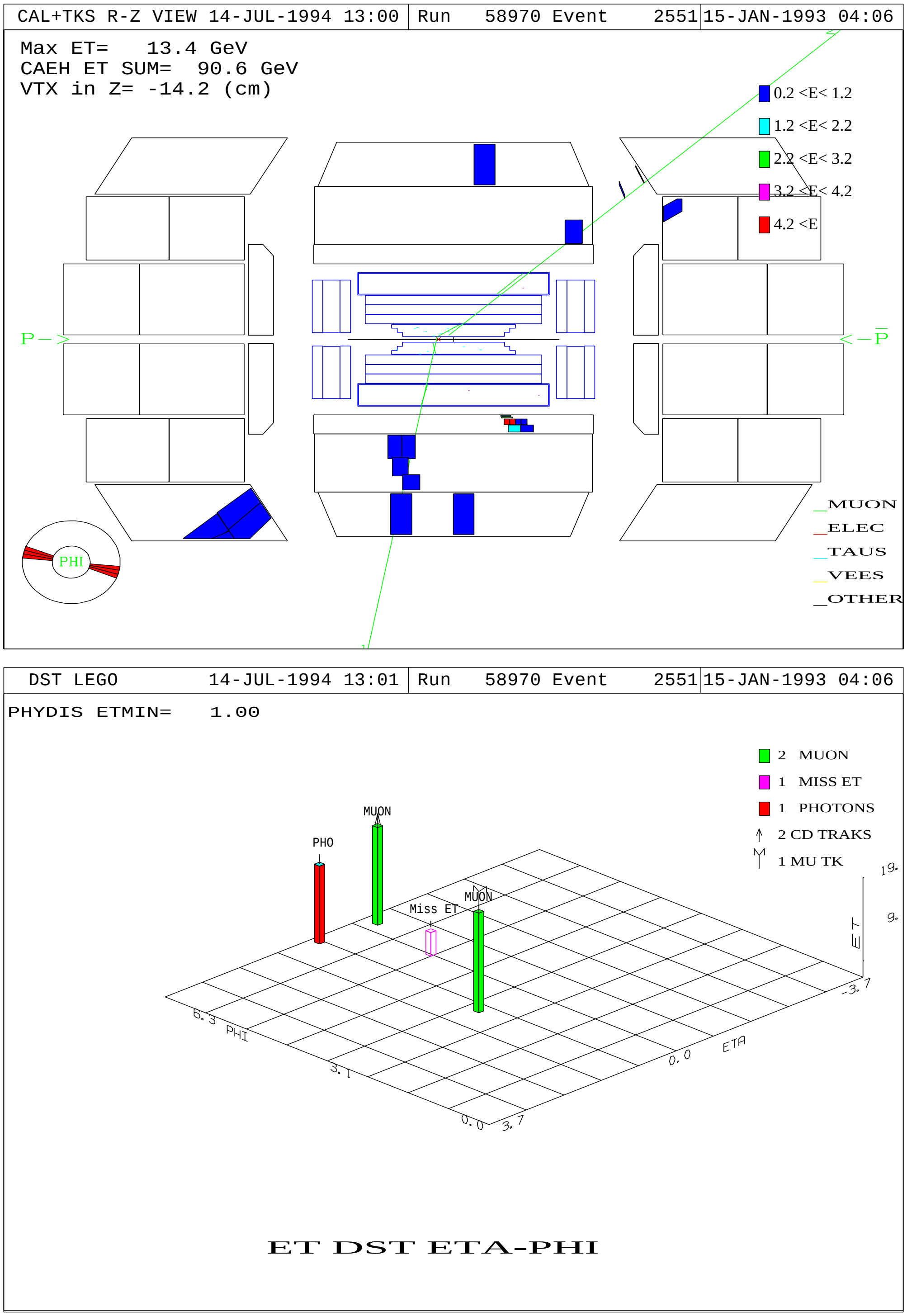

Figure 4.10: Event display of one of the $\mu\mu\gamma$ candidates (cont'd).

plot in the same figure shows the end-view of the detector. A cluster in the electromagnetic calorimeter close in ϕ to one of the muons corresponds to the photon. Both muons and the photon were produced in the same plane in this event, and the $r-z$-view of the corresponding ϕ-slice is shown in the top plot of the second figure. Both the MIP depositions in the calorimeter and the matching tracks in the CDC can be seen for muons. The photon cluster has no close tracks. Finally, the physical $\eta - \phi$ lego-plot is displayed in the bottom of the second figure. It shows the population of the phase space with the final state particles. The photon is clearly close to one of the muons as is expected for decay events (see Fig. 2.7).

4.4 Selection of $p\bar{p} \rightarrow \nu\nu\gamma$ Events

Currently we do not use the neutrino channel for establishing limits on the anomalous couplings or to state an observation of signal, but certain attempts to detect $Z\gamma$ events in this channel were made.

The advantages of the neutrino decay mode of Z were discussed in sec. 2.3.3. The theoretical backgrounds to this channel due to the $Z+jets$ and multijet production are expected to be acceptable for $p_T^\gamma > 30$ GeV/c. Therefore we attempted to select $p\bar{p} \rightarrow \nu\bar{\nu}\gamma$ candidates using the following cuts:

$$p_T^\gamma > 30 \text{ GeV}/c, \quad \not{E}_T > 30 \text{ GeV}, \qquad (4.16)$$
$$|\eta_{det}^\gamma| < 1.1 \text{ or } 1.5 < |\eta_{det}^\gamma| < 2.5.$$

The ELE_MAX Level 2 trigger can be used for selecting these events. This trigger requires an isolated EM-cluster with $E_T > 20$ GeV which passes certain quality cuts which are less stringent than the standard photon identification cuts, and a missing transverse energy in the calorimeter above 20 GeV. This trigger follows the Level 1 EM_1_MAX trigger which requires an EM-cluster with transverse energy above 14 GeV. Both Level 1 and Level 2 triggers were not prescaled during the run Ia. They are used for the $p\bar{p} \to W \to e\bar{\nu}$ analysis.

However, most of the events which pass the selection criteria (4.16) are due to the direct production of W's which subsequently decay into electron-antineutrino pairs: $p\bar{p} \to W \to e\bar{\nu}$, with the electrons being misplaced into the PPHO (photon) banks due to the tracking inefficiency. There are about 9,000 $W \to e\bar{\nu}$ events with a "tight" electron passing the standard electron identification cuts (see sec. 4.1.1), and with $E_T^e > 30$ GeV, $\not{E}_T > 30$ GeV. Taking into account the tracking efficiency of $\approx 87\%$ (see Table 4.1), one would expect about 1500 $W \to e\bar{\nu}$ events with the electron misplaced in the PPHO bank and passing all our cuts. The expected cross section of the reaction (2.9) within the set of cuts is about 0.5 pb (assuming $\approx 60\%$ overall detection efficiency), which corresponds to 7 signal events. In order to make the background at least comparable with the signal one needs an additional rejection of the fake process $W \to e\bar{\nu} \to \gamma\not{E}_T$ by about a factor of 100.

Recent studies show that the main tracking inefficiency in the CDC (see sec. 3.4.3) is due to a poor reconstruction of the z-coordinates of the hits. In the VTX chamber (see sec. 3.4.1) the main reason is a high number of hits, which results in ambiguities in combining them into tracks. The same problem exists for the FDC (see sec. 3.4.4) where the density of tracks is much higher than that in the central region. Therefore, the tracking inefficiency is primarily due to poor track finding, and not because of problems with hit reconstruction. As a part of the work on the neutrino channel candidate selection it was shown that an additional rejection power for electrons of about 15 with a 70% efficiency for photons can be achieved by counting the density of hits in 3-dimensional and 2-dimensional tracking roads. The specialized package, HITSINFO [117], was developed and released as part of DØRECO for this purpose. Utilization of the TRD (see sec. 3.4.2) information should improve this rejection even further.

p_T^γ and $\not{E}_T$ thresholds	Standard selection			With hit-counting		
	N_{SM}	N_{anom}	N_{bck}	N_{SM}	N_{anom}	N_{bck}
30 GeV/c	6.4	28	1340	4.5	20	89
40 GeV/c	3.6	25	203	2.5	18	14
45 GeV/c	2.7	24	45	1.9	17	3

Table 4.7: Expected number of SM (N_{SM}), anomalous ($h_{40}^Z = 0.5$, N_{anom}), and $W \to e\bar{\nu}$ background (N_{bck}) events for the standard e/γ identification criteria and after applying the hit counting electron rejection method.

Utilization of the HITSINFO package does not solve the background problem completely — the background is still higher than the signal. However, for the case of anomalous couplings the cross section is much larger than that for the SM case, especially for large values of p_T^γ. Table 4.7 shows the expected number of signal events for the SM case, for the anomalous coupling $h_{40}^Z = 0.5$ and form factor scale $\Lambda = 500$ GeV (which corresponds to our current 95% confidence level (CL) limit from combined electron and muon channel, see Chapter 5), and the expected $W \to e\bar{\nu}$ background before and after applying the hit counting algorithm. It is clear that for transverse momenta above 45 GeV/c the sensitivity to anomalous couplings is very high, and the anomalous signal is 5 times higher than the expected background. Therefore, the p_T^γ-fit method (see sec. 5.2) with the correct background shape should be capable of setting even better limits on the anomalous couplings in the neutrino channel than those obtained using the charged decay modes of the Z (provided, that no significant excess of high p_T^γ events above the background level is observed, likewise for the electron and muon channels).

Work in this direction is under way, and the hope is that it will be possible to obtain the limits on the anomalous $Z\gamma$ production in the reaction (2.9) in the near future.

4.5 Backgrounds

In this section we describe the main sources of background in the $e^+e^-\gamma$ and $\mu^+\mu^-\gamma$ channels.

4.5.1 QCD Background

The major source of background to $\ell^+\ell^-\gamma$ signal is the QCD background due to $\ell^+\ell^- + jets$ (dominated by $Z + jets$) production with one of the jets faking a photon by fragmenting into a high energy π^0 which subsequently decays into a pair of spatially close photons unresolved in the EM calorimeter.

For the $e^+e^-\gamma$ channel there is an additional background from jets faking electrons. Jets are able to fake electrons by fragmenting into a leading π^0, with the additional track originating either from photon conversion or from soft charged particles accompanying the π^0.

This type of background dominates also for several other processes, e.g. $p\bar{p} \to W\gamma \to \ell\bar{\nu}\gamma$ or direct photon production ($j\gamma$). The quantitative characteristics of this background depend very much on the details of the detector design, jet definition algorithms, etc. For the DØ detector the probability of a jet faking an electron/photon was studied in great detail [118].

Jets Faking Electrons or Photons

The method used for estimating the probability that a jet fakes an electromagnetic cluster is based on measuring the fraction of $n\ jet(s) + \gamma$ events in the $(n+1)$ *jets* sample ($n = 1, 2, ...$). Here γ is a PPHO bank which passes all photon identification criteria (see Table 4.1). This method is based on the assumption that all photons in such a sample are in fact QCD fakes. This is not exactly true because of direct photon production [119]. We will discuss the direct photon contamination in the background sample later.

The initial data set for fake probability studies was collected during the same physics run using several jet triggers. Because of the very high multijet production cross section most of these triggers were prescaled (see sec. 3.6.2) which results in several dips at the trigger thresholds in the E_T^γ spectrum. In order to eliminate this trigger bias we consider only multijet events with the photon which is not a leading particle. We also perform the analysis separately in CC and EC, and restrict the fiducial volume to $|\eta^{\gamma}_{det}| < 1.1$ in CC and $1.5 < |\eta^{\gamma}_{det}| < 2.5$ in EC, which coincides with the fiducial volume used for both the $e^+e^-\gamma$ and $\mu^+\mu^-\gamma$ analyses (see cut definitions (4.8) and (4.12)).

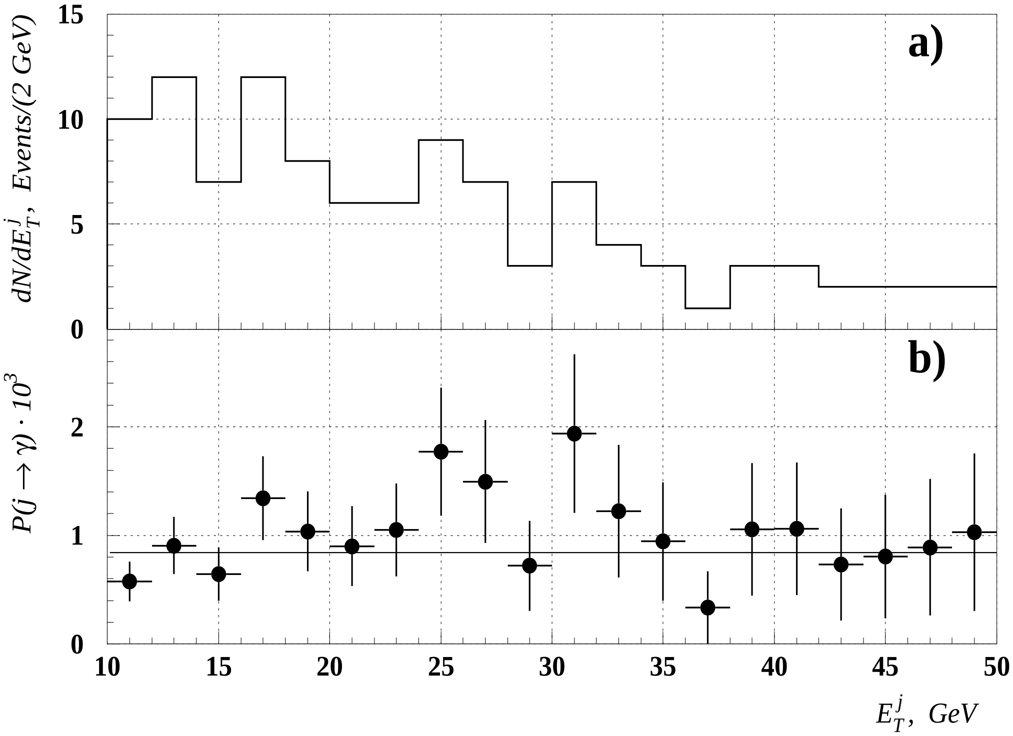

Figure 4.11: a) E_T spectrum of non-leading CC photons in the multijet sample passing standard photon identification and selection cuts; b) jet faking photon probability in the CC as a function of jet/photon transverse energy.

The transverse energy spectrum of the CC photons accompanying jets is shown in Fig. 4.11 (a). The probability of a jet faking a photon is obtained by dividing the E_T spectrum of fake photons by that of the non-leading jets in pure multijet events, and is shown in Fig. 4.11 (b) for the CC. It is well fitted by either a linear or constant function. The same is true for the fake background in the EC. For this analysis we use constant fake probabilities. The uncertainties due to the fit method are included in the total systematics of the background estimates.

The same method was used for obtaining the probabilities for a jet faking a "tight" or a "loose" (i.e. passing "loose" electron/photon cuts, and failing at least one of the "tight" electron cuts, see sec. 4.1.1) electron (in what follows e_t and e_ℓ, respectively) with transverse momenta above 25 GeV/c in the central and end calorimeters. The fake probabilities are summarized in Table 4.8. The fourth column of the table shows the fake probabilities averaged over the detector using the observed ratio of the CC/EC jets (3/1). The systematic uncertainties of these probabilities are dominated by the low statistics of the fake jets and are of the order of 15%. The probability to fake any electron is given by the sum of the probabilities to fake a "tight" and a "loose" electron, as shown in the bottom row of the table.

Faking	CC	EC	Average	Direct γ corrected
$j \to \gamma$	0.84 ± 0.08	0.90 ± 0.11	0.86 ± 0.09	0.65 ± 0.18
$j \to e_t$	0.62 ± 0.07	1.5 ± 0.2	0.84 ± 0.10	0.84 ± 0.10
$j \to e_\ell$	1.7 ± 0.1	1.6 ± 0.2	1.7 ± 0.1	1.5 ± 0.2
$j \to e$	2.3 ± 0.1	3.1 ± 0.3	2.5 ± 0.1	2.3 ± 0.2

Table 4.8: Probabilities (in units of 10^{-3}) for a jet to fake a photon or electron in the DØ detector.

The last column of the table represents a rough way to take into account the direct photon contamination in the multijet sample used for the analysis.

Recent DØ results on direct photon cross section [119] show that the fraction of direct photons passing the photon selection cuts used in this analysis in the p_T^γ range of 10 to 50 GeV/c (where most of the background is concentrated) is $25 \pm 25\%$. The large (systematic) error is due to the big uncertainty on the direct photon cross section, especially in the low p_T^γ region. The probability of a direct photon to fake a PELC (electron) bank is negligible at our level of accuracy because such a photon must either convert before the tracking chambers or be quite close to a random track in the central detector. The probability in both cases is of the order of 10%. Thus, accounting for the direct photon contamination decreases the probability for a jet to fake a photon (by $25 \pm 25\%$) or a "loose" electron ($13 \pm 13\%$). The correction is less for the "loose" electrons since only about half of them are found in PPHO (photon) banks. The fake probabilities after the direct photon corrections are listed in the last column of Table 4.8.

QCD Background in the Electron Channel

Now we are ready to estimate the QCD background in the electron channel. It is important to estimate this background from the data, because this ensures that all possible sources of the background, including double and triple jet fakes are weighted with the correct factors in the estimate.

It is convenient to break the background into three parts and treat them independently. The first background originates from $e^+e^- + jets$ (dominated by $Z + jets$) with one of the jets faking a photon with transverse momentum above 10 GeV/c. Using real $e^+e^- + jets$ data and multiplying the number of jets by

$P(j \to \gamma)$ (see Table 4.8) is the most precise way of estimating this contribution to the background, since the real $e^+e^- + jets$ sample already contains possible contamination from multijet events with two jets faking electrons. The sample used for the estimation of this background contains one "tight" and another, "tight" or "loose," electron with transverse energy above 25 GeV each. Both electrons are required to pass the standard electron selection criteria (see sec. 4.1.1 and 4.2). We also required a separation $\Delta R_{ej} > 0.7$ between the jet and both of the electrons, in the same way we required the electron-photon separation for the signal. There are 225 CC ($|\eta_{det}| < 1.1$) and 79 EC ($1.5 < |\eta_{det}| < 2.5$) jets with $E_T^j > 10$ GeV in this sample. Multiplying the number of the jets by $P(j \to \gamma)$ from Table 4.8 (the last column) we obtain the following number of events for the first component of the QCD background: $N_1^B = 0.20 \pm 0.05$.

The second and the third components of the QCD background are due to jets faking electrons. In order to calculate these backgrounds we use the $e_t + \gamma + jets$ and $e_\ell + \gamma + jets$ events. The requirement on the electron (photon) is to pass the standard tight or loose identification criteria and a transverse energy cut of 25 (10) GeV. In addition, the photon must have separations $\Delta R_{\gamma j}, \Delta R_{\gamma e} > 0.7$ from the electron and the jet. These two samples contain the $e^+e^- + jets$ events with one electron being misidentified as a photon and also the multijet background with two jets faking an electron and photon. (Because of the low transverse energy cut on the photon, the samples are dominated by the mixture of $Z + jets$ and Drell-Yan e^+e^- pairs with associated jet production)

Selection of these events is quite different from that for the signal events, because one can not use the parent $Z \to ee$ sample due to a low E_T cut on one of the electromagnetic clusters. Thus, we had to reprocess about 75% of run Ia statistics with the requirement of the ELE_HIGH trigger (one electromagnetic cluster with E_T above 20 GeV at the Level 2 trigger) in order to select the $e_{t/\ell}+\gamma+jets$ events. The normalization factor taking into account the different trigger and the fact that only a part of the run Ia statistics was processed, is 1.21. It was calculated by comparing the number of the e^+e^-+jets events with $E_T^e > 25$ GeV in the standard $Z \to ee$ sample and in the background sample. The number of CC (EC) jets with $E_T^j > 25$ GeV observed in the background sample for $e_t+\gamma+jets$ topology is 54 (26); for $e_\ell+\gamma+jets$ topology, 59 (27). The fiducial volume used for counting jets in CC/EC is the same as that for the first component of the background.

At this point extra caution is necessary because simple multiplication of the number of jets by faking probabilities and the normalization factor would result in a double-counting of the multijet background with all three electromagnetic objects being jet fakes, since this background was already estimated as a part of the N_1^B. Although the effect of double counting is small, it was decided to subtract the multijet component from the background samples. This can be achieved by comparing the number of events in the $e_t+\gamma+jets$ and the $e_\ell+\gamma+jets$ samples using the "loose/tight" electron ratio given by equation (4.4) and the probabilities for faking "loose"/"tight" electrons. A simple calculation shows that the numbers of the multijet fakes in the background samples with the jet in CC/EC are 8/6 for the $e_t+\gamma+jets$

topology, and 26/12 for the $e_\ell + \gamma + jets$ topology. Therefore, we base our background calculations on 46/20 (33/15) $e_t+\gamma+jets$ ($e_\ell+\gamma+jets$) events with jets in CC/EC. Multiplication of these numbers by the normalization factor and $P(j \to e_{t/l})$ gives the following number of the background events of the second and third components of the QCD background: $N_2^B + N_3^B = 0.23 \pm 0.03$ events. (This number should be compared with 0.31 ± 0.03 events without subtraction of the multijet fraction from the background samples, which proves that the double-counting does not change results significantly).

The total QCD background in the $e^+e^-\gamma$ channel is:

$$N^e_{QCD} = N_1^B + N_2^B + N_3^B = 0.43 \pm 0.06. \tag{4.17}$$

The p_T spectrum of the background was obtained by combining the p_T spectrum of jets contributing to the first component of the background and the p_T spectra of photons in the events contributing to the second and third components of the background. The subtraction of the double-counted multijet contribution was done simply by scaling the p_T^γ spectra. Since the effect of such a subtraction translates into only one standard deviation of the total background, this approximation is sufficiently accurate. The p_T^γ spectrum of the QCD background is shown in Fig. 4.12 (a). The enhancement at ≈ 50 GeV/c is due to the Jacobian peak [120] in the transverse energy spectrum of the electrons with a missing track in the $Z + jets \to ee + jets \to e\gamma + jets$ events. This spectrum was fitted by the sum of an exponential function $C \cdot e^{-(\alpha p_T + \beta p_T^2)}$ describing rapidly falling jet E_T spectrum, and a Gaussian (to approximately account for the bump at 50 GeV/c).

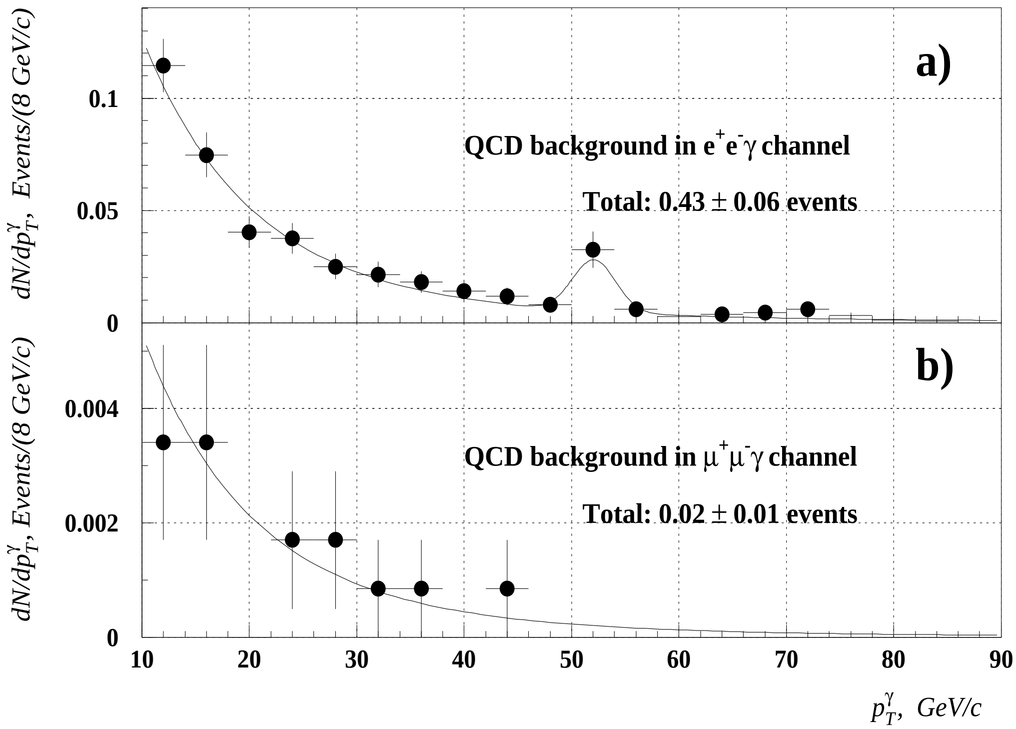

Figure 4.12: a) QCD background in the $e^+e^-\gamma$ channel. The bump around 50 GeV/c is due to the Jacobian peak from the $Z + jets$ production with a jet faking an electron and one of the electrons from the Z-decay being misidentified as a photon. b) QCD background in the $\mu^+\mu^-\gamma$ channel. For fit definitions see text.

QCD/Cosmic Background in the Muon Channel

The QCD background calculation in the muon channel is much simpler since the probability for jets to fake a pair of muons is negligible. Such a fake in principle can occur for b-jets, but the requirement of muons well isolated from jets (see sec. 4.1.3) together with the transverse momentum cut (4.12) suppresses this type of fakes to zero.

The estimation of the QCD background is based on the $\mu^+\mu^- + jets$ sample with muons passing the standard selection cuts (see sec. 4.1.3 and 4.3). We also require a separation of $\Delta R_{\mu j} > 0.7$ between the jet and either of muons, similar to the photon-muon separation requirement for the signal. This sample includes Drell-Yan with associated jet production, $Z + jets$, and cosmic background events. Therefore, the estimation of the background from the data automatically takes into account the background from cosmic rays overlapping with multijet events. (This background is already small because of the muon quality cuts.) The other type of cosmic background with the muon radiating a high energy photon in the detector material (external *bremsstrahlung*) is negligible [121] due to the requirement of a large separation ($\Delta R_{\mu\gamma} > 0.7$) between the photon and both muons.

The background sample was selected using a single muon trigger which requires a 15 GeV/c muon at Level 2. The prescale factor for this trigger, if compared with the trigger used for the signal selection (see sec. 4.3) was calculated to be 1.3$\pm$0.3. The number of jets with a transverse energy above 10 GeV in the CC ($|\eta_{det}| < 1.1$) and EC ($1.5 < |\eta_{det}| < 2.5$) is 8 and 7, respectively. Multiplication of these numbers by the prescale factor and $P(j \to \gamma)$ (Table 4.8, last column) gives the following number of QCD/cosmic background events:

$$N^{\mu}_{QCD} = 0.02 \pm 0.01. \tag{4.18}$$

The p_T spectrum of the background is shown in Fig. 4.12 (b). It was fitted with the function $C \cdot e^{-(\alpha p_T + \beta p_T^2)}$. Due to poor background statistics we used the values of α, β obtained for the electron channel.

4.5.2 $Z \to \tau\tau$ Background

Another source of "background" to $p\bar{p} \to Z\gamma \to \ell^+\ell^-\gamma$ is a cascade decay of Z into neutrinos and a dimuon or dielectron pair through the τ-lepton channel: $Z \to \tau^+\tau^- \to \nu_\tau\nu_\ell\bar{\nu}_\tau\bar{\nu}_\ell\ell^+\ell^-$. Although such cascade decay events are not really background events, they are still not included in the DØBAUR Monte Carlo, so one must make sure that the contribution of the cascade decays is taken into account when comparing the theoretical and experimental cross sections and deriving limits.

From the branching ratio for the $\tau \to \ell\bar{\nu}_\ell\nu_\tau$ decay (0.178 ± 0.003 [9]), the fraction of such decays is $3.2 \pm 0.1\%$. It is further reduced by the p_T cuts on the final state leptons. The exact fraction of τ-events was calculated by comparing the number of events passing the lepton selection cuts in the $Z \to \ell^+\ell^-$ and $Z \to \tau^+\tau^- \to \nu_\tau\nu_\ell\bar{\nu}_\tau\bar{\nu}_\ell\ell^+\ell^-$ samples generated using the ISAJET Monte Carlo [104] and the DØGEANT detector simulation program [103]. It was shown that the expected fractions of the cascade τ-decay events in the e and μ signal samples are:

$$f_e = (0.10 \pm 0.05)\%; \quad f_\mu = (1.4 \pm 0.5)\%, \tag{4.19}$$

where the error is dominated by the systematic error due to the different E_T spectra of leptons in the $p\bar{p} \to Z \to \ell\ell$ decays and in the $p\bar{p} \to Z\gamma \to \ell\ell\gamma$ reactions. This background can be safely neglected for the electron channel.

4.6 Signal

Using the observed number of events in each channel and the background estimates (4.17), (4.18), (4.19), we obtain the following expectations for the number of signal events in the $e^+e^-\gamma$, $\mu^+\mu^-\gamma$ and $\ell^+\ell^-\gamma$ channels:

$$S_{ee\gamma} = 3.57^{+3.15}_{-1.91} \pm 0.06; \tag{4.20}$$

$$S_{\mu\mu\gamma} = 1.95^{+2.62}_{-1.29} \pm 0.01; \tag{4.21}$$

$$S_{\ell\ell\gamma} = 5.52^{+3.56}_{-2.37} \pm 0.06. \tag{4.22}$$

Here the first error is a symmetric conservative 68% CL error, based on Poisson statistics [122] (see sec. 5.1 for more details on the error definitions), and the second one is the systematic error of the background estimate.

These formulas represent the most important result of this work — the first observation of $Z\gamma$ production in hadron collisions[1].

The SM predicts the following number of events (calculations are done with the DØBAUR generator, see sec. 3.7, and formulas (4.11), (4.15)):

$$S^{SM}_{ee\gamma} = 3.2 \pm 0.3 \pm 0.4; \tag{4.23}$$

$$S^{SM}_{\mu\mu\gamma} = 2.5 \pm 0.4 \pm 0.3; \tag{4.24}$$

$$S^{SM}_{\ell\ell\gamma} = 5.6 \pm 0.7 \pm 0.7. \tag{4.25}$$

Here the first error is due to the MC systematics (see sec. 3.7) and the second one is due to the 12% luminosity uncertainty. The SM predictions are in

[1] Recently the CDF Collaboration also observed 8 $Z\gamma$ events [5] in the 1992–1993 data.

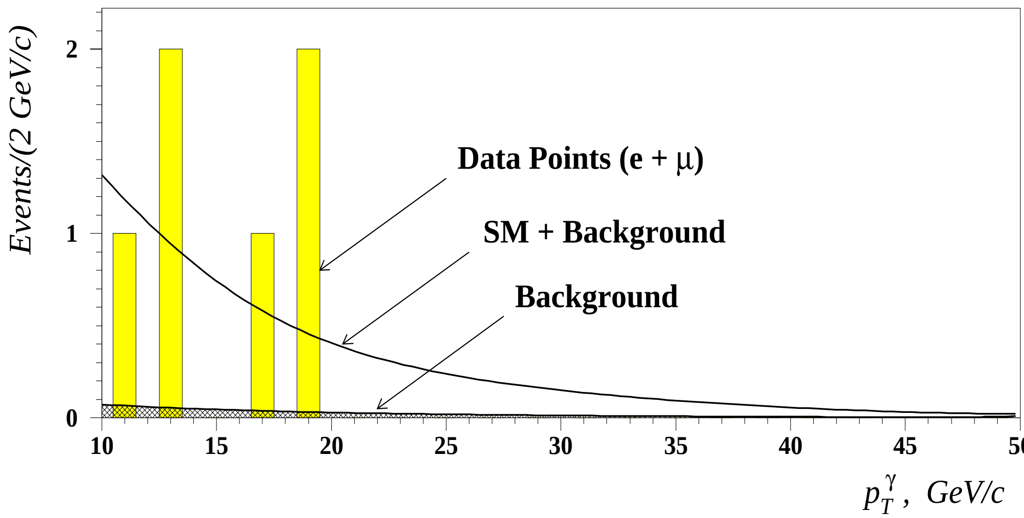

Figure 4.13: Comparison of the observed p_T^γ spectrum of the combined $ee\gamma$ and $\mu\mu\gamma$ signal and the SM predictions. Shadowed bars show data points; hatched curve represents overall background; solid curve shows sum of the SM predictions and background.

good agreement with the observed signal. There is no evidence for anomalous couplings which result in an increase of the expected number of events (see sec. 2.3.2).

The combined p_T^γ spectrum of the $e^+e^-\gamma$ and $\mu^+\mu^-\gamma$ events is shown in Fig. 4.13. The background and the SM prediction are shown in the same plot. The total background is about 6%. Again, the data are in good agreement with the SM expectation and there is no evidence for production of high-p_T^γ events typical of anomalous couplings (see sec. 2.3.2).

Chapter 5

Limits on the Anomalous Couplings

Now, from apex to base, the volume of the Great Pyramid in cubic inches is approximately $161,000,000,000$. *How many human souls, then, have lived on the earth from Adam to the present day? Somewhere between* $153,000,000,000$ *and* $171,900,000,000$.

P. Smith, "Our Inheritance in the Great Pyramid"

In this Chapter we are going to derive the limits on the anomalous couplings based on the observed 4 $ee\gamma$ and 2 $\mu\mu\gamma$ events and the estimated background of 0.5 events. Several different methods for obtaining these limits will be discussed: a fit of the total cross section, and a binned and unbinned likelihood fit of the p_T^γ distribution. The dependence of these limits on the form factor scale Λ and the correlation between different anomalous couplings will be studied. The comparison of our limits with the recent results from the CDF [5] and L3 [6] collaborations and with indirect limits obtained in low energy experiments (see sec. 2.4) is given in Chapter 6.

5.1 Limits From Total Cross Section Measurements

As mentioned in sec. 2.3.2, it follows from the form of the $ZV\gamma$ vertex functions (2.3), (2.4) that the anomalous coupling contributions to the total or differential cross sections of the $q\bar{q} \to \ell^+\ell^-\gamma$ processes are quadratic in h_{i0}^V.

The eight possible $ZV\gamma$ couplings can be naturally combined into four different pairs: the CP-conserving (h_{30}^Z, h_{40}^Z), (h_{30}^γ, h_{40}^γ), and the CP-violating (h_{10}^Z, h_{20}^Z), (h_{10}^γ, h_{20}^γ) couplings. Couplings with different CP-parity do not interfere with each other, so there are no cross-terms in the bilinear form which are proportional to the product of a CP-conserving and a CP-violating coupling. There is a small interference between $ZZ\gamma$ and $Z\gamma\gamma$ couplings with the same CP-transformation property. The most significant interference occurs between the two couplings of a pair, e.g. between h_{30}^Z and h_{40}^Z (see [20]). So, we will study the behavior of the anomalous cross section as a function of two (out of eight) possible couplings. In most cases these two couplings will belong to the same pair.

The total cross section of the reaction (2.7) as a function of two couplings, h_a and h_b, can be expressed in the following form:

$$\sigma(h_a, h_b) = \sigma_{SM} + a_0 h_a + a_1 h_b + b_0 h_a^2 + b_1 h_a h_b + b_2 h_b^2. \tag{5.1}$$

Here, σ_{SM} is the SM cross section, and a_i, b_i are some coefficients.

An upper limit on the cross section of the reaction (2.7) at the confidence level (CL) α from the experimentally observed number of the events can be

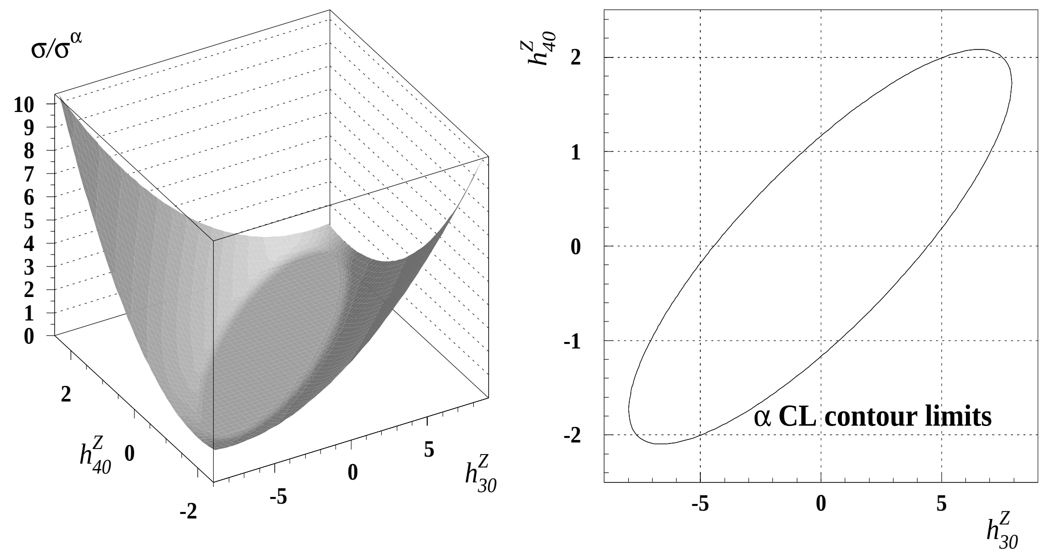

Figure 5.1: Obtaining limits on a pair of couplings from the total cross section measurements. Left plot: ratio of the calculated anomalous cross section (σ) and the α CL upper limit on the cross section from the experiment (σ^α) as a function of the anomalous couplings h^Z_{30} and h^Z_{40}. The contour limit on the pair of couplings is obtained by cutting the σ/σ^α surface at $z = \sigma/\sigma^\alpha = 1$ (a shadowed oval in the left figure). Right plot: projection of the 3D-plot on the (h^Z_{30}, h^Z_{40}) plane.

immediately translated into an α CL limits for the pair of couplings h_a, h_b by solving the following equation:

$$\sigma(h^\alpha_a, h^\alpha_b) = \sigma^\alpha. \tag{5.2}$$

Here the index α denotes the upper limit at the CL of α. The curve defined by equation (5.2) is an ellipse in the (h_a, h_b)-plane (see Fig. 5.1). Therefore, a simple counting of the number of $\ell^+\ell^-\gamma$ events produced in $p\bar{p}$ collisions is sufficient for setting limits on the anomalous couplings. It is important that these limits are defined by a *finite* area in (h_a, h_b)-plane, unlike the indirect limits of low-energy experiments (see sec. 2.4).

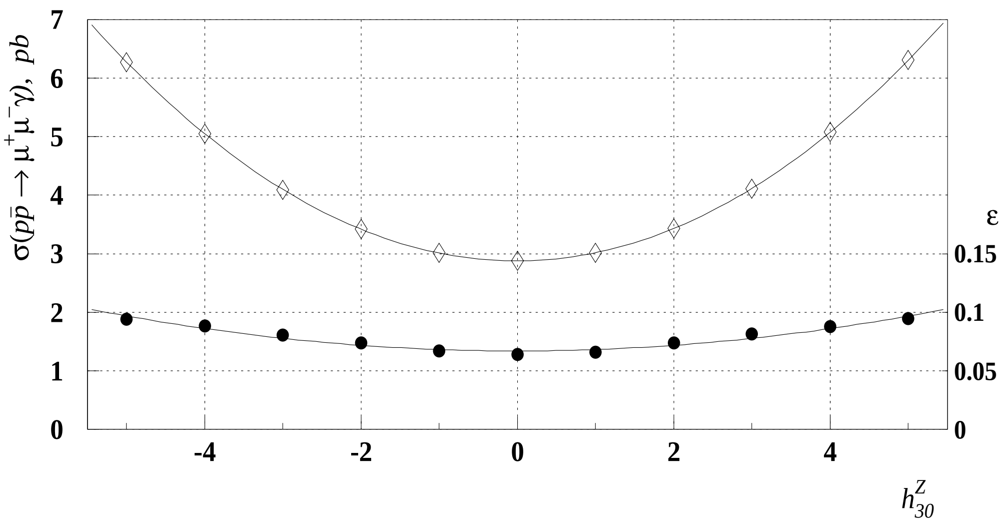

Figure 5.2: The theoretical cross section of the $p\bar{p} \rightarrow \mu^+\mu^-\gamma$ reaction (open diamonds) and the overall detection efficiency (solid dots) as functions of the h_{30}^Z coupling. The systematic error on the efficiency is not shown. Solid lines represent fits with a simple bilinear function.

In practice the observed cross section of the reactions (4.1) and (4.2) might have a more complicated dependence on the anomalous couplings than the bilinear form (5.1) because the detection efficiency generally depends on the actual coupling values. In our case, however, this effect is small. This is illustrated by Fig. 5.2 which shows the calculated cross section and the overall efficiency as functions of the h_{30}^Z coupling for the muon channel. The open diamonds show the theoretical cross section for the case when only the p_T^μ, p_T^γ and ΔR cuts of the set (4.12) are applied. Shown by the solid dots in the same figure is the overall efficiency which includes acceptance, smearing effects, trigger, and particle identification efficiencies corresponding to the full set of cuts (4.12). This efficiency was calculated using the DØBAUR Monte Carlo program with a comprehensive DØ detector simulation (see sec. 3.7). It is clear from the figure that the variation of the detection efficiency is less than that of the cross section, so it can be neglected to first order. Moreover, the efficiency as a function of the coupling constant can be parameterized by a simple quadratic function; if two couplings are varied at a time it becomes a quadratic form in the couplings, similar to (5.1). Therefore, the observed cross section, which is a product of the cross section within the kinematical cuts (p_T^μ, p_T^γ, and ΔR cuts) and the overall efficiency, can still be described by the bilinear form (5.1) if one neglects cubic and quartic terms in the coupling constants. The variation of the efficiency within the DØ 95% CL limits on the couplings (see sec. 5.2) is only about 15% for the muon channel, so it is comparable with the systematic errors on the efficiency (see sec. 4.3). The major source of the efficiency increase is the production of more central muons in the case of anomalous couplings (see sec. 2.3.2), which increases the acceptance because of the stringent cut on the muon pseudorapidity (4.12). For the electron channel variation of the efficiency is less pronounced because of the less stringent cut on the electron pseudorapidity (see cut definitions given by Eqs. (4.8), (4.12)).

Indeed, the total cross section (which is an output of the DØBAUR Monte Carlo program with the detector simulation) as a function of two couplings can be well fitted by the function (5.1). This fact allows us to determine the parameters $\mathcal{P} = \{a_0, a_1, b_0, b_1, b_2\}$ with a relatively small amount of CPU time, and then simply calculate the cross section for arbitrary values of the couplings using equation (5.1). We used a 3×3 grid in the (h_a, h_b)-plane, centered at the SM value of $(0, 0)$ in order to estimate the set $\mathcal{P}$ for different pairs of couplings. This is a standard overconstrained problem which can be effectively solved by a minimal squares method. The size of the grid in each case was chosen to be slightly larger than the expected 95% CL limits on the corresponding pair of couplings, so the cross section as a function of h_a, h_b (required for solving the equation (5.2)) was obtained by an *interpolation*, rather than *extrapolation*, which improves the accuracy of the results. The error of such a parameterization was estimated by calculating the cross section at random points inside the grid and then comparing these cross sections with the calculated values (5.1). The error on the approximation is less than 2%, which is negligible if compared to the overall systematic error of the cross section calculations (see sec. 3.7).

The total cross section within the cuts was parameterized independently for the electron and muon channels, which allows for a calculation of the limits for each channel separately, as well as the combined limits. In order to get the actual 68% and 95% CL limits on the anomalous couplings one has to calculate the corresponding limits on the total cross section ($\sigma^{(68\%)}$ and $\sigma^{(95\%)}$) using the observed number of events and the estimated background (see sec. 4.6). There are two types of errors on the observed signal. The first one is the statistical Poisson error on the number of the observed events, and the second one is the systematic error due to efficiency and background uncertainties. The one-sided α CL errors for a Poisson process with background can be estimated using the

Bayesian approach [122][1]. For instance the α CL upper limit for the signal, S, can be obtained from the following equation [122]:

$$1 - \alpha = \frac{e^{-(S+B)} \cdot \sum_{k=0}^{N} \frac{(S+B)^k}{k!}}{e^{-B} \cdot \sum_{k=0}^{N} \frac{S^k}{k!}}, \tag{5.3}$$

where B is the expected background and N is the observed number of events.

As is well known from statistics (see, e.g. [125]), it is impossible to obtain the precise α CL limit on the signal because of the discrete nature of the Poisson process. However, formula (5.3) gives the best possible *conservative* upper limit. In order to propagate the systematic error into the upper limit we adopted the method recently described in Ref. [126] which is also based on the Bayesian approach. The $\tau\tau$ background (see sec. 4.5.2), which is proportional to the expected signal, was taken into account by scaling the calculated cross sections by $(1 + f_e)$ and $(1 + f_\mu)$ for the electron and muon channels, respectively. Here f_e and f_μ are the background fractions given by Eq. (4.19). Although the effect of these corrections is very small, it was taken into account.

The 68%, 90%, and 95% CL upper limits on the observed signal and cross section are summarized in Table 5.1. The upper limits on the signal (S_{max})

[1]Although the Bayesian approach has several disadvantages and its validity for estimating upper limits for a Poisson process has been debated in the literature for the last decade [122, 123, 124], we still will follow this method, which has been canonized by the Particle Data Group [9]. Most of the authors agree that both classical and Bayesian approaches can be used, and the question of choice belongs more to philosophy than to mathematical statistics (see, e.g. [124]).

Channel	68% CL		90% CL		95% CL	
	S_{max}	$\sigma_{max} \cdot BR$	S_{max}	$\sigma_{max} \cdot BR$	S_{max}	$\sigma_{max} \cdot BR$
$e^+e^-\gamma$	5.34	0.395 pb	7.56	0.576 pb	8.72	0.674 pb
$\mu^+\mu^-\gamma$	3.49	0.271 pb	5.30	0.425 pb	6.28	0.513 pb
Combined	7.52	0.574 pb	10.1	0.799 pb	11.4	0.920 pb

Table 5.1: Upper limits on the signal (S_{max}) and the observed cross section ($\sigma_{max} \cdot BR$) based on electron, muon, and combined data. Only the (Poisson) statistical error is propagated into the upper limit for signal using the method described in Refs. [9, 122]). Both statistical error and systematic uncertainties of the efficiencies and luminosities are propagated into the upper limit of the observed cross section using the method described in Ref. [126].

receive a contribution only from the statistical errors (systematic uncertainties for the background are negligible compared to the Poisson errors). For the upper limit on the observed cross section for a given channel ($\sigma_{max} \cdot BR$) we take into account both the $11\% - 16\%$ systematic error on the efficiency calculations, and the 12% error on the integrated luminosity, and add them quadratically. By propagating the systematic error on the detection efficiency into the upper limit on the experimentally measured cross section, we can treat the parameterized cross section from the DØBAUR Monte Carlo generator as an exact one, and use equation (5.2) to calculate limits on the anomalous couplings.

The resulting limits for pairs (h^Z_{30}, h^Z_{40}) and ($h^\gamma_{30}, h^\gamma_{40}$) calculated for the form factor scale $\Lambda = 500$ GeV (see sec. 2.3.2) are shown in Figs. 5.3, 5.4. We

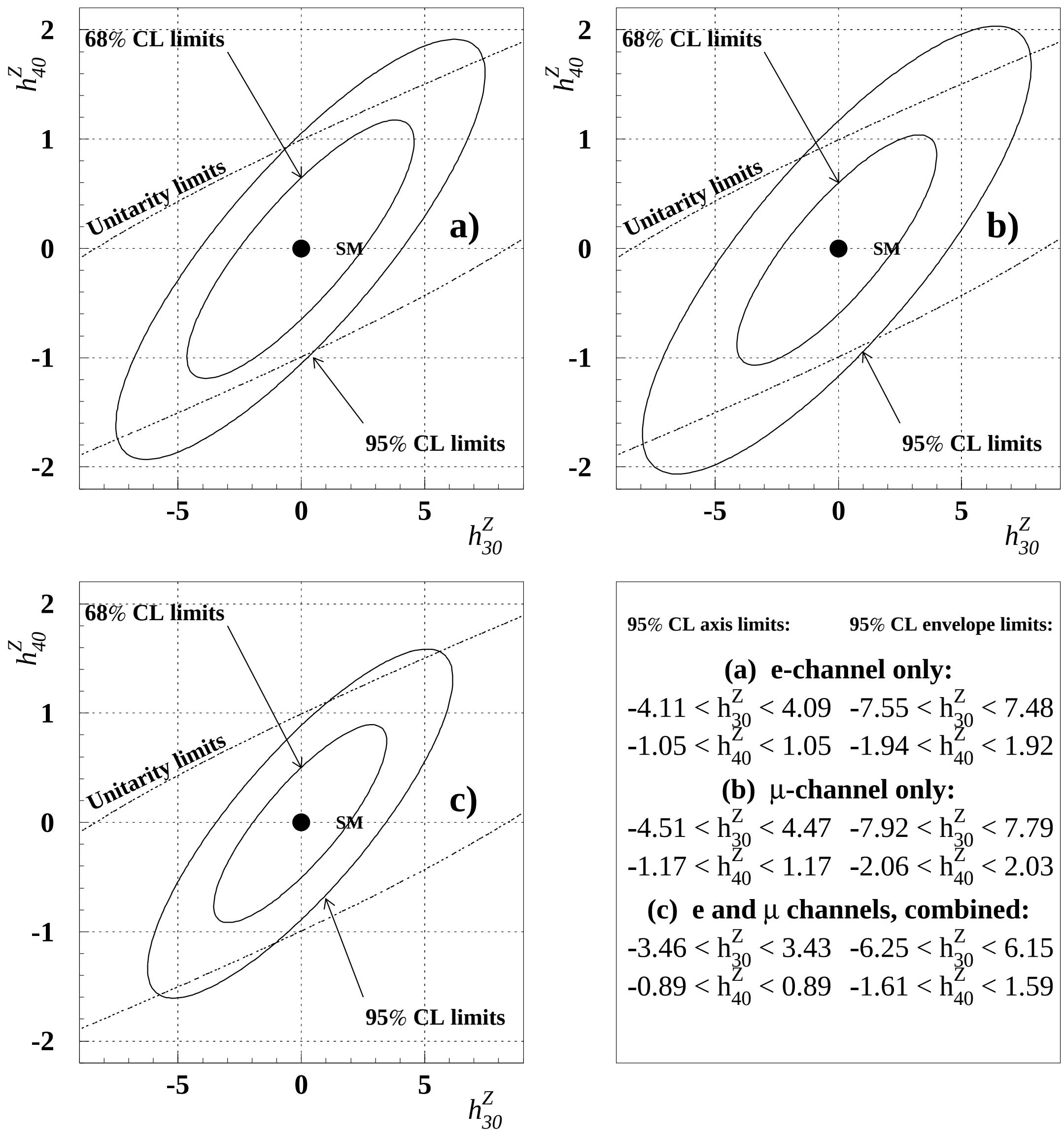

Figure 5.3: Limits on the pair of the anomalous couplings (h_{30}^{Z}, h_{40}^{Z}) from the total cross section fit. Contours represent 68% and 95% CL limits for (a) electron channel; (b) muon channel; (c) both channels combined. Dashed lines show the limits obtained from partial wave unitarity (see sec. 2.3.2) for a form factor scale of $\Lambda = 500$ GeV.

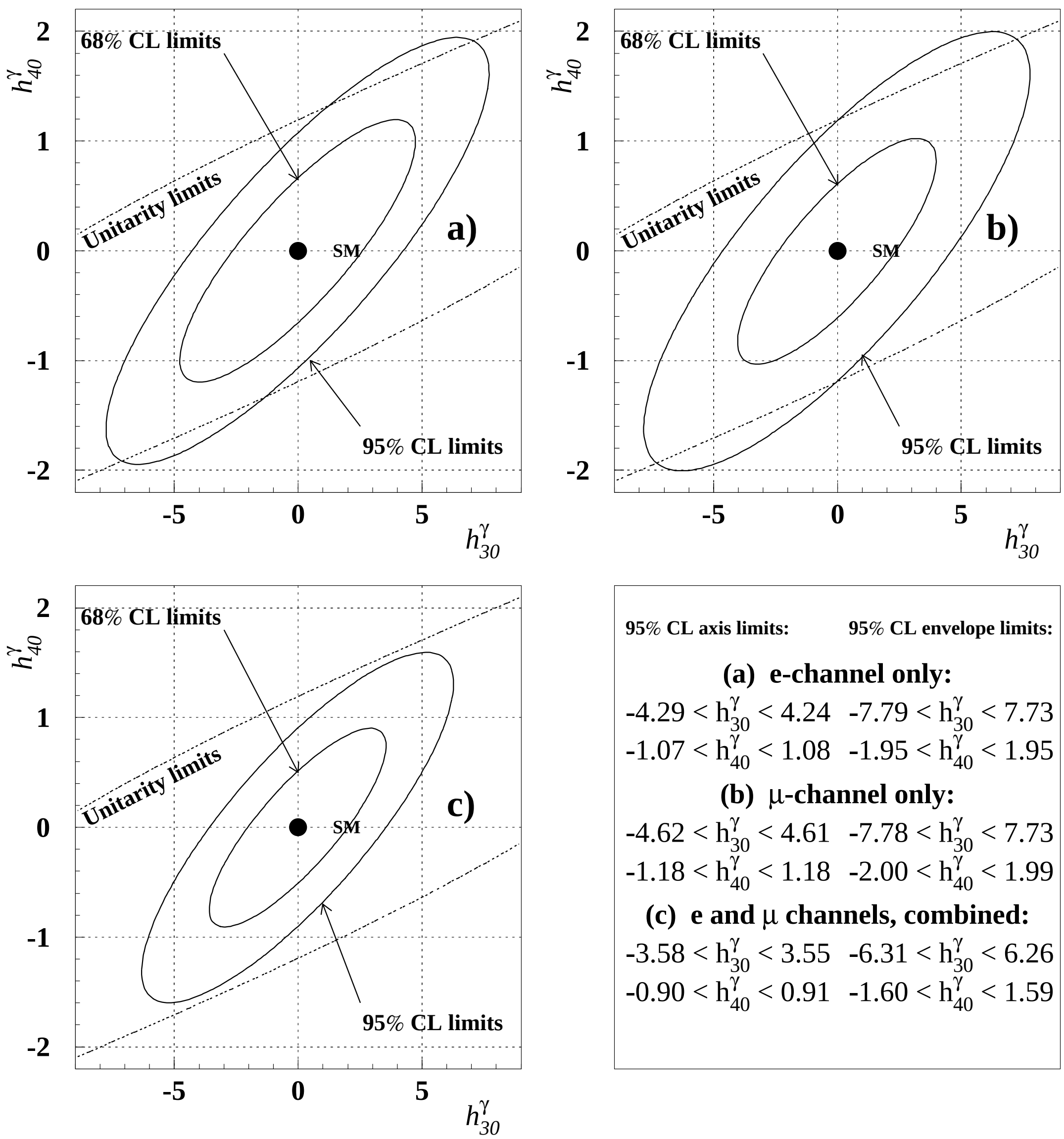

Figure 5.4: Limits on the pair of the anomalous couplings $(h_{30}^{\gamma}, h_{40}^{\gamma})$ from the total cross section fit. Contours represent 68% and 95% CL limits for (a) electron channel; (b) muon channel; (c) both channels combined. Dashed lines show the limits obtained from partial wave unitarity (see sec. 2.3.2) for a form factor scale of $\Lambda = 500$ GeV.

Conditions	Axis limits	Envelope limits
e-channel (h_{30}^Z, h_{40}^Z)	$-4.11 < h_{30}^Z < 4.09$	$-7.55 < h_{30}^Z < 7.48$
	$-1.05 < h_{40}^Z < 1.05$	$-1.94 < h_{40}^Z < 1.92$
μ-channel (h_{30}^Z, h_{40}^Z)	$-4.51 < h_{30}^Z < 4.47$	$-7.92 < h_{30}^Z < 7.79$
	$-1.17 < h_{40}^Z < 1.17$	$-2.06 < h_{40}^Z < 2.03$
e and μ channels (h_{30}^Z, h_{40}^Z)	$-3.46 < h_{30}^Z < 3.43$	$-6.25 < h_{30}^Z < 6.15$
	$-0.89 < h_{40}^Z < 0.89$	$-1.61 < h_{40}^Z < 1.59$
e-channel $(h_{30}^\gamma, h_{40}^\gamma)$	$-4.29 < h_{30}^\gamma < 4.24$	$-7.79 < h_{30}^\gamma < 7.73$
	$-1.07 < h_{40}^\gamma < 1.08$	$-1.95 < h_{40}^\gamma < 1.95$
μ-channel $(h_{30}^\gamma, h_{40}^\gamma)$	$-4.62 < h_{30}^\gamma < 4.61$	$-7.78 < h_{30}^\gamma < 7.73$
	$-1.18 < h_{40}^\gamma < 1.18$	$-2.00 < h_{40}^\gamma < 1.99$
e and μ channels $(h_{30}^\gamma, h_{40}^\gamma)$	$-3.58 < h_{30}^\gamma < 3.55$	$-6.31 < h_{30}^\gamma < 6.26$
	$-0.90 < h_{40}^\gamma < 0.91$	$-1.60 < h_{40}^\gamma < 1.59$

Table 5.2: 95% CL limits on the anomalous couplings from the total cross section fit for a form factor scale of $\Lambda = 500$ GeV.

will use the value of $\Lambda = 500$ GeV as a main choice throughout this Chapter, since such a value is close to our experimental sensitivity (see below and in sec. 5.2.5). The numerical limits shown in these figures are also summarized in Table 5.2. As was mentioned in the beginning of this section, the couplings which belong to the same pair interfere strongly with each other, which result in a significant tilt of the resulting ellipses in Figs. 5.3 and 5.4. To numerically describe this interference we introduce two types of limits. The first type, which will be called the *axis limit*, is the limit on a coupling when the others are fixed at zero. Graphically these limits are given by the intersection points of the α CL contour with the corresponding axis. The other type, the so called *envelope limit*, is the limit on a certain coupling when the other coupling of the same pair is allowed to vary, while the remaining six couplings are fixed at zero. Graphically they correspond to the maximum variation of the coupling inside the α CL contour. The envelope limits are always greater or equal to the axis limits. The closer the envelope limits to the axis limits, the smaller the interference between the corresponding couplings is. It will be shown in sec. 5.2.5 that the envelope limits obtained by varying of a pair of strongly interfering couplings are close to the *global limits*, i.e. the limits on one coupling when all others are allowed to vary.

The 95% CL limits on the anomalous couplings from the total cross-section fit are less stringent than the partial wave unitarity constraints in certain areas of the anomalous couplings phase space. It means that the form factor value of $\Lambda = 500$ GeV is at the limit of the sensitivity of this experiment.

5.2 Limits From Fitting the p_T^γ Spectrum

The advantage of the total cross section method of obtaining limits (see sec. 5.1) is its simplicity. However, limits obtained from the total cross section fit are sensitive to the normalization, i.e. the uncertainty of the integrated luminosity, efficiencies, QCD corrections, and other factors used in the Monte Carlo calculations of the cross section.

A better way of obtaining limits on anomalous couplings is to fit the shape of kinematical distributions which are sensitive to anomalous couplings. The analysis of the shape of distributions is to a large extent independent of the overall normalization, and thus can yield better limits. Furthermore, these limits are generally much tighter than that of the total cross section method, since the shape of a differential distribution is additional information which is ignored by the total cross section method.

The differential cross section which is most sensitive to anomalous couplings is $d\sigma/dp_T^\gamma$. The resolution in the photon transverse energy is very good, so the results are virtually not affected by smearing effects. Besides, it is easy to combine the p_T^γ spectra for different decay channels (unlike, e.g. the $m_{\ell\ell\gamma}$ spectra, which are smeared differently for the electron and muon channels because of the very different lepton resolutions). Furthermore, the p_T^γ spectrum is the only measurable kinematical distribution for the neutrino channel.

The idea of using the differential cross sections in general and the p_T^γ spectrum in particular for obtaining limits on the anomalous tri-boson couplings has been expressed in the very early papers on this subject (e.g. [26, 127]) and was first implemented by the UA2 Collaboration for their $W\gamma$ analysis [15]. We will use a modified binned p_T^γ fit method, as was first described in [128], for obtaining limits. The modification is based on adding an extra bin with no observed events to the p_T^γ histogram, which improves the sensitivity significantly. The limits obtained by this method are compared with those for the unbinned likelihood fit as described in [129]. Since both methods were originally developed during our studies of the $W\gamma$ and $Z\gamma$ couplings, it is worth to describe the main ideas, advantages and drawbacks of both methods, which is done in detail in the following sections.

5.2.1 Unbinned Likelihood Fit

The unbinned likelihood fit method (see, e.g. [130] and references therein) is often used to determine the parameters of resonance peaks or other distributions with well defined mean and dispersion. In this case the unbinned likelihood fit is a way to obtain unbiased and effective estimates of the mean and the dispersion from the data. The main advantage is that the results are not biased by binning of the data, unlike methods which first combine data into a group of bins (a histogram), and then perform the actual fit.

It is possible to use the unbinned likelihood fit to estimate the parameters of a distribution, even if the distribution is not peak-like. The key idea of the unbinned likelihood method is to treat a certain theoretical distribution as a *probability density function* (p.d.f.) and then construct the likelihood function based on the observed data points, assuming that they are distributed according to this probability function. Estimation of any parameters on which the theoretical p.d.f. depends can be further done using the standard maximum likelihood method formalism (see, e.g. [125, 130]).

In our case we start with the predicted $d\sigma/dp_T^\gamma$ spectrum calculated by the Monte Carlo generator (with all kinematical cuts and efficiencies properly taken into account), the estimated background $d\sigma_{bck}/dp_T^\gamma$ distribution, and a certain set of measured $(p_T^\gamma)_i$ points. In order to treat the expected p_T^γ distribution (which is a sum of the predicted signal and background) as a p.d.f. $(f(p_T))$, we need to normalize it to unity within the p_T range (p_T^{min}, p_T^{max}) used for the measurements:

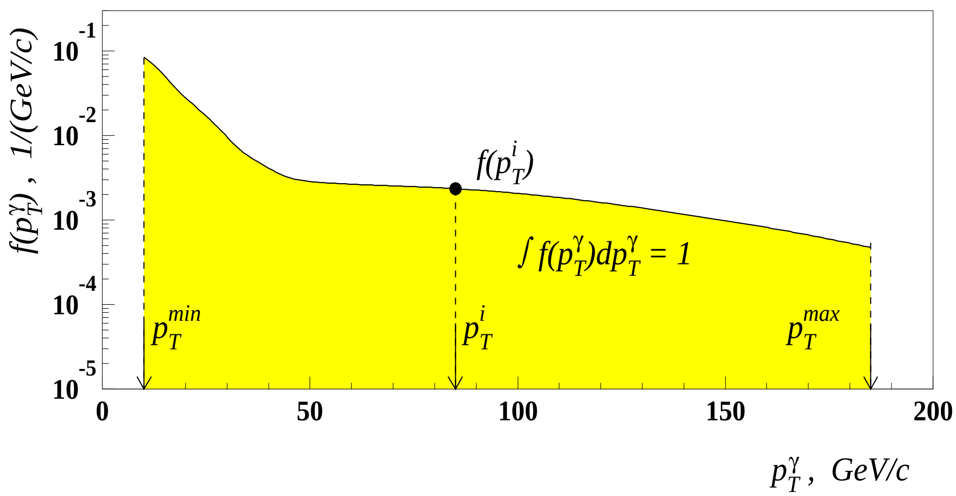

Figure 5.5: The principle of the unbinned likelihood fit.

$$\int_{p_T^{min}}^{p_T^{max}} f(p_T)dp_T = 1, \tag{5.4}$$

which immediately yields

$$f(p_T) = \frac{1}{\sigma_{tot} + \sigma_{bck}} \cdot \left[\frac{d\sigma}{dp_T} + \frac{d\sigma_{bck}}{dp_T}\right],$$

where σ_{tot}, σ_{bck} are the total cross section of the signal and background processes in the p_T range under consideration (see Fig. 5.5). In what follows we will consider the differential cross section as a function of only one pair of couplings, similar to the way used for obtaining limits from the total cross section measurements (see sec. 5.1). The pair of couplings (h_a, h_b) is a set of the parameters we want to determine from the p_T^γ spectrum fit. Therefore, the p.d.f. has the following form:

$$f(p_T|h_a, h_b) \quad = \quad \frac{1}{\sigma_{tot}(h_a, h_b) + \sigma_{bck}(h_a, h_b)} \times \tag{5.5}$$

$$\left[\frac{d\sigma(h_a,h_b)}{dp_T}(p_T)+\frac{d\sigma_{bck}(h_a,h_b)}{dp_T}(p_T)\right].$$

Here the background generally depends on the couplings, since it might have a component proportional to the signal (in our case it is the $\tau\tau$ background, see sec. 4.5.2).

Using this p.d.f., it is straightforward to construct the probability function for observing a certain set of non-correlated points $\{p_T^1, p_T^2, ..., p_T^N\}$ for a given pair (h_a, h_b):

$$P\{p_T^1, ..., p_T^N | h_a, h_b\} = \prod_{i=1}^{N} f(p_T^i | h_a, h_b). \tag{5.6}$$

Therefore, the logarithmic likelihood function of the problem is

$$\begin{aligned} L(h_a,h_b) \equiv \log P = \sum_{i=1}^{N} \log \Bigg[& \frac{1}{\sigma_{tot}(h_a,h_b)+\sigma_{bck}(h_a,h_b)} \times \\ & \left\{\frac{d\sigma(h_a,h_b)}{dp_T}(p_T^i)+\frac{d\sigma_{bck}(h_a,h_b)}{dp_T}(p_T^i)\right\}\Bigg]. \end{aligned} \tag{5.7}$$

The set of parameters $(\tilde{h}_a, \tilde{h}_b)$ which fits the experimental data the best, and their errors can be obtained by maximization of the likelihood function by varying the parameters (h_a, h_b).

The advantage of the unbinned likelihood fit is a clear statistical interpretation of the method, and its total independence from the overall scale of the cross section: the fit is done using the shape only. Moreover, as can be seen from equation (5.7), one even does not need to know the behavior of the function in the whole p_T^γ range. It is sufficient to know the function in the vicinity of the data points, and the total cross section, in order to perform the fit. For instance, if the data points are concentrated at the lower end of the distribution, one does not need to know the precise p_T behavior at the high end — all one needs to know is the total cross section above the last data point. This feature makes it easier to parameterize the $d\sigma/dp_T^\gamma$ distribution (see sec. 5.2.4).

The drawback of this method is the dependence of the results on the smearing of the p_T^i points which could be a significant effect for the case of poor statistics. In principle the smearing effect can be taken into account by performing a large number of maximum likelihood fits with data points being randomly smeared around their central values with known resolution function. However, the interpretation of the α CL limits obtained in a large number of runs is a statistically ill-defined problem. Other drawbacks of this method are the complicated interpretation of the quality of the fit (one can use Kolmogorov-Smirnov statistics for this purpose, see [130] for details), and the absence of any information on the expected and measured total cross section. The best fit might require a total cross section much higher or lower than the measured one with all systematic uncertainties taken into account, and the quality of the fit would still be good. This particular disadvantage, however, can be overcome using the generalized unbinned likelihood fit, described in the next section.

5.2.2 Generalized Unbinned Likelihood Fit

It is easy to generalize the unbinned likelihood method to include the constraint on the total cross section. There are two equivalent ways of introducing an extra term in the likelihood function.

One, which is attributed to E. Fermi (Ref. [131]), is based on the changing of the normalization (5.4) from 1 to the observed number of events N:

$$\int_{p_T^{min}}^{p_T^{max}} f(p_T) dp_T = N.$$

The other approach leads to a logarithmic likelihood function which differs from that within the Fermi's approach by a constant term and has a more straightforward statistical interpretation. The two approaches are equivalent, and we will use the second one, in which the normalization factor is introduced by multiplying the probability function (5.6) by the Poisson probability to observe N events for given integrated luminosity $\mathcal{L} \equiv \int L dt$ (where L is the instantaneous luminosity) and a total cross section $\sigma_{tot}(h_a, h_b) + \sigma_{bck}(h_a, h_b)$:

$$\begin{aligned} P\{p_T^1, ..., p_T^N, N | h_a, h_b, \mathcal{L}\} \;\; = \;\; & \prod_{i=1}^{N} f(p_T^i | h_a, h_b) \times \\ & \frac{\{\mathcal{L}[\sigma_{tot}(h_a, h_b) + \sigma_{bck}(h_a, h_b)]\}^N}{N!} \times \\ & \exp\{-\mathcal{L}[\sigma_{tot}(h_a, h_b) + \sigma_{bck}(h_a, h_b)]\}. \end{aligned}$$

Such a probability function leads to additional terms in the logarithmic likelihood function, if compared with (5.7):

$$\begin{aligned} L(h_a, h_b, \mathcal{L}) \;\; \equiv \;\; & \log P = \sum_{i=1}^{N} \log \left[\frac{1}{\sigma_{tot}(h_a, h_b) + \sigma_{bck}(h_a, h_b)} \cdot \right. \\ & \left. \left\{ \frac{d\sigma(h_a, h_b)}{dp_T}(p_T^i) + \frac{d\sigma_{bck}(h_a, h_b)}{dp_T}(p_T^i) \right\} \right] + \qquad (5.8) \end{aligned}$$

$$N \log\{\mathcal{L}[\sigma_{tot}(h_a, h_b) + \sigma_{bck}(h_a, h_b)]\} -$$
$$\mathcal{L}[\sigma_{tot}(h_a, h_b) + \sigma_{bck}(h_a, h_b)],$$

where we omitted the constant term $(-\log(N!))$.

Now we have more flexibility in obtaining the limits on the anomalous couplings. If the uncertainties in the efficiencies and the error on the integrated luminosity $\mathcal{L}$ are small, one can fix the parameter $\mathcal{L}$ at the measured value and maximize the likelihood function (5.8) with respect to the anomalous couplings h_a, h_b only. However, if the systematic errors on the luminosity and efficiencies are large (as in our case) it is advantageous to use the data itself to normalize $\mathcal{L}(\sigma_{tot} + \sigma_{bck})$ by making $\mathcal{L}$ an extra parameter of the fit. The fit will give the best value of $\mathcal{L}$ with the error on it. If this value obtained from the fit agrees with the measured integrated luminosity within the combined systematic uncertainties of the efficiency calculations and luminosity monitoring, the fit can be considered as reasonably good.

The generalized unbinned likelihood method eliminates one of the drawbacks of the standard unbinned method, described in sec. 5.2.1. However, the limits obtained by the generalized unbinned likelihood fit are still affected by smearing of the data points. One possible way to get rid of this dependence is discussed in the next section.

5.2.3 Binned Likelihood Fit

A simple way to eliminate the dependence of the limits on the data points smearing is to group the data into a set of bins, which are wide enough to dilute the smearing effects. Binning of the experimental data is a well known procedure in experimental high energy physics, and the result of binning is commonly called a histogram.

For large statistics the best estimators of the parameters for a certain distribution do not depend on binning, but for poor statistics this is not the case. Generally the bins should be chosen wide enough to absorb the resolution effects (i.e. the bin width should be much larger than the resolution of the data to be binned). At the same time the number of bins has to be large enough to reflect details in the shape of the data distribution.

Let us consider a general histogram with N_b bins and with n_i events in the i-th bin. For a given distribution $f(p_T) \equiv d\sigma/dp_T + d\sigma_{bck}/dp_T$, the expected number of events in the i-th bin, f_i, is given by the following expression:

$$f_i = \mathcal{L} \cdot \int_{p_T^i}^{p_T^{i+1}} f(x|h_a, h_b)dx,$$

where p_T^i is the lower edge of the i-th bin ($p_T^1 \equiv p_T^{min}$; $p_T^{N_b+1} \equiv p_T^{max}$), and $\mathcal{L}$ is the integrated luminosity. The probability for observing n_i events when f_i events are expected is given by the Poisson probability:

$$P_i = \frac{f_i^{n_i}}{n_i!}\ e^{-f_i}.$$

Therefore, the probability of observing the histogram $\{n_1, n_2, ..., n_{N_b}\}$, assuming uncorrelated bins (which is justified if the bins are chosen to be much wider than the p_T resolution), is given by a simple multiplication of the probabilities P_i:

$$P = \prod_{i=1}^{N_b} \frac{f_i^{n_i}}{n_i!}\ e^{-f_i}.$$

The likelihood function for such a set of bins is

$$L \equiv \log P = \sum_{i=1}^{N_b} (n_i \log f_i - f_i), \tag{5.9}$$

where the constant term $(-\sum \log(n_i!))$ has been omitted. The best set of parameters (h_a, h_b) and their α CL limits can again be obtained by maximizing the likelihood function. As for the generalized unbinned likelihood method, the integrated luminosity can either be fixed at the measured value or can be treated as a free parameter of the fit (see sec. 5.2.2).

At this point the question of obtaining the best possible limits on the pair of the anomalous couplings (h_a, h_b) is reduced to the question of optimum binning of the data. Generally one would like to have at least several events per bin, and since the p_T^γ distribution falls rapidly, one has to increase the bin width for higher p_T^γ. The standard way of binning (e.g. as described in Ref. [20]) suggests having an approximately equal number of events per bin, which results in the last bin being extended from a certain $p_T^{N_b}$ to p_T^{max}. However, this choice neglects the fact that the SM and the anomalous couplings predict events populating very different regions of the p_T phase space.

For the SM case the events are concentrated in the low p_T region; in presence of the anomalous couplings, a large excess of events at high photon transverse momenta is expected (see Fig. 2.5). Therefore, the highest observed p_T carries the essential information about the limits on the anomalous couplings. A simple extension of the last bin up to p_T^{max} ignores the information about the highest transverse momentum in the data — all that one knows after such a binning is that it is higher than $p_T^{N_b}$, which makes such a histogram less sensitive to the anomalous couplings.

In order to exploit the fact that the maximum observed transverse momentum for the SM case should be far below p_T^{max}, it was proposed to require the last bin with the data-driven bin lower edge ($p_T^{N_b}$) to *contain no events* [128]. The $p_T^{N_b}$ should be chosen slightly above the highest observed transverse momentum in the data sample so that the smearing effect could not move the last data point across the boundary of this bin.

Philosophically, the usage of such a data-driven bin is equivalent to representing the results of the experiment as two essentially independent measurements. The first one is a *non-observation* of *any* events above a certain p_T^γ threshold (a null-result experiment), which carries the information on the anomalous couplings. The second one is the *observation* of a certain number of events (a cross section measurement), which mainly carries the information about overall normalization, and can be used to diminish the uncertainties due to systematics of the integrated luminosity and efficiency estimates. This second measurement is equivalent to the introduction of the extra term in the generalized unbinned likelihood method (see sec. 5.2.2).

A mathematical proof of the fact that the described approach with the *posteriori* and not *a priori* chosen binning is indeed unbiased, can be derived from the likelihood formula (5.9). To see this, let us choose an *a priori* binning with the bin width determined only by the resolution in p_T^γ. This approach is completely unbiased by the data. After the experiment is carried out, a certain number of subsequent high-p_T bins will have no events. The contribution of these empty bins to the likelihood function, according to (5.9), is

$$\sum_{i=N_{l+1}}^{N_b} (n_i \log f_i - f_i) = - \sum_{i=N_{l+1}}^{N_b} f_i = - \int_{p_T^{l+1}}^{p_T^{max}} f(x|h_a, h_b),$$

where l is the last bin (with the upper edge at p_T^{l+1}) which contains a non-zero number of events. The additional term does not have any dependence on the number of empty bins ($N_b - N_l$), and depends only on the upper edge of the last data bin. Therefore, one can simply combine all adjacent empty bins into a single bin with the lower edge at p_T^{l+1}, and this is essentially the modification we have made. By generating a large number of Monte Carlo samples and varying the number and the widths of bins with data, it was demonstrated that the results do not depend on the binning below p_T^l (see Ref. [128]).

5.2.4 Differential Cross Section Parameterization

The last question which should be addressed before calculating the actual limits from the p_T^γ fit, is the parameterization of the differential cross sections of the signal and background.

In our case the background has two components: the first does not depend on the anomalous couplings (the QCD background, see sec. 4.5.1, was parameterized as a function of p_T^γ, as shown in Fig. 4.12); the second component (the $\tau\tau$ background, see sec. 4.5.2) is proportional to the expected signal. Therefore it is sufficient to parameterize the p_T^γ spectrum of the signal in order to apply either unbinned or binned likelihood fit methods.

Similar to the parameterization of the total cross section (see sec. 5.1), the differential $d\sigma/dp_T^\gamma(h_a, h_b)$ cross section can be expressed in the following form:

$$\frac{d\sigma(h_a,h_b)}{dp_T^\gamma} = \frac{d\sigma_{SM}}{dp_T^\gamma}(p_T^\gamma) + a_0(p_T^\gamma)h_a + a_1(p_T^\gamma)h_b + b_0(p_T^\gamma)h_a^2 + b_1(p_T^\gamma)h_a h_b + b_2(p_T^\gamma)h_b^2, \tag{5.10}$$

where a_i, b_i are functions of the photon transverse momentum. In practice it is hard to obtain these functions using the p_T^γ spectrum calculated for several different couplings.

However, for solving the maximum likelihood problem given by equation (5.7), (5.8), or (5.9), one does not need to know the behaviour of the differential cross section in the full p_T^γ range. For the unbinned methods it is sufficient to know the differential cross section at the data points, and the total cross section. For the binned likelihood method only the total cross section in each of N_b bins is required. Therefore, instead of the parameterization (5.10) it is sufficient to perform pointlike parameterizations (5.1) either in several data points or in several fixed bins, which can be effectively done by the same 3×3 grid method as described in sec. 5.1. We used this simplified approach to carry out the fits.

In order to make it easier to study the smearing of the data points in the unbinned approaches, or to change the binning in the binned method, we first parameterized the differential cross section calculated with the DØBAUR Monte Carlo generator in each of the 3×3 grid nodes (h_a^i, h_b^j) in the following form:

$$\frac{d\sigma}{dp_T}(p_T|h_a^i,h_b^j) = \exp(c_0^{ij} + c_1^{ij}p_T + c_2^{ij}p_T^2 + c_3^{ij}p_T^3 + c_4^{ij}p_T^4) \tag{5.11}$$

in the p_T range from $p_T^{min} = 10$ GeV/c to 30 GeV/c, where such an approximation works very well. All data points are contained in this p_T region (see Fig. 4.13). We also calculated the total cross section at each of the grid points between p_T^{min} and $p_T^{max} = 250$ GeV/c, as it was discussed in the sec. 5.1. The 250 GeV/c cutoff was introduced for technical reasons. The total cross section above this threshold is negligible for anomalous couplings of any strength allowed by unitarity limits (see sec. 2.3.2). Both the parameterization (5.11) and the total cross section calculations were done independently for the electron and muon channel with very high statistics Monte Carlo runs, which made the errors in the c_k^{ij}, $k = 0...4$, negligible. The set of coefficients obtained is sufficient for calculating the likelihood functions (5.7), (5.8), (5.9) for any set of points or bins below 30 GeV/c.

5.2.5 Results of the p_T^{γ} Fit

Since the total statistics is only 6 events, we performed the p_T^{γ} fit only for the combination of the electron and muon channels. It can be done in two ways: either by maximizing the sum of the likelihood functions independently calculated for the $ee\gamma$ and $\mu\mu\gamma$ channels, or by maximizing the likelihood function based on the sum of the $d\sigma/dp_T$ distributions and $d\sigma_{bck}/dp_T$ distributions for electron and muon channels. In the first method one knows which of the 6 photons corresponds to each channel. In the second approach one does not use this information. The second method is preferred since the separation of the two channels is an artificial step which has to do with different detector response for the electrons and muons, and not with the physics of the $ZV\gamma$ couplings. Thus, there is no reason to distinguish between the photons corresponding to these two channels. The combined spectrum also smooths out statistical fluctuations which very likely take place for such restricted data sets. However, the difference in these two approaches is merely academic since the numerical results of the fits incorporating either of them are essentially the same.

The results of the binned luminosity-free likelihood fit of the combined electron and muon data for the $(h_{30}^Z, h_{40}^Z)/(h_{10}^Z, h_{20}^Z)$ and $(h_{30}^\gamma, h_{40}^\gamma)/(h_{10}^\gamma, h_{20}^\gamma)$ pairs of couplings and the form factor scale $\Lambda = 500$ GeV are shown in Figs. 5.6 and 5.7, respectively. The limits on the CP-conserving and CP-violating couplings are the same within our accuracy, and therefore they are shown in the same figure. The best fit favors the SM, similar to that for the total cross section fit (see sec. 5.1). This is shown in Fig. 5.8, together with the case of $h_{30}^Z = 2.0$, the 95% CL limit for h_{30}^Z. Comparison of the SM and the 95% CL limit cross sections demonstrates that the most significant information about the strength of anomalous couplings is indeed contained in the last bin of the histogram (see sec. 5.2.3).

The integrated luminosity obtained from the fit is

$$\int L dt = 13.4 \ {}^{+6.2}_{-4.7} \ \mathrm{pb}^{-1}, \tag{5.12}$$

which agrees very well with the average of the electron and muon channel of 13.6 ± 1.6 pb^{-1} (see sec. 4.2 and 4.3). The agreement ensures that the detection efficiencies and other detector-dependent effects have been properly taken into

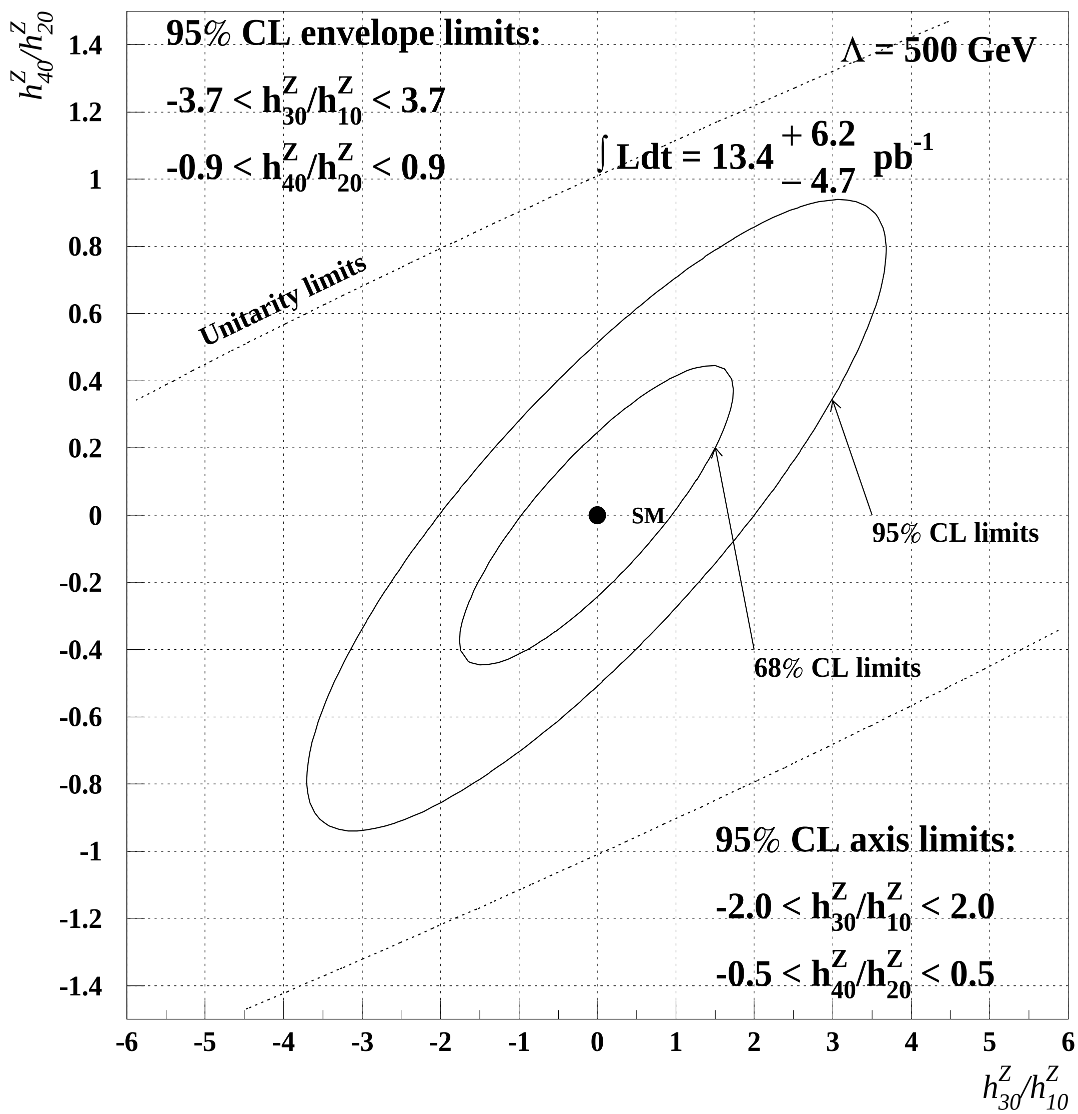

Figure 5.6: Limits on the pairs of the anomalous couplings $(h^Z_{30}, h^Z_{40})/(h^Z_{10}, h^Z_{20})$ from the binned p_T^γ fit. Integrated luminosity is treated as a free parameter. Contours represent 68% and 95% CL limits. The dashed lines show the limits obtained from partial wave unitarity (see sec. 2.3.2) for a form factor scale of $\Lambda = 500$ GeV.

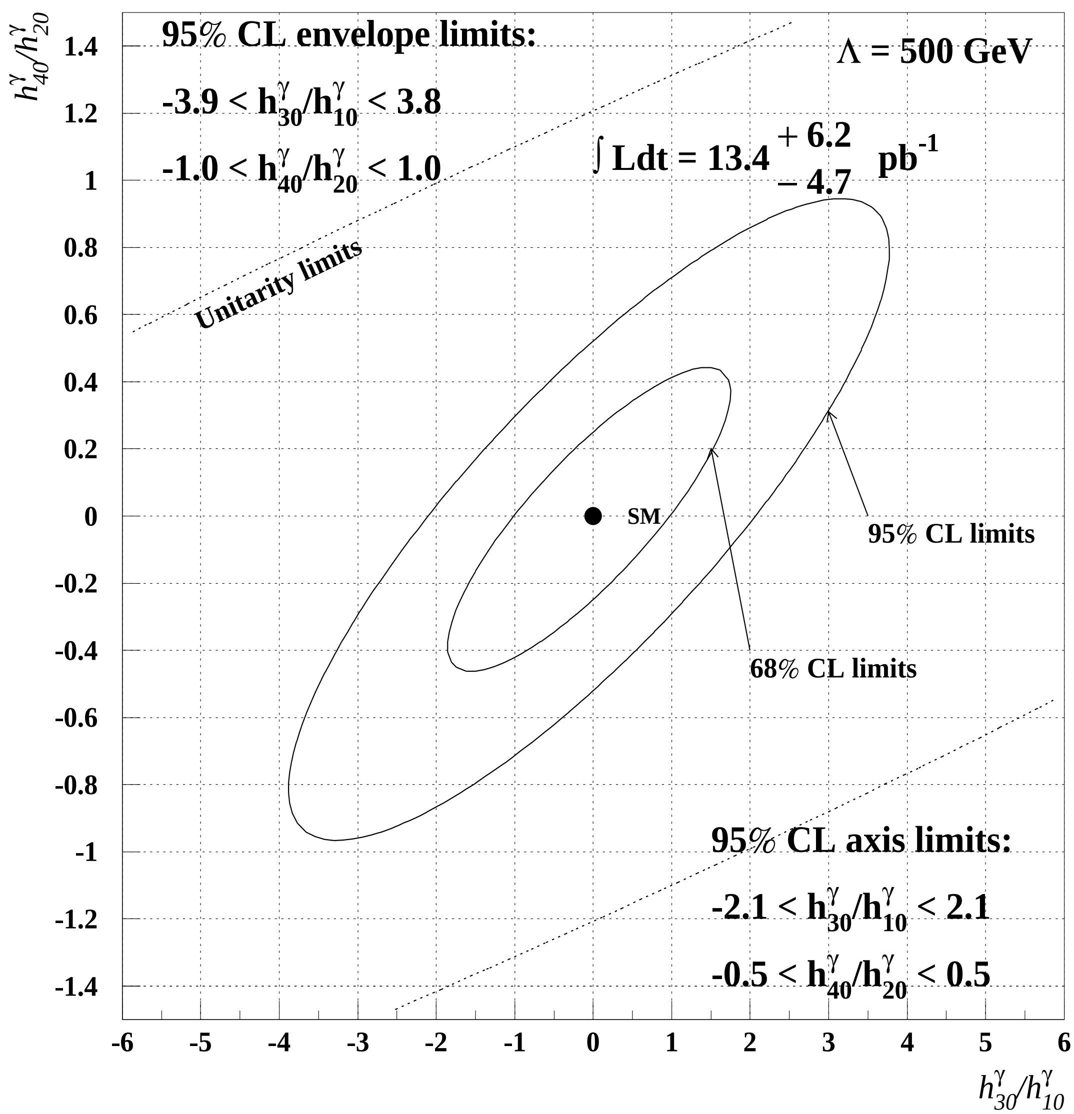

Figure 5.7: Limits on the pairs of the anomalous couplings $(h_{30}^{\gamma}, h_{40}^{\gamma})/(h_{10}^{\gamma}, h_{20}^{\gamma})$ from the binned p_T^{γ} fit. Integrated luminosity is treated as a free parameter. Contours represent 68% and 95% CL limits. The dashed lines show the limits obtained from partial wave unitarity (see sec. 2.3.2) for a form factor scale of $\Lambda = 500$ GeV.

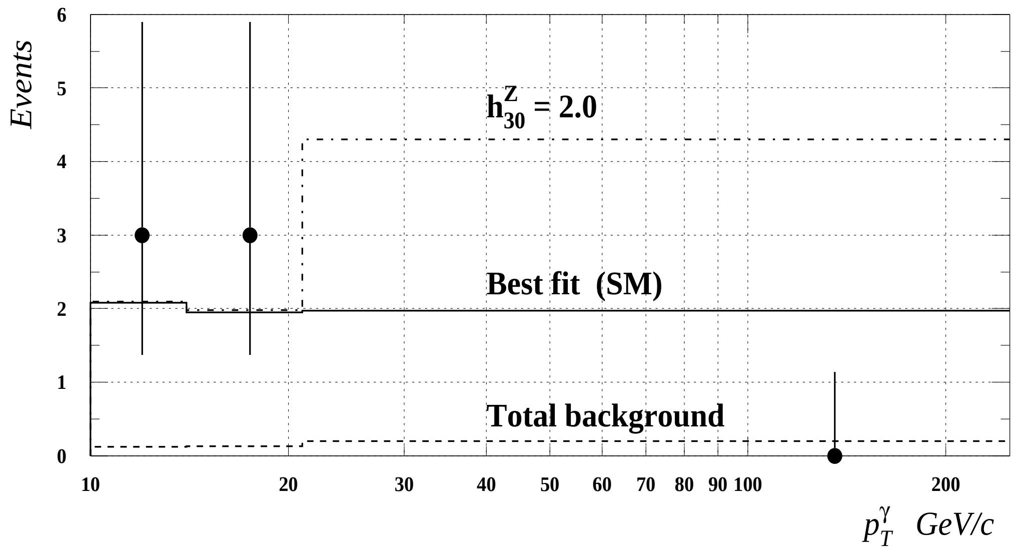

Figure 5.8: Results of the binned p_T^γ fit. Solid dots with error bars represent the data with Poisson 68% CL errors. The solid histogram corresponds to the number of events per bin for the best fit (sum of the signal and background) and favors the SM prediction. The dashed histogram shows the total background, whereas the dash-dotted histogram corresponds to the expected number of events per bin for the case of $h^Z_{30} = 2.0$, i.e. at 95% CL limit.

account in the Monte Carlo calculations of the cross section (see sec. 3.7).

The limits on the couplings from the transverse spectrum fit are much more stringent than those from the total cross section fit (see Table 5.2) and are completely contained inside the region allowed by partial wave unitarity. The definition of the axis and envelope limits is the same as for the total cross section fit (see sec. 5.1). The 95% CL limits on the anomalous couplings from the data are close to the unitarity limits for $\Lambda = 500$ GeV. With present statistics, DØ is therefore sensitive to form factor scales up to ~ 500 GeV at most. This means that for higher values of Λ there are some regions of the anomalous coupling space which are not excluded by our data, but are excluded from unitarity, i.e. the theoretical constraints start to be tighter than the 95% CL experimental limits for $\Lambda > 500$ GeV. This is illustrated in more detail in Fig. 5.9 which shows the limits on (h_{30}^Z, h_{40}^Z) for $\Lambda = 750$ GeV as well as the corresponding unitarity limits. Despite the fact that numerically these limits are more stringent than those for $\Lambda = 500$ GeV, part of the area inside the 95% CL contour for $\Lambda = 750$ GeV violates unitarity. Lowering of the form factor scale Λ results in numerically less stringent limits, but they are well contained within the theoretical unitarity limits, as illustrated by Fig. 5.10 which shows the limits on the same pair of couplings for the $\Lambda = 250$ GeV case. The situation is similar for all other pairs of couplings.

The 68% and 95% CL axis and envelope limits for these two pairs of couplings are summarized in the Table 5.3. The limits on the *CP*-violating pairs of couplings coincide with the limits on the corresponding pair of *CP*-conserving couplings. The limits from the generalized unbinned likelihood fit agrees with those obtained from the binned method[2]. We choose to quote the limits from the binned likelihood fit since they do not depend on effects due to smearing of the data points (see sec. 5.2.2).

Finally, the limits on the other pairs of couplings for $\Lambda = 500$ GeV are

[2]The axis limits of the unbinned likelihood fit are almost identical to those of the binned likelihood fit; the envelope limits are about 10% less stringent for the unbinned fit.

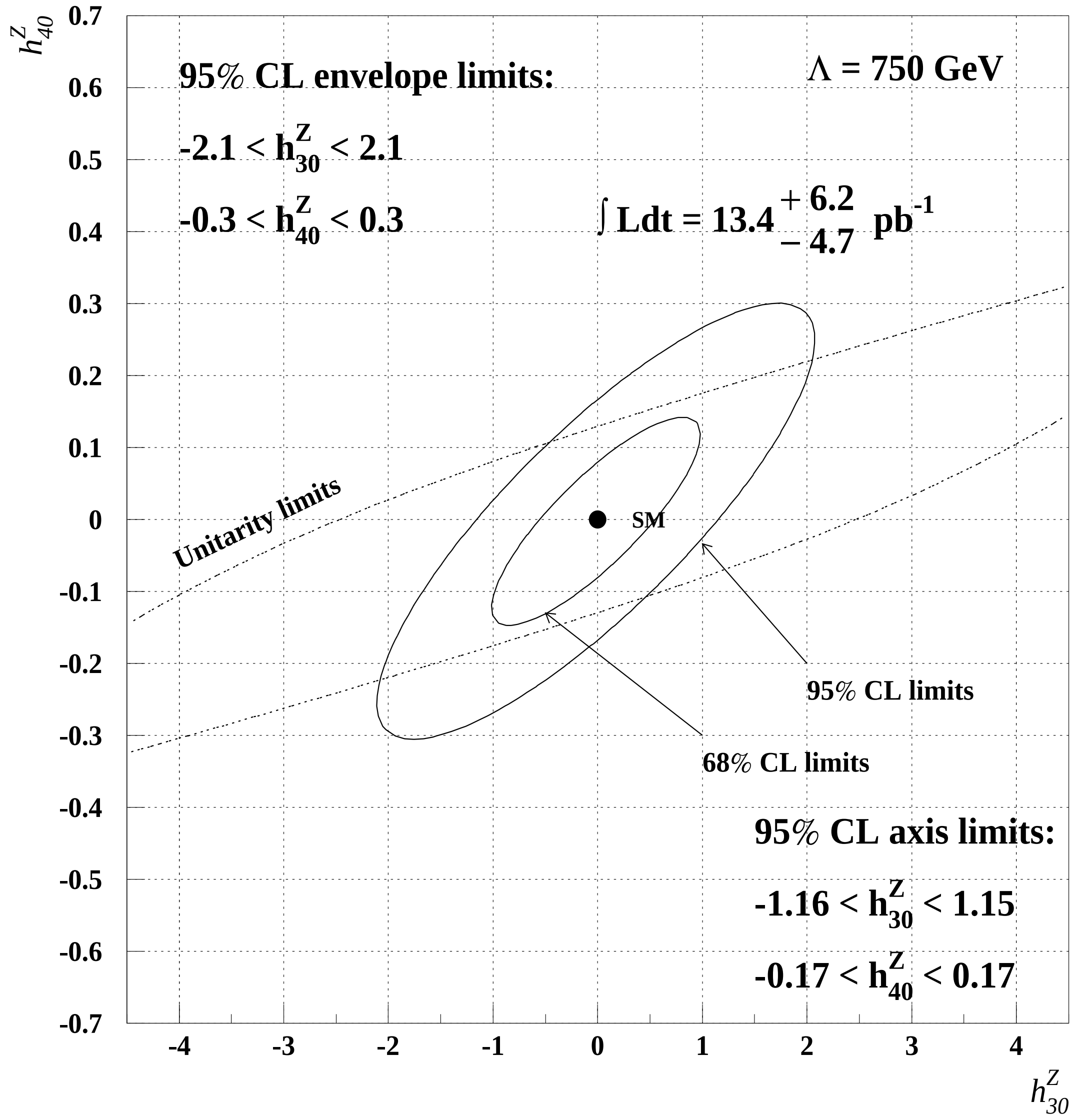

Figure 5.9: Limits on the pair of the anomalous couplings (h^Z_{30}, h^Z_{40}) from the binned p^γ_T fit. Integrated luminosity is treated as a free parameter. Contours represent 68% and 95% CL limits. The dashed lines show the limits obtained from partial wave unitarity (see sec. 2.3.2) for a form factor scale of $\Lambda = 750$ GeV.

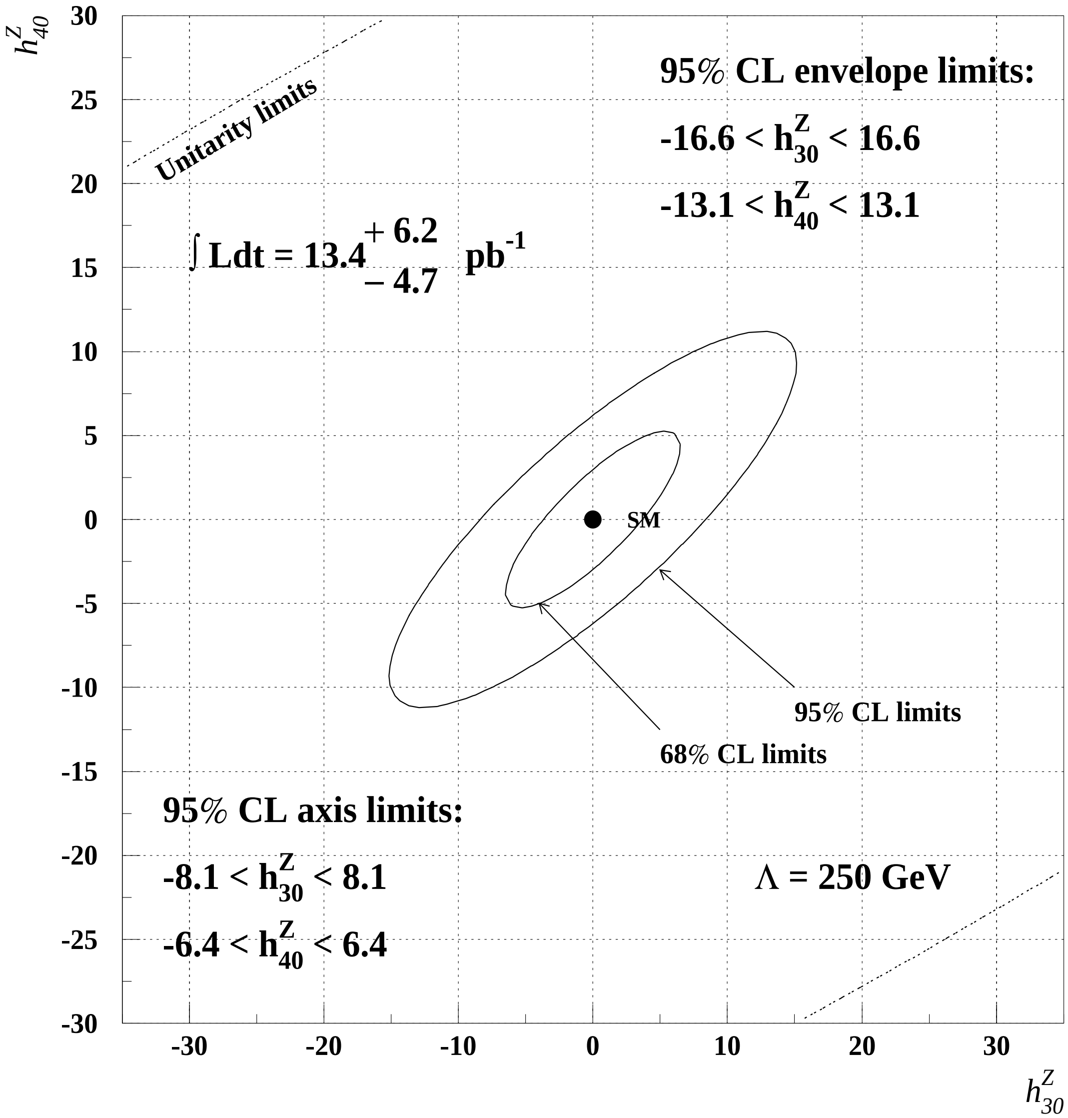

Figure 5.10: Limits on the pair of the anomalous couplings (h^Z_{30}, h^Z_{40}) from the binned p^γ_T fit. Integrated luminosity is treated as a free parameter. Contours represent 68% and 95% CL limits. The dashed lines show the limits obtained from partial wave unitarity (see sec. 2.3.2) for a form factor scale of $\Lambda = 250$ GeV.

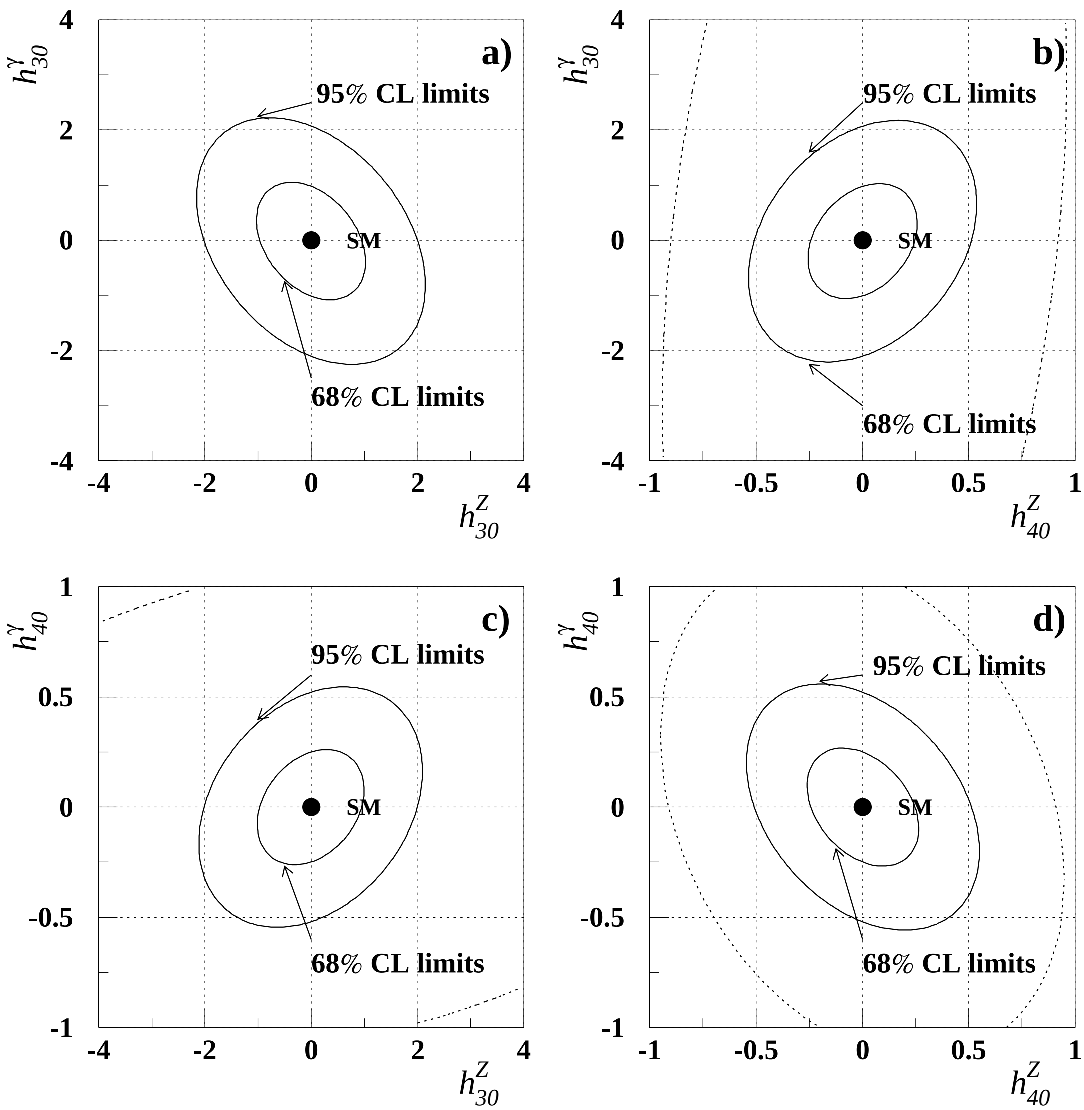

Figure 5.11: Limits on the weakly interfering pairs of anomalous couplings from the binned p_T^{γ} fit. Integrated luminosity is treated as a free parameter. Solid contours show the 68% and 95% CL limits (form factor scale $\Lambda = 500$ GeV) for the following pairs of couplings: a) $(h^Z_{30}, h^{\gamma}_{30})$; b) $(h^Z_{40}, h^{\gamma}_{30})$; c) $(h^Z_{30}, h^{\gamma}_{40})$; d) $(h^Z_{40}, h^{\gamma}_{40})$. The dotted curves show the unitarity limits [35]. (Unitarity limits for plot (a) are outside the area shown.)

Conditions	Axis limits	Envelope limits
$\Lambda = 500$ GeV (h^Z_{30}, h^Z_{40})	$-2.00 < h^Z_{30} < 2.02$ $-0.51 < h^Z_{40} < 0.51$	$-3.71 < h^Z_{30} < 3.68$ $-0.94 < h^Z_{40} < 0.94$
$\Lambda = 500$ GeV (h^Z_{10}, h^Z_{20})	$-2.01 < h^Z_{10} < 2.02$ $-0.51 < h^Z_{20} < 0.51$	$-3.75 < h^Z_{10} < 3.77$ $-0.95 < h^Z_{20} < 0.96$
$\Lambda = 500$ GeV $(h^\gamma_{30}, h^\gamma_{40})$	$-2.11 < h^\gamma_{30} < 2.07$ $-0.52 < h^\gamma_{40} < 0.52$	$-3.88 < h^\gamma_{30} < 3.77$ $-0.97 < h^\gamma_{40} < 0.94$
$\Lambda = 500$ GeV $(h^Z_{30}, h^\gamma_{30})$	$-2.02 < h^Z_{30} < 2.00$ $-2.11 < h^\gamma_{30} < 2.07$	$-2.16 < h^Z_{30} < 2.14$ $-2.25 < h^\gamma_{30} < 2.21$
$\Lambda = 500$ GeV $(h^Z_{40}, h^\gamma_{30})$	$-0.51 < h^Z_{40} < 0.51$ $-2.11 < h^\gamma_{30} < 2.07$	$-0.54 < h^Z_{40} < 0.54$ $-2.21 < h^\gamma_{30} < 2.17$
$\Lambda = 500$ GeV $(h^Z_{30}, h^\gamma_{40})$	$-2.02 < h^Z_{30} < 2.00$ $-0.52 < h^\gamma_{40} < 0.52$	$-2.12 < h^Z_{30} < 2.09$ $-0.55 < h^\gamma_{40} < 0.55$
$\Lambda = 500$ GeV $(h^Z_{40}, h^\gamma_{40})$	$-0.51 < h^Z_{40} < 0.51$ $-0.52 < h^\gamma_{40} < 0.52$	$-0.54 < h^Z_{40} < 0.55$ $-0.56 < h^\gamma_{40} < 0.56$
$\Lambda = 250$ GeV (h^Z_{30}, h^Z_{40})	$-8.12 < h^Z_{30} < 8.12$ $-6.37 < h^Z_{40} < 6.37$	$-16.6 < h^Z_{30} < 16.6$ $-13.1 < h^Z_{40} < 13.1$
$\Lambda = 750$ GeV (h^Z_{30}, h^Z_{40})	$-2.00 < h^Z_{30} < 2.02$ $-0.51 < h^Z_{40} < 0.51$	$-3.71 < h^Z_{30} < 3.68$ $-0.94 < h^Z_{40} < 0.94$

Table 5.3: 95% CL limits on the anomalous couplings from the binned likelihood p^γ_T fit.

shown in Fig. 5.11. It is clear, that the interference between these couplings is much less strong than that for the pair of couplings defined in sec. 5.1. Numerically it is represented by the envelope limits being very close to the axes limits. Also, the interference between $(h^Z_{i0}, h^\gamma_{i0})$ has a different sign (corresponding ellipses are tilted in the opposite direction), in agreement with theoretical predictions [20]. The numerical limits for these pairs of couplings are listed in Table 5.3.

The experimental fact that the interference between $ZZ\gamma$ and $Z\gamma\gamma$ couplings is small (of the order of 10%), together with the fact that couplings with opposite CP-parity do not interfere, allows us to interpret the contours in Figs. 5.6 and 5.7 as a good approximation for *global* limits on a corresponding pair of couplings, i.e. limits which are independent of the values of the other six couplings. Thus, the envelope limits on strongly interfering pairs of couplings are close to the global limits, which justifies our approach based on obtaining the limits in two-dimensional projections of the eight-dimensional anomalous coupling space.

Chapter 6

Conclusions

But you must know that we are all in agreement, whatever we say.

Turba Philosophorum

In this work we carried out a novel test of the gauge sector of the Standard Model of electromagnetic interactions by searching for anomalous self-interactions between the heavy Z boson and massless photon fields.

We observed 4 $Z\gamma$ events in the electron channel, and 2 $Z\gamma$ events in the muon channel with an overall background of 0.5 events. The observed number of events, as well as the p_T^γ spectrum of the $Z\gamma$ candidates, agrees well with the SM predictions. Both the limits from the total cross section measurements, and from the fit of the p_T^γ spectrum were derived.

The results obtained constitute the first independent measurement of the self-interactions between neutral gauge bosons. Similar analyses were also carried out simultaneously by the CDF Collaboration at the Tevatron and the L3 Collaboration at LEP which recently announced their first results on this topic [5, 6] (also, see sec. 2.4).

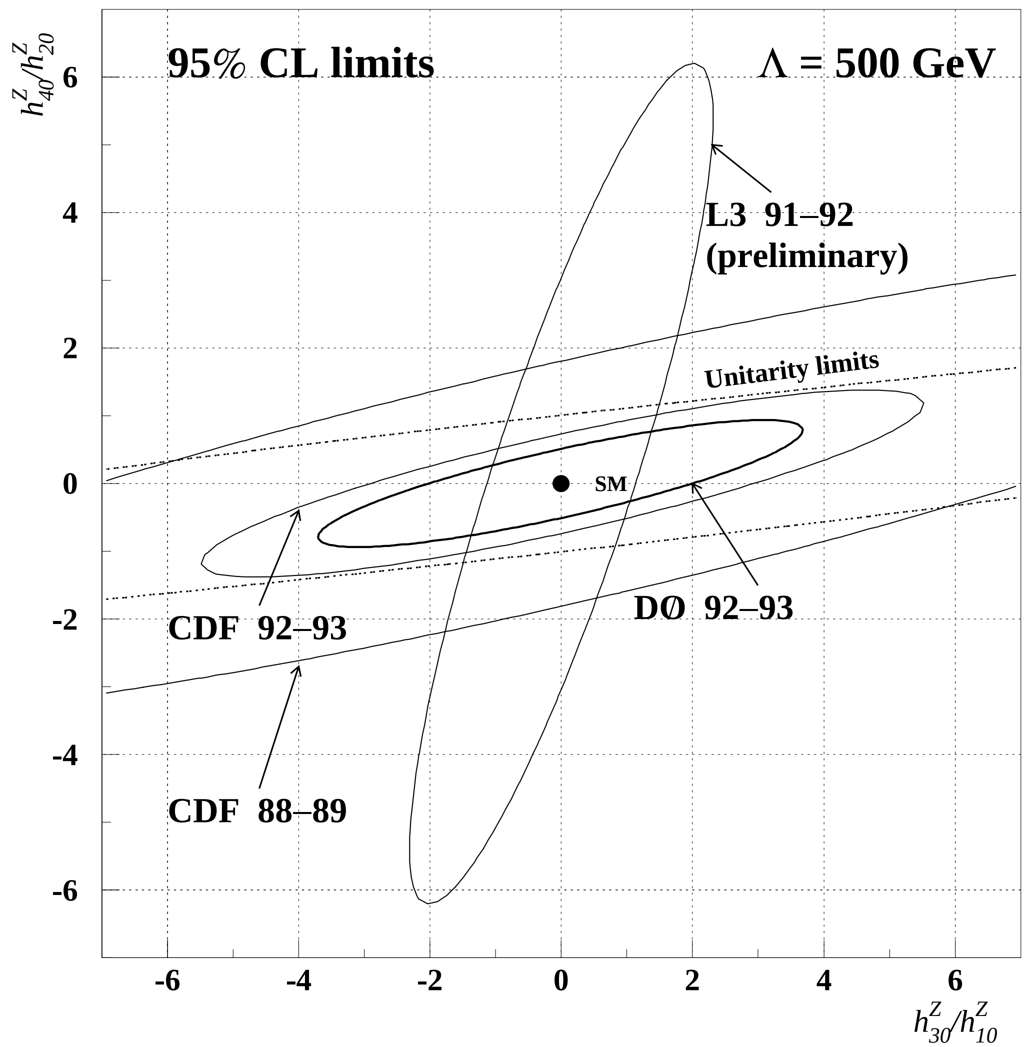

Figure 6.1: Comparison of the limits on the anomalous $ZZ\gamma$ (h^Z_{30}, h^Z_{40}) and (h^Z_{10}, h^Z_{20}) couplings from this experiment (Table. 5.3), CDF [5], and preliminary results from L3 [6].

A comparison of the limits of the three experiments on the pair of CP-conserving $ZZ\gamma$ (h^Z_{30}, h^Z_{40}) couplings is shown in Fig. 6.1. The axis limits obtained by the DØ Collaboration are about 20% better than those of CDF (92 – 93 data) for all possible pairs of anomalous couplings. CDF has also published limits from the first, lower luminosity, run (88 – 89) [132] which are also shown in the same plot. They are outside the unitarity limits (given by the dashed line in the same plot) in the range of interest for the anomalous couplings. The limits of the L3 Collaboration on the dimension six (see sec. 2.3.2) couplings, h^Z_{10}, h^Z_{30}, from the $Z \to \nu\bar{\nu}\gamma$ measurements are better than those obtained at the Tevatron at the cost of significantly less stringent limits on the dimension eight couplings, h^Z_{20}, h^Z_{40}. The limits of other low energy experiments are far outside the unitarity limits (see sec. 2.4).

The limits on the $Z\gamma\gamma$ couplings, which can not be measured in the neutrino decay mode of Z (see sec. 2.4), constitute the first experimental measurement of these couplings, obtained independently and simultaneously by CDF and in this work. The DØ axis limits are about 20% better than the corresponding CDF limits in this case as well.

The current limits on the anomalous $ZV\gamma$ couplings will be significantly improved with the data which are presently collected in run Ib of the Tevatron. The statistics expected to be accumulated by DØ/CDF in this run is at least a factor of 5 greater than that in run Ia. This corresponds to a 50% improvement in the sensitivity to the anomalous couplings. Inclusion of the neutrino decay channel of the Z will further improve the limits (see sec. 4.4). The limits can also be improved by analyzing double differential cross sections of the $Z\gamma$ production, e.g. $d^2\sigma/dp_T^\gamma d\Delta R_{\ell\gamma}^{min}$. A significant number of observed events is required, however, for such a multidimensional analysis.

Another interesting analysis which will become possible with larger statistics is the measurement of the ratio of the $Z\gamma$ and $W\gamma$ production cross sections [133]. This ratio is sensitive to the $ZV\gamma$ and $WW\gamma$ anomalous couplings. Most of the theoretical and experimental uncertainties for both channels cancel in the ratio, which makes it a particularly useful quantity for testing the electroweak boson self-interactions.

Anomalous $ZV\gamma$ couplings can also be studied in LEP II experiments and at future hadron colliders, e.g. an upgraded Tevatron (see sec. 3.1.3) or the LHC. The sensitivity of these future experiments to anomalous couplings is expected to be at least $5-10$ times higher than the one achieved in this work, which will make it possible to prove or exclude certain anomalous coupling models. However, such an improvement most likely will be possible only in the next decade.

Bibliography

[1] S.L. Glashow, Nucl. Phys. **22** (1961) 579; S. Weinberg, Phys. Rev. Lett. **19** (1967) 1264; A. Salam, *Elementary Particle Theory*, ed. N. Svartholm (Almquist and Wiksells, Stockholm, 1969) p. 367.

[2] F.J. Hassert *et al.*, Phys. Lett. **B46** (1973) 138.

[3] G. Arnison *et al.* (UA1 Collaboration), Phys. Lett. **126B** (1983) 398; Phys. Lett. **129B** (1983) 273.

[4] P. Bagnaia *et al.* (UA2 Collaboration), Phys. Lett. **129B** (1983) 310; Z. Phys. **24C** (1984) 1.

[5] F. Abe *et al.* (CDF Collaboration), preprint Fermilab–Pub–94/304–E.

[6] J. Busenitz (for the L3 Collaboration), Talk given at the DPF '94 Conference, Albuquerque, 1994.

[7] M. Kobayashi, T. Maskawa, Prog. Theor. Phys. **49** (1973) 652.

[8] P.W. Higgs, Phys. Rev. Lett. **12** (1964) 508; Phys. Rev. **145** (1966) 1156.

[9] Review of Particle Properties, PDG, Phys. Rev. **D50** (1994) 1191, 1233, 1279–1282, 1304, 1308, 1405.

[10] Delahaye F. *et al.*, Metrologia **22** (1986) 103.

[11] G. Bardin et al., Phys. Lett. **137B** (1984) 135.

[12] F. Abe *et al.* (CDF Collaboration), Phys. Rev. Lett. **73** (1994) 225.

[13] G. t'Hooft, Nucl. Phys. **B33** (1971) 173; **B35** (1971) 167.

[14] D. Buskulic *et al.* (ALEPH Collaboration) Z. Phys. **C62** (1994) 539; P. Abreu *et al.* (DELPHI Collaboration) Nucl. Phys. **B418** (1994) 403; M. Acciarri *et al.* (L3 Collaboration) Z. Phys. **C62** (1994) 551; R. Akers *et al.* (OPAL Collaboration) Z. Phys. **C61** (1994) 19;

[15] J. Alitti *et al.* (UA2 Collaboration), Phys. Lett. **277B** (1992) 194.

[16] F. Abe *et al.* (CDF Collaboration), preprint Fermilab–Pub–94/236–E.

[17] S. Abachi *et al.* (DØ Collaboration), *"Measurement of the $WW\gamma$ Gauge Boson Couplings at the Tevatron Collider"*, to appear in Phys. Rev. Lett.

[18] F.M. Renard, Nucl. Phys. **B196** (1982) 93.

[19] K. Hagiwara *et al.*, Nucl. Phys. **B282** (1987) 253.

[20] U. Baur, E.L. Berger, Phys. Rev. **D47** (1993) 4889.

[21] C.N. Yang, Phys. Rev. **77** (1950) 242.

[22] J.M. Cornwall, D.N. Levin, G. Tiktopoulos, Phys. Rev. Lett. **30** (1973) 1268; Phys. Rev. **D10** (1974) 1145; C.H. Llewellyn Smith, Phys. Lett. **46B** (1973) 233; S.D. Joglekar, Ann. of Phys. **83** (1974) 427.

[23] U. Baur, D. Zeppenfeld, Phys. Lett. **201B** (1988) 383.

[24] K. Hagiwara, D. Zeppenfeld, Nucl. Phys. **B274** (1986) 1.

[25] H. Czyz, K. Kolodziej, M. Zralek, Z. Phys. **C43** (1989) 97.

[26] U. Baur, E.L. Berger, Phys. Rev. **D41** (1990) 1476.

[27] J.D. Bjorken, S.D. Drell, *"Relativistic quantum fields"*, ed. McGraw-Hill (New York, 1965) p. 123.

[28] F. Boudjema, *private communication.*

[29] A.D. Martin, R.G. Roberts, W.J. Stirling, Phys. Lett. **306B** (1993) 145.

[30] C.Y. Lee, Phys. Rev. **D32** (1985) 3044.

[31] A. Barroso, F. Boudjema, J. Cole, N. Dombey, Z. Phys. **C28** (1985) 149.

[32] J. Ohnemus, Phys. Rev. **D47** (1993) 940; J. Ohnemus, preprint UCD–94–29 (1994).

[33] U. Baur, T. Han, J. Ohnemus, Phys. Rev. **D48** (1993) 5140.

[34] A. de Rujula, M.B. Gavela, P. Hernandez, E. Masso, Nucl. Phys. **B384** (1992) 3; K. Hagiwara, S. Ishihara, R. Szalapski, D. Zeppenfeld, Phys. Lett. **283B** (1992) 353; C.P. Burgess, D. London, Phys. Rev. Lett. **69** (1992) 3428.

[35] U. Baur, *private communication.*

[36] J. Bailey *et al.*, Nucl. Phys. **B150** (1979) 1; E.R. Cohen, B.N. Taylor, Rev. Mod. Phys. **59** (1987) 1121.

[37] F. Herzog, Phys. Lett. **148B** (1984) 355; **155B** (1985) 468; M. Suzuki, Phys. Lett. **153B** (1985) 289; A. Grau, J.A. Griffols, Phys. Lett **144B** (1985) 283; J.C. Wallet, Phys. Rev. **D32** (1985) 813;

[38] P. Meŕy, S.E. Moubarik, M. Perrottet, F.M. Renard, Z. Phys. **C46** (1990) 229.

[39] K.F. Smith *et al.* Phys. Lett. **B234** (1990) 191.

[40] W.J. Marciano, A. Queijeiro, Phys. Rev. **D33** (1986) 3449; F. Boudjema, K. Hagiwara, C. Hamzaoui, K. Numata, Phys. Rev. **D43** (1991) 2223.

[41] P. Acton *et al.* (OPAL Collaboration), Phys. Lett. **273B** (1991) 338.

[42] O. Adriani *et al.* (L3 Collaboration), Phys. Lett. **297B** (1992) 469.

[43] X. Tata, *The Standard Model and Beyond*, ed. J. Kim (World Scientific, Singapore, 1991), p. 304; H. Nilles, Phys. Rep. **110** (1984) 1; P. Nath, R. Arnowitt, A. Chamseddine, *Applied* $N = 1$ *Supergravity* ICTP Series in Theoretical Physics, Vol. 1 (World Scientific, Singapore, 1984); H. Haber, G. Kane, Phys. Rep. **117** (1985) 75.

[44] A.B. Lahanas, V.C. Spanos, Phys. Lett **334B** (1994) 378.

[45] A. Meńdez, A. Pomarol, Phys. Lett. **272B** (1991) 313.

[46] D. Chang, W.Y. Keung, P.B. Pal, preprint Fermilab–PUB–94/196–T (1994).

[47] H. Harari, N. Seiberg, Phys. Lett. **98B** (1981) 269; Nucl. Phys. **204** (1982) 141; O.W. Greenberg, J. Sucher, Phys. Lett. **99B** (1981) 339; H. Fritzsch, G. Mandelbaum, Phys. Lett. **102B** (1981) 319; **109B** (1982) 224; R. Barbieri, R.N. Mohapatra, Phys. Rev. **D25** (1982) 2419.

[48] M. Leurer, H. Harari, R. Barbieri, Phys. Lett. **141B** (1984) 455; M. Leurer, Phys. Lett. **144B** (1984) 273.

[49] F.T. Cole *et al.*, *"Design Report, Superconducting Acceleartor,"* FNAL Internal Note (1979), unpublished; *"Design report, Tevatron 1 Project,"* FNAL Internal Note (1984), unpublished.

[50] W.J. Thompson, *Ph.D. Dissertation*, SUNY @ Stony Brook (1994), unpublished.

[51] R. Fernow, *"Introduction to Experimental Particle Physics,"* Cambridge University Press, Cambridge (1986).

[52] D. Patterson, *"The FNAL Linac,"* FNAL Internal Note (1986), unpublished.

[53] A. Braun, T. Meyer, *"The Main Ring Rookie Book,"* FNAL Internal Note (1991), unpublished.

[54] E. Harms, *"The Antiproton Source Rookie Book v.0.2,"* FNAL Internal Note (1993), unpublished.

[55] *"Fermilab III: Building the Future,"* in Fermilab Annual Report (1990), unpublished.

[56] J. Peoples, talk at the "University of DØ," September 8, 1994, DØ Internal Note #2293, unpublished; D. Amidei *et al.*, preprint Fermilab–Conf–94/249–E (1994), to appear in the Proc. of the DPF '94 Conference, Albuquerque, August 1994.

[57] S. Abachi *et al.*, Nucl. Instr. and Methods **A338** (1994) 185.

[58] F. Abe *et al.*, Nucl. Instr. and Methods **A271** (1988) 387.

[59] B. Piffer *et al.* (DØ Collaboration), *"An Experiment at DØ to Study Antiproton-Proton Collisions at 2 TeV,"* FNAL Internal Note (1983), unpublished.

[60] H. Williams, Ann. Rev. Nucl. Sci. **36** (1986) 366.

[61] S. Feher, *private communication.*

[62] C.W. Fabjan, *"Calorimeters in High Energy Physics,"* in Experimental Techniques in High Energy Physics, edited by T. Ferbel, ed. Addison–Wesley, Menlo Park (1987) p. 257.

[63] R. Wigmans, Nucl. Instr. and Methods **A259** (1987) 389.

[64] C.W. Fabjan *et al.*, Nucl. Instr. and Methods **141** (1977) 61.

[65] R. Wigmans, preprint CERN/EF 86–18 (1986), unpublished.

[66] J. Yu, *Ph.D. Dissertation*, SUNY @ Stony Brook (1993), unpublished.

[67] S. Rajagopalan, *Ph.D. Dissertation*, Northwestern University (1992), unpublished.

[68] H. Aihara *et al.* (DØ Collaboration), Nucl. Instr. and Methods **A325** (1993) 393.

[69] M. Paterno, DØ Internal Note #1782 (1993), unpublished.

[70] M. Paterno, *Ph.D. Dissertation*, SUNY @ Stony Brook (1994), unpublished.

[71] W.G.D. Dharmaratna, Internal DØ Note #1731 (1993), unpublished.

[72] J. Kotcher, *private communication.*

[73] I. Adam, DØ Internal Notes #2297 and #2298 (1994), unpublished.

[74] U. Heintz, DØ Internal Notes #2209 and #2268 (1994), unpublished.

[75] F. Sauli, *"Principles of Operation of Multiwire Proportional and Drift Chambers,"* in Experimental Techniques in High Energy Physics, edited by T. Ferbel, ed. Addison–Wesley, Menlo Park (1987) p. 79.

[76] B. Angstadt *et al.*, DØ Internal Note #1276 (1991), unpublished.

[77] R. Yarema, IEEE Trans. on Nucl. Sci. **NS33** (1986) 933.

[78] A.R. Clark *et al.* (DØ Collaboration), Nucl. Instr. and Methods **A279** (1989) 243.

[79] E. Oltman, *private communication.*

[80] A.R. Clark *et al.* (DØ Collaboration), Nucl. Instr. and Methods **A315** (1992) 193.

[81] F. Feinstein, *Ph.D. Dissertation*, A'l'Universite de Paris-Sud, Centre d'Orsay (1987), unpublished.

[82] V.L. Ginsburg, I.M. Frank, JETP **16** (1946) 15.

[83] Alain Pluquet, *private communication.*

[84] T. Behnke, *Ph.D. Dissertation*, SUNY @ Stony Brook (1989), unpublished; D. Pizzuto, *Ph.D. Dissertation*, SUNY @ Stony Brook (1991), unpublished.

[85] S. Fehers, G. Finocchiaro, G. Landsberg, DØ Internal Notes #1482 (1992), #1594 (1993), #1483 (1994), unpublished.

[86] C. Brown *et al.*, Nucl. Instr. and Methods **A279** (1989) 331.

[87] Y. Antipov *et al.*, Nucl. Instr. and Methods **A297** (1990) 121.

[88] J. Bantly *et al.*, IEEE Trans. on Nucl. Sci. **41** (1994) 1274.

[89] M. Abolins *et al.*, IEEE Trans. on Nucl. Sci. **36** (1989) 384; Nucl. Instr. and Methods **A289** (1990) 543.

[90] J.M. Butler, DØ Internal Note #1682 (1993), unpublished.

[91] J. Bantly, *private communication.*

[92] D. Cutts *et al.*, in Proc. of the Intern. Conf. on Computing in HEP (Amsterdam, 1985) 287; (Oxford, 1989); (Annecy, 1992) 262.

[93] M. Goosens *et al.*, CERN Program Library Long Writeup Q100, CERN (1991).

[94] B. Klima, H.B. Prosper, DØ Internal Note #944 (1990), unpublished.

[95] J. Cochran, *Ph.D. Dissertation*, SUNY @ Stony Brook (1993), unpublished.

[96] S.J. Wimpenny *et al.*, Nucl. Instr. and Methods **A279** (1989) 359.

[97] N. Amos *et al.*, DØ Internal Note #2031 (1994), unpublished.

[98] F. Abe *et al.* (CDF Collaboration), preprints Fermilab–Pub–93/232–E (1993), Fermilab–Pub–93/233–E (1993), Fermilab–Pub–93/234–E (1993).

[99] N. Amos *et al.* (E710 Collaboration), Phys. Lett. **B243** (1990) 158.

[100] N. Amos *et al.*, DØ Internal Note #2186 (1994), unpublished.

[101] N. Gelfand, preprint Fermilab FN–538 (1990), unpublished.

[102] H.-U. Bengtsson, T. Sjostrand, PYTHIA v5.6, CERN Program Library Long Writeup W5045, CERN (1991).

[103] R. Brun, F. Carminati, *GEANT v3.14*, CERN Program Library Long Writeup W5013, CERN (1993); J. Womersley, DØ Internal Note #1520 (1992), unpublished.

[104] F. Paige, S. Protopopescu, BNL Report no. BNL–38034 (1986), unpublished.

[105] J. Jiang, DØ Internal Note #2249 (1994), unpublished.

[106] F. Abe *et al.* (CDF Collaboration), in press in Phys. Lett. **B** (1994).

[107] H. Plothow-Besch, *PDFLIB v4.15*, CERN Program Library Long Writeup W5051, CERN (1993).

[108] J. Botts *et al.* (CTEQ Collaboration), Phys. Lett. **304B** (1993) 159.

[109] R. Engelmann *et al.*, Nucl. Instr. and Methods **A216** (1983) 45; M. Narain (DØ Collaboration), in proc. of DPF '92, (1993) 1678.

[110] S. Abachi *et al.*, Nucl. Instr. and Methods **A324** (1993) 53.

[111] M. Narain, U. Heintz, DØ Internal Note #2351 (1994), unpublished.

[112] O. Dahl, *private communication.*

[113] S. Abachi *et al.*, Phys. Rev. Lett. **72** (1994) 2138.

[114] U. Heintz, *private communication.*

[115] R. Avery *et al.*, DØ Internal Note #1355 (1992), unpublished.

[116] S. Fahey, *private communication.*

[117] G. Landsberg, HITSINFO package description, to be released as a DØ Internal Note.

[118] M. Kelly, DØ Internal Note #2215 (1994), unpublished; M. Fatyga, D. Chakraborty, DØ Internal Note #1753 (1993), unpublished.

[119] S. Fahey, DØ Internal Note #2277 (1994), unpublished.

[120] C. Quigg, Rev. Mod. Phys. **49** (1977) 297.

[121] A. Klatchko, S. Youssef, DØ Internal Note #1769 (1993), unpublished.

[122] O. Helene, Nucl. Instr. and Methods **212** (1983) 319; Nucl. Instr. and Methods **228** (1984) 120.

[123] G. Zech, Nucl. Instr. and Methods **A277** (1989) 608; H. Prosper, Phys. Rev. **D37** (1988) 1153; Nucl. Instr. and Methods **A241** (1985) 236.

[124] F. James, Nucl. Instr. and Methods **A240** (1985) 203.

[125] H. Cramér, Mathematical Methods of Statistics, Princeton University Press, 1946.

[126] R.D. Cousins, V.L. Higland, Nucl. Instr. and Methods **A320** (1992) 331.

[127] J. Cortés *et al.*, Nucl. Phys. **B278** (1986) 26.

[128] G. Landsberg, in Proc. Workshop on Physics at Current Accelerators and the Supercollider, ANL–HEP–CP–93-92 (1992) 303.

[129] G. Landsberg, DØ Internal Note #2085 (1994), unpublished.

[130] W.T. Eadie *et al.*, Statistical Methods in Experimental Physics, North Holland, Amsterdam, 1971.

[131] J. Orear, preprint CLNS 82/511, Cornell (1982).

[132] F. Abe *et al.* , preprint Fermilab 94/244–E, Phys. Rev. **D**, in print.

[133] U. Baur, S. Errede, J. Ohnemus, Phys. Rev. **D48** (1993) 4103.